Communications from the
Konkoly Observatory
of the Hungarian
Academy of Sciences

Mitteilungen
der Sternwarte der
Ungarischen Akademie
der Wissenschaften

Budapest–Svábhegy

No. 103
(Vol. 13, Part 3)

The Interaction of Stars with their Environment II.

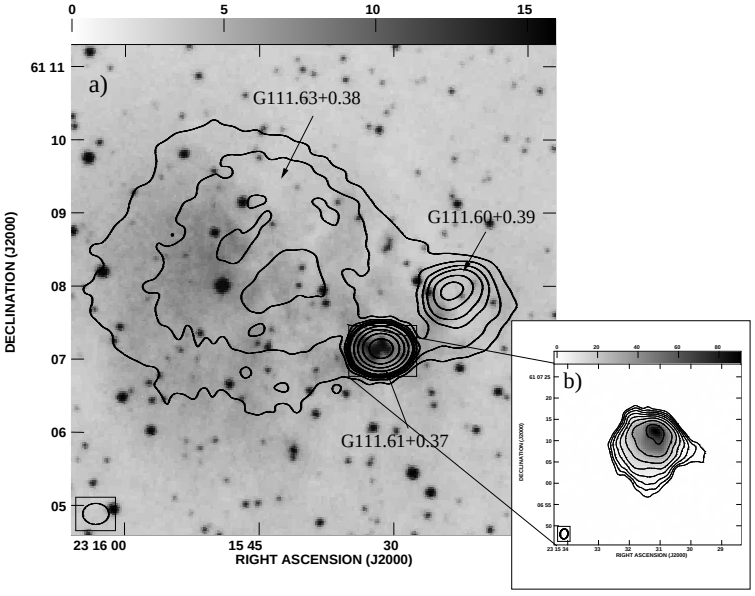

Proceedings of the workshop held at the Eötvös Loránd University, Budapest, Hungary, 15–18 May, 2002

Budapest, 2003

EDITORS:

Csaba Kiss, **Mária Kun**
Konkoly Observatory of the Hungarian Academy of Sciences
P.O. Box 67, H-1525 Budapest, Hungary

and **Vera Könyves**
Astronomy Department, Eötvös Loránd University
P.O. Box 32, H-1518 Budapest, Hungary

ISBN 963 8361 41 7
HU ISSN 0238-2091
Responsible publisher: Lajos G. Balázs

Contents

Young Stars

(Post-)Main-Sequence Stars

Winds and Bubbles

Processes on Galactic Scales

PREFACE

The first workshop and spring school organized by the Department of Astronomy of the Loránd Eötvös University and Konkoly Observatory was held in 1996 at Visegrád, Hungary. The second conference of the series followed it six years later in Budapest. During this six years several new aspects of this field of research emerged. The mid- and far-infrared detectors of ISO opened new windows on the great variety of phenomena related to the interactions between stars and their environment. New types of objects came into the foreground, such as circumstellar environments of brown dwarfs and very cold cloud cores.

Participants from nine countries, mainly students, attended the workshop, whose topics embraced a wide scale of phenomena accompanying the life of the stars, from protostellar winds and disks through the effects of pulsating stellar atmospheres on the surrounding gas and dust to circumstellar envelopes of Wolf-Rayet and post-AGB stars.

We hope that the two volumes of 'Interactions of Stars with their Environment' published by Konkoly Observatory will be followed by further issues on this intriguing and amazing field of astronomy.

We are grateful to the Astronomy Department of the Eötvös Loránd University for the hospitality during the conference and to the Hungarian Research Found (OTKA) for the financial support.

These proceedings could not have been published without the financial resources provided by Dr. L. Szabados and Dr. L.V. Tóth (OTKA #T029013 and #T043773). Their help is highly appreciated.

The Editors

Star Formation

Multivariate Separation of Cosmic Components

L.G. Balázs
Konkoly Observatory of the Hungarian Academy of Sciences
P.O. Box 67, H-1525 Budapest, Hungary
E-mail: balazs@konkoly.hu

Abstract

Observing and storing the photons of the incoming radiation from the Cosmos typically give a data cube defined by $(\alpha, \delta, \lambda)$. It is easy to translate this data structure into the formalism of multivariate statistics. A common problem in the multivariate statistics is whether the stochastic variables described by observed properties are statistically independent or can be described by a less number of hidden variables. This is the task of factor analysis. Forming groups from cases having similar properties according to the measures of similarities or the distances is the task of cluster analysis. We demonstrated in three cases how these technics can be used for separating physically independent cosmic components projected onto the same celestial area by chance.

1. Introduction: Nature of astronomical information

The information we receive from Cosmos is predominantly in the form of electromagnetic radiation. An incoming plain wave can be characterized by the following quantities:

$$\underline{n}\,(direction),\ \lambda\,(wavelength),\ polarization.$$

These physical quantities determine basically the possible observational programs:

1. Position $\Longrightarrow$ astrometry
2. Distribution of photons with $\lambda \Longrightarrow$ spectroscopy
3. Number of photons $\Longrightarrow$ photometry
4. Polarization $\Longrightarrow$ polarimetry
5. Time of observation $\Longrightarrow$ variability
6. Distribution of photons in data space $\Longrightarrow$ statistical studies

In the reality, however, not all these quantities can be measured simultaneously. Restriction is imposed by the existing instrumentation.

By observing and storing the photons of the incoming radiation typically we get a data cube defined by $(\alpha, \delta, \lambda)$. The measuring instrument has some finite resolution in respect to the parameters of the incoming radiation. Consequently, the data cube can be divided into cells of size of the resolution. The astronomical objects can be characterized by isolated domains on the α, δ plane. A real object can be more extended than one pixel in this plane. Each pixel in the α, δ plane can have a set of non-empty cells according to the different λ values. A list of non-empty pixels can be ordered into a matrix form having columns of properties (α, δ, and the set of λs) and rows referring to the serial number of objects. This structure is called the 'Data Matrix' which is the input of many multivariate statistical procedures.

Table 1: Structure of the Data Matrix: m means the number of properties and n runs over the cases.

α_1	δ_1	λ_{11}	λ_{12}	$\cdots$	λ_{1m}
α_2	δ_2	λ_{21}	λ_{22}	$\cdots$	λ_{2m}
$\vdots$	$\vdots$	$\vdots$	$\vdots$	$\ddots$	$\vdots$
α_n	δ_n	λ_{11}	λ_{12}	$\ldots$	λ_{nm}

2. Brief summary of multivariate methods

2.1. Factor Analysis

A common problem in the multivariate statistics is whether the stochastic variables described by different properties are statistically independent or can be described by a less number of physically important quantities behind the data observed. The solution of this problem is the subject of the factor analysis.

Factor analysis assumes a linear relationship between the observed and the background variables. The value (factor scores) and number of background variables, along with the coefficients of the relationship (factor loadings) are outputs of the analysis. The basic model of factor analysis can be written in the following form:

$$X_j = \sum_{k=1}^{p} a_{jk} F_k + u_j \qquad , \qquad (j = 1, \cdots, m). \tag{1}$$

In the formula above X_j means the observed variables, m is the number of properties, p is the number of hidden factors (normally $p < m$), a_{jk} denotes the factor loadings, F_k the factor scores, and u_j-s are called individual factors. The individual factors represent those parts of the observed variables which are not explained by the common factors.

A common way to solve the factor problem uses the Principal Components Analysis (PCA). PCA has many similarity with the factor analysis, however, its basic idea is different. Factor analysis assumes that behind the observed ones there are hidden variables, less in number, responsible for the correlation between the observed ones. The PCA looks for uncorrelated background variables from which one obtains the observed variables by linear combination. The number of PCs is equal to those of the the observed variables. In order to compute the PCs one has to solve the following eigenvalue problem:

$$\underline{R}\,\underline{a} = \lambda\,\underline{a} \tag{2}$$

where $\underline{R}$, $\underline{a}$ and λ mean the correlation matrix of the observed variables, its eigenvector and eigenvalue, respectively. The components of the $\underline{a}$ eigenvectors give the coefficients of the linear relationship between the PCs and the observed variables. The PC belonging to the biggest eigenvalue of $\underline{R}$ gives the most significant contribution to the observed variables. The PCs can be ordered according to the size of the eigenvalues. In most cases the default solution of the factor problem is the PCA in the statistical software packages (e.g. BMDP, SPSS). Normally, if the observed variables can be described by a less number of background variables (the starting assumption of the factor model) there is a small number of PCs having large eigenvalue and their linear combination reproduce fairly well the observed quantities. The number of large eigenvalues gives an idea on the number of the hidden factors. Keeping only those PCs having large eigenvalues offers a solution for the factor model. This technique has a very wide application in the different branches of observational sciences. For the astronomical context see Murtagh & Heck (1987).

The factor model can be used successfully for separating cosmic structures physically not related to each other but projected by chance on the same area of the sky. We will return to the details later on when dealing with case studies.

2.2. Cluster Analysis

Factor analysis is dealing with relationships between properties when describing the mutual correlations of observed quantities by hidden background variables. One may ask, however, for the relationship between cases. In order to study the relationship between cases one have to introduce some measure of similarity. Two cases are similar if their properties, the value of their observed quantities, are close to each other.

"Similarity", or alternatively "distance" between l and k cases, is a function of two X_j^l, X_j^k set of observed quantities (j is running over the properties describing a given case). Conventionally, if $l = k$, i. e. the two cases are identical, the similarity $a(X_j^l, X_j^k) = 1$ and the distance $d(X_j^l, X_j^k) = 0$. The mutual similarities or distances of cases form a similarity or distance matrix.

Forming groups from cases having similar properties according to the measures of similarities and the distances is the task of cluster analysis. There are several methods for searching clusters in multivariate data. There is no room here to enter into the details. For the astronomical context see again (Murtagh & Heck, 1987). Typical application of this procedure is the recognition of celestial areas with similar properties, based on multicolor observations. The procedure of clustering in this case is a searching for pixels on the images taken in different wavelengths but having similar intensities in the given colors.

In the following we try to demonstrate how these procedures are working in real cases.

3. Case studies

3.1. Separation of the Zodiacal Light and Galactic Dust Emission

The IRAS mission covered the whole sky in four (12, 25, 60, 100 μm) wavelengths. In particular, the 12 and 25 micron images were dominated by the thermal emission of the Zodiacal Light (ZL) having a characteristic temperature around 250 $K\hbar$. The contamination of the Galactic Dust thermic radiation by the ZL is quite serious close to the Ecliptic. Assuming that both radiation are coming from optically thin media the observed infrared intensities are sums of those coming from these two components. We may assume furthermore the distribution of the intensity of thermal radiation on the sky coming from the Galactic component has some similarities when observed at the given wavelengths and the same holds also for the ZL. Identifying the radiation coming from these two physically distinct components with the hidden variables in Eq.

Table 2: Results of factor analysis. There are two large eigen values indicating the presence of two important factors. The last two columns of the table give the a_{jk} factor coefficients for Eq. (1). (Balázs et al., 1990)

eigenvalue	cum. percent.	Variable	1. factor	2. factor
2.4818	62.0	F_{12}	0.9637	0.2089
1.3910	96.8	F_{25}	0.9917	0.0458
0.1003	99.3	F_{60}	0.3625	0.9044
0.0268	100.0	F_{100}	0.0409	0.9819

(1) and the incoming intensity with the observed ones the separation of the ZL and the Galactic radiation can be translated into the general framework of factor analysis.

In the case of the IRAS images the $\underline{R}$ correlation matrix has a size of 4×4 by cross correlating the four (12, 25, 60 and 100 μm) images. We selected a field of $15^\circ \times 15^\circ$ (corresponding to 512×512 pixels) in Perseus close to the ecliptic, containing the California Nebula, IC 348 and the Pleiades.

Solving Eq. (2) for this case we got the results summarized in Tab. 2. One can infer from this table that there are two large eigenvalues indicating the presence of two important factors. The last two columns of the table give the a_{jk} factor coefficients for Eq. (1). The first factor dominates the radiation at 12 and 25 μm while the second one does it at 60 and 100 μm. Computing the factor values from the observed data (the measured 12, 25, 60 and 100 μm intensities) one gets the two images as shown in Fig. 1, along with the originals (Balázs et al., 1991).

In order to define regions of similar physical properties we performed cluster analysis in the $\{F_1; F_2\}$ factor plane. These two factors define a two-dimensional subspace in the four-dimensional color space. The 1-st factor almost fully explains the 25 micron flux, which is heavily dominated by the Zodiacal Light and therefore represents its influence in different colors. The second factor, in contrast, describes the effect of the radiation coming from the galactic dust which produces most of the 100 micron emission. Performing cluster analysis altogether 10 regions were defined, however this figure was arbitrary. The result is given in Fig. 2. The basic features of this plot are the two 'fingers' pointing upwards and nearly horizontally. These 'fingers' may be identified with the Zodiacal Light (dominating F_l) and the galactic radiation (dominating F_2).

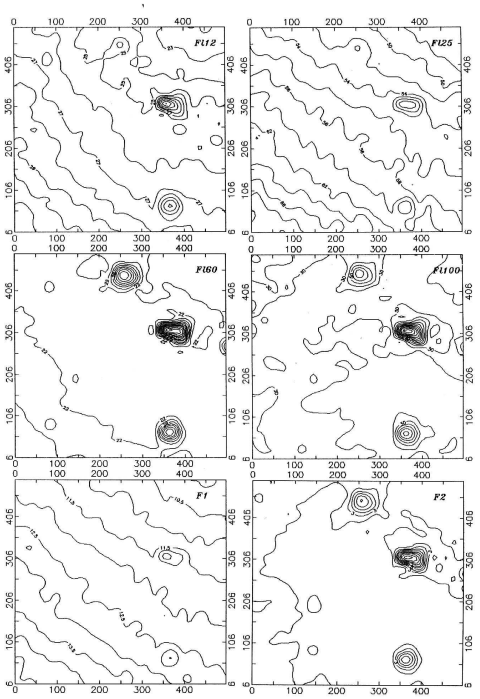

Figure 1: Input IRAS (12, 25, 60, and 100μm) images of the factor analysis and the resulted two factor pictures. The coordinates are measured in pixels. The objects are the California Nebula, IC 348 and the Pleiades, in descending order. Note the strong trend in F_1 representing the ZL while F_2 displays the Galactic component (Balázs et al., 1991).

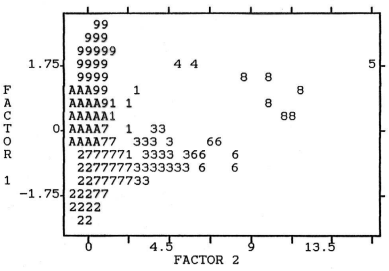

Figure 2. Character plot of regions (clusters) of similar properties in the $\{F_1; F_2\}$ factor plane. The identical symbols mean physically similar regions. The basic features of this plot are the two 'fingers' pointing upwards and nearly horizontally. These 'fingers' may be identified with the Zodiacal Light (dominating $Factor\,1$) and the galactic radiation (dominating $Factor\,2$) (Balázs et al., 1990).

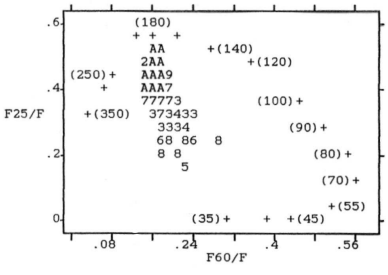

Figure 3. Distribution of duster members in the $\{F25/F; F6O/F\}$ plane. The coding of dusters is the same as in Fig. 2. The loci of dust low $\alpha = 1$ radiations of different temperatures are marked with crosses. The numbers in parentheses are the respective temperatures. Note that the wedge-shaped distribution of symbols representing real measurements points towards dust temeratures of about 40K and 200K (Balázs et al., 1990).

The dust emission is basically thermal. We computed the total infrared emission by adding the fluxes in the four bands:

$$F = F_{12} + F_{25} + F_{60} + F_{100} \tag{3}$$

Assuming a dust emission law in the form of $B(T)/\lambda^{\alpha}$ where $B(T)$ is the black body (BB) radiation at T temperature, λ the wavelength and α depends on the physical properties of the emitting dust, we put $\alpha = 1$. However, recent studies of the far infrared radiation of the ZL with the ISO satellite indicate nearly BB radiation (Leinert et al., 2002), i.e $\alpha = 0$. The specification of α influences the numerical results obtained, of course, but our goal is only to demonstrate the link between the statistical procedure and the physical quantities.

The F_i/F ratios (i is 12, 25, 60 or 100) depend only on T if a region determined by one characteristic temperature. Supposing the validity of the dust emission law given above we computed the loci of such regions in Fig. 3, marked with crosses the sources of different temperatures in the line of sight. As a consequence, the real points in Fig. 3 are not on the theoretically computed line but deviate from it according to the relative intensity of superimposed sources of different temperatures. Keeping the same coding of sources as in Fig. 2 one gets a wedge-shaped distribution of symbols representing real measurements pointing towards dust temperatures of about 40 K and 200K. This distribution can be obtained from the superimposed ZL and Galactic sources with these characteristic temperatures.

4. Separation of HI components in the field of L1780

The next case study refers to L1780, a small dust cloud at a high galactic latitude. By analyzing the profile of the HI 21 cm line it was difficult to separate the object from the background since the velocity of the cloud was very close to those of the background.

The cloud was observed with the 100 m telescope at Effelsberg at 209 positions in 82 channels. Formulating the problem of separation with the phraseology of the multivariate statistical analysis we had 209 cases and 82 properties.

Performing PCA yielded 7 eigenvalues > 1 and they were accepted as significant factors. In order to get clear-cut factor pattern we made Varimax rotation. This procedure makes use of the fact that factors are determined only up to an orthogonal transformation. Varimax rotation is an orthogonal transformation

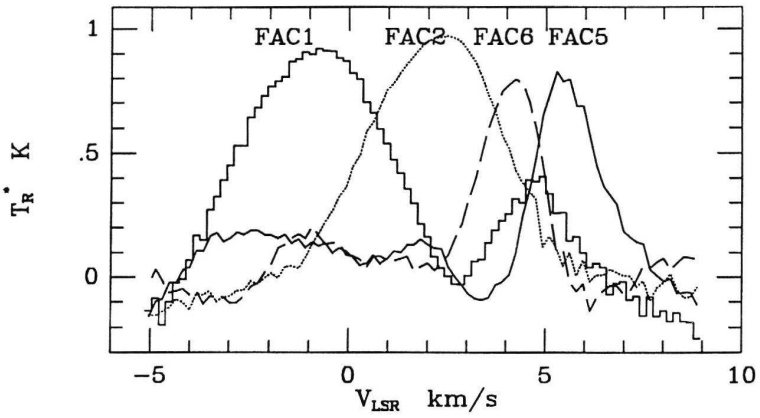

Figure 4: Results of factor analysis in L1780. The factor coefficients are displayed as functions of the channels calibrated to the velocity in the line of sight. Beside the strongest factor (FAC1), the main HI background component, those are displayed which give excess emission in the field of L1780 (FAC2, FAC5, FAC6) (Tóth et al., 1993).

which maximizes the variance of the factor coefficients and usually gives a dominant factor in each observed variables. This dominant factor makes easier to identify the factors with real physical entities.

Inspecting the pictures obtained from the factor scores we found that FAC2, FAC5 and FAC6 indicated excess HI radiation that could be associated with L1780. On the contrary, FAC1, FAC3, FAC4 and FAC7 described the background. The contributions of the different factors to the channel maps are displayed in Fig. 4. Summing up the factors related to the cloud gives the amount of HI associated to L1780 (Tóth et al., 1993).

Using the computed factors associated with the cloud we calculated the HI 21 cm spectra in some characteristic positions of L1780 along with the background as seen in Fig. 5. Note that the difference of the HI spectra across the cloud (i.e. the difference between he position a and c) indicates large scale internal motions.

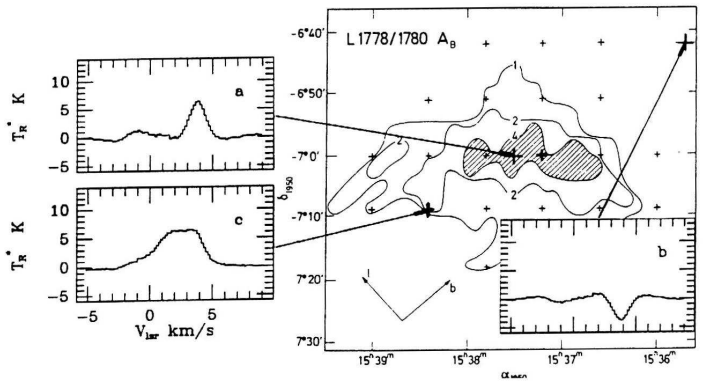

Figure 5: Distribution of the dust in L1780 as obtained from the optical extinction (A_B). The HI spectra in the inserts give velocity profiles at some characteristic parts of the cloud (a, c) and the background (b), respectively. Note that the difference of the HI spectra across the cloud (i.e. the difference between the positions a and c indicates large scale internal motions (Tóth et al., 1993).

5. Multivariate study of the Cepheus Bubble

The Cepheus Bubble was discovered in the IRAS maps (Kun et al., 1987) as a ring about 10 deg. in diameter around Cep OB2 joining several known star forming regions (S140, IC1396, S134, etc). The association of the ring with the star forming regions with known distances (between 800-900 pc) enabled one to estimate the true geometric diameter to be 140-160 pc. The dust responsible for the radiation detected by IRAS, however, is only a tiny fraction of the total mass which is mostly in the form of HI. In order to calculate the mass and internal kinematics of the bubble one of the best choice was to use neutral hydrogen observations. The integrated map of the HI channel intensities clearly showed a ring coinciding with those in the IRAS maps (Fig. 6). We used 43 HI channel maps of the region from the Dwingeloo HI sky survey (Burton & Hartman, 1994) in the [–38 km/s; +10 km/s] range.

Inspection of the channel maps (Fig. 5), starting at –38 km/s and moving towards positive radial velocities, revealed a ring structure starting at –30 km/s, becoming dominant in the [–18 km/s; –10 km/s] range and fading away

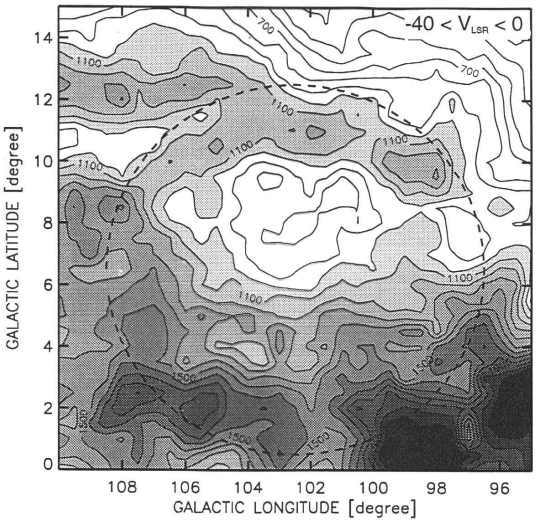

Figure 6: Integrated column density of the HI in the region of the Cepheus Bubble. A dashed circle indicates the outer boundary of the infrared ring (Ábrahám et al., 2000).

afterwards (Fig. 8). In order to separate the HI associated with the Bubble we performed factor analysis based on PCA which yielded 6 main components (see Tab. 3). The factor coefficients, similarly to the case of L1780, could be calibrated for radial velocity and are displayed in Fig. 9. The Figure clearly shows that each factor dominates a certain velocity range. Usage of the images made up from the factor scores (Fig. 10) enabled us to identify the factors in terms of different physical entities of the HI distribution. The main body of the bubble appeared in factor 2 whereas factor 3 and 5 are strong on the area where factor 2 is weak. These factors can be interpreted as different slices of an expanding shell. Identification of the factors with different physical entities of the neutral hydrogen enabled us to separate the HI associated with the Bubble and determine its mass and age (Ábrahám et al., 2000).

6. Conclusions

1. The nature of astronomical information is well suited for multivariate studies.

2. The typical procedures of multivariate methods (factor analysis, cluster analysis) can be applied succesfully for studying different structures in the

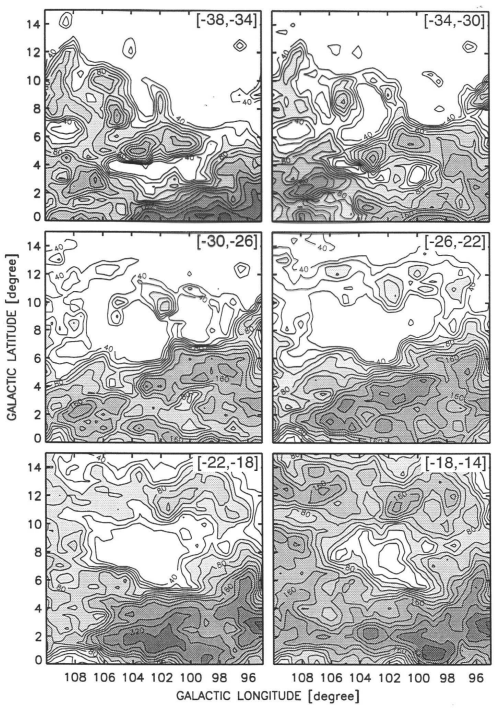

Figure 7: HI channel maps of the Cepheus Bubble in the [-38 km/s; -14 km/s] range. The ring structure appears at -26 km/s and increases in dominance at less negative velocities (Ábrahám et al., 2000).

data cubes.

3. There is no straightforward way to assign physically meaningful objects to the formal statistical results (actually this is one of the basic problems).

4. Special care is needed to separate "ghosts". In some cases physically related structures can be splitted into different mathematical structures.

5. The best results can be expected for problems where the basic mathematical assumptions (e.g. linearity and orthogonality at PCA models) are also physically meaningful.

6. A basic advantage is the existence of professional statistical packages (SPSS, SAS, S-plus, etc.)

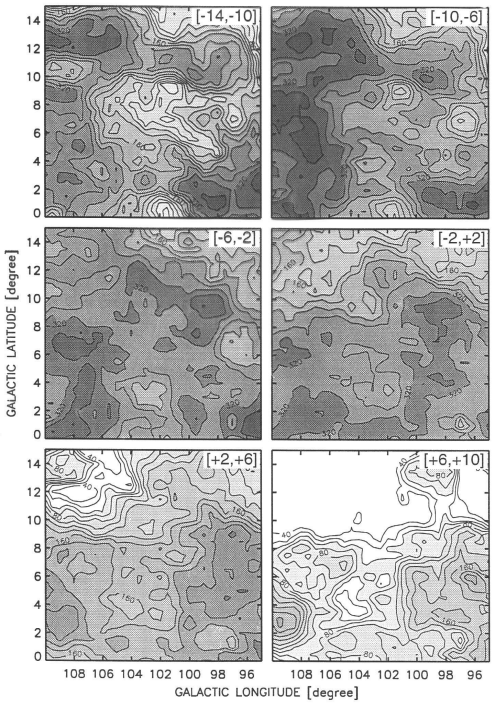

Figure 8: HI channel maps of the Cepheus Bubble in the [-14 km/s; +10 km/s] range. The ring structure fades away towards less negative velocities and completely disappears (Ábrahám et al., 2000).

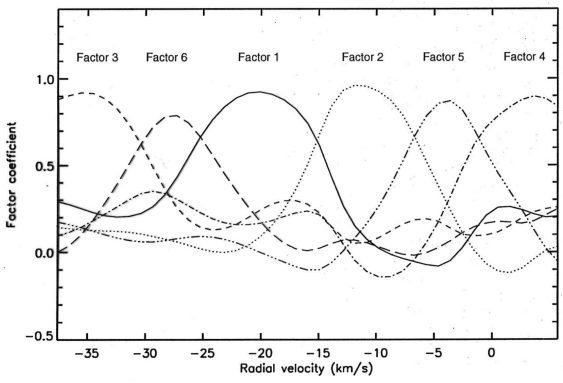

Figure 9: Dependence of the factor coefficients on the radial velocity in the Cepheus Bubble. Each factor dominates a certain range of radial velocities. The 2nd strongest factor can be associated with the main body of the ring (Ábrahám et al., 2000).

Table 3: Results of the factor analysis on the HI data of the Cepheus Bubble. There are 6 eigenvalues > 1 reproducing 95.4 % of the total variance of the data.

PC	Eigenvalue.	Pct. of Var. [%]	Cum.Pct. [%]
1	20.41	47.5	45.5
2	7.80	18.3	65.8
3	5.87	13.7	79.5
4	3.41	7.9	87.4
5	1.87	4.3	91.8
6	1.56	3.6	95.4
7	0.66	1.5	96.7
8	0.52	1.2	98.1
⋮	⋮	⋮	⋮
43	0.00	0.00	100.0

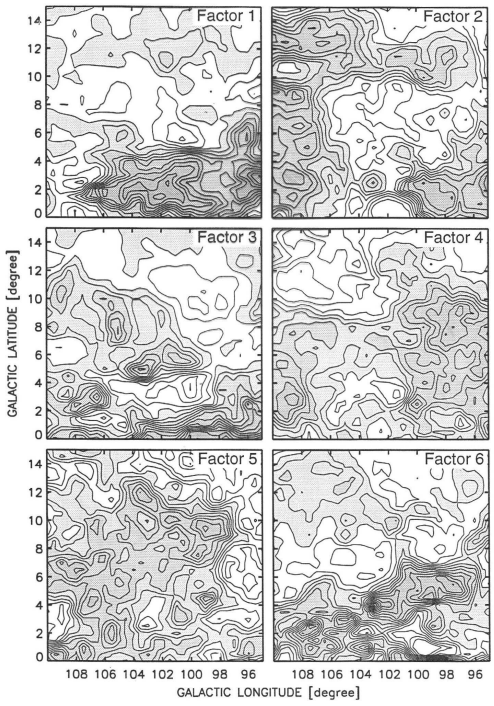

Figure 10: Images made up from the factor scores in the Bubble. The 2nd strongest factor gives the main body of the ring. Images of factors 3 and 5 are strong on the area where factor 2 is weak. These factors can be interpreted as different parts of an expanding shell (Ábrahám et al., 2000).

Acknowledgements

The author is indebted to Dr. Gábor Tusnády (Rényi Institute of Mathematics, Budapest) for the comprehensive discussions in the theory and practice of multivariate statistical methods.

References

Ábrahám, P., Balázs, L.G., Kun, M., 2000, A&A, 354, 645

Balázs, L.G., Kun, M., Tóth, V., 1990, in 'The Galactic and Extragalactic Background Radiation', IAU Symposia No. 139, eds. S. Bowyer & C. Leinert, Kluwer Academic Publishers, Dordrecht, Holland, p.214

Balázs, L.G., Tóth, L.V., 1990, in the 'Physics and Composition of Interstellar Matter', eds. J. Krelowski & J. Papaj, Institute of Astronomy Nicolaus Copernicus University, Torun , p.135

Burton, W.B., Hartmann, D., 1994, A&ASS, 217, 189

Kun, M., Balázs, L.G., Tóth, I. 1987, A&ASS, 134, 211

Leinert, C., Ábrahám, P., Acosta-Pulido, J., Lemke, D., Siebenmorgen, R., 2002, A&A, 393, 1073

Murtagh, F., Heck, A., 1987, "Multivariate data analysis", Astrophysics and Space Science Library, Dordrecht: Reidel

Tóth, L.V., Mattila, K., Haikala, L., Balázs, L.G., ASP Conf. Ser. Vol. 52, 'Astronomical Data Analysis Software and Systems II', eds. R.J. Hanisch et al., p.462

Low-Mass Star Formation Induced by the Orion–Eridanus Bubble

M. Kun[1], **S. Nikolić**[2]

[1]Konkoly Observatory
H-1525 Budapest, P.O. Box 67, Hungary
E-mail: kun@konkoly.hu
[2]Onsala Space Observatory
S-439 92 Onsala, Sweden
E-mail: silvana@oso.chalmers.se

Abstract

During a spectroscopic survey performed with the Nordic Optical Telescope in La Palma we found five classical T Tauri stars in the small, high latitude molecular clouds associated with the reflection nebula IC 2118. The star-forming clouds are located at the outer boundary of the Orion star forming region, at a mean galactic latitude of -28°. Their positions in space and cometary shapes suggest their interaction with the Orion SFR. Using spectroscopic and near-infrared photometric data we determined the positions of the newly discovered pre-main sequence stars in the HRD. Comparison of the results with evolutionary models has shown that the masses of these stars are between 0.3–0.8 $M_{\odot}$ and their ages are close to 10^6 yrs. They are roughly coeval and significantly younger than the known WTTS of the same region. We conclude that the birth of the molecular clouds and the stars was probably induced by the interaction of the Orion–Eridanus Bubble with some small, diffuse high-latitude HI clouds.

KEYWORDS: *ISM: supershells, high-latitude molecular clouds, Orion–Eridanus Bubble, star formation–stars: pre-main sequence*

1. Introduction

The Orion–Eridanus Bubble is a giant supershell blown by the high-mass stars of the oldest subgroup of the Orion OB1 association, Orion OB1a (Brown et al., 1995). Its present radius is about 140 pc, and has a mean expansion velocity of $\sim$40 km s^{-1}. It shows up as a fragmented HI shell with angular extent more than 40°, associated with several Hα loops and filaments, including the Barnard Loop. The interior of the bubble is filled with low density ionized gas which is traced by soft X-ray emission and by ultraviolet absorption lines in the spectra of background stars. This large volume of tenuous gas surrounding Orion OB1

is often referred to as *Orion's cloak* (Cowie, 1982). The total mass of the HI shell is estimated to be about $2.3 \times 10^5\,M_\odot$, and its kinetic energy is about 3.7×10^{51} erg (Brown et al., 1995). The supershell expands into the surrounding interstellar medium, thereby creating favorable circumstances for induced star formation. Identification of individual interstellar features associated with the bubble, hovewer, requires careful study of distances of the objects in question, because the size of this supershell is comparable with its distance from us.

The reflection nebula IC 2118 near Rigel (*Witch head nebula*) is a region associated with the nearest wall of the supershell. Its galactic coordinates are $205^\circ \leq l \leq 210^\circ$, $-30^\circ \leq b \leq -25^\circ$. The distance of the nebula from the Sun is 210 ± 20 pc (Kun et al., 2001).

In this case the well-known distance of the illuminating star makes it possible to determine the distance of the illuminated clouds. Molecular clouds associated with IC 2118 were described by Yonekura et al. (1997) and Kun et al. (2001). The wind-blown appearance of the bright reflection nebula and the cometary shapes of the associated molecular clouds suggest that the region is dynamically influenced by the association Orion OB1: though the main source of illumination is Rigel, the heads of the cometary clouds point towards the north-east, to the centre of the association. This morphology suggests the scenario in which the HI clouds have been compressed from the direction of Orion OB1. The association, however, is some 150 pc more distant than IC 2118. Therefore the interaction of these objects is probably mediated by the high pressure of the bubble surrounding the association.

Objective prism search for Hα emission stars in the region of IC 2118 suggested that low-mass stars might have been born in these high-latitude molecular clouds (Kun et al., 2001). In this paper we present the results of spectroscopic observations that confirm the presence of pre-main sequence stars in the molecular clouds associated with IC 2118.

2. Observations

We observed the spectra of stars selected as possible Hα emission objects in objective prism Schmidt plates in January 2001 with ALFOSC (*Andalucia Faint Object Spectrograph*) on the Nordic Optical Telescope in La Palma. Using grism 8 with a 1 arcsec slit provided a spectral resolution $\lambda/\Delta\lambda \approx 2200$ in the wavelength interval 5800–8300 Å. This spectral region contains both the Hα and the LiI λ6708 lines, crucial for identification of T Tauri type stars, as well as several absorption features suitable for spectral classification (Kirkpatrick et al.,

1991). Spectra of helium and neon lamps were observed before and after each stellar observation for wavelength calibration. For spectral classification purposes we observed a series of spectroscopic standards. We reduced the spectra using the standard IRAF routines. Spectral and luminosity classes were determined using the criteria established by Kirkpatrick et al. (1991) and Martín & Kun (1996).

3. Results

We found five stars closely confined to the clouds which have shown several characteristics of pre-main sequence nature, as well as two stars having weak Hα emission ($EW(H\alpha)$ <5 Å) but no Li I absorption. Figure 1 displays the distribution of the pre-main sequence stars identified during the spectroscopic survey with respect to the molecular clouds, and Fig. 2 shows their spectra, normalized to the continuum. Several emission lines attributed to circumstellar matter can be observed in the spectra, such as the [O I] lines at 6300 and 6360 Å, [N I] at 6583 Å, [S II] at 6717 and 6731 Å, as well as the emission lines of neutral helium at 5875 Å and 6678 Å.

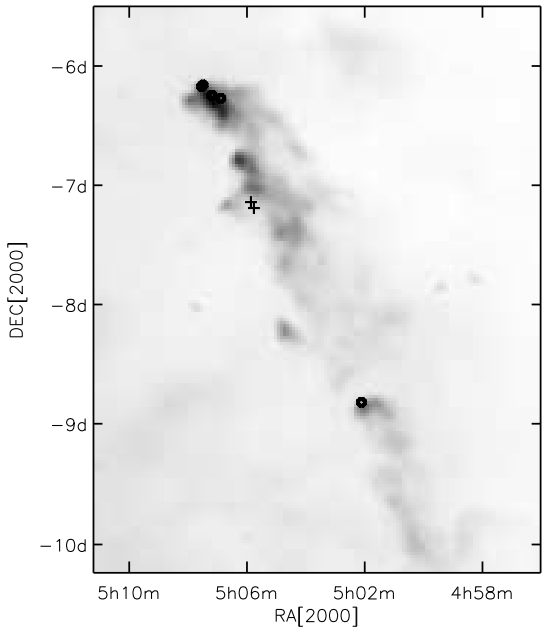

Figure 1: Location of classical T Tauri stars (circles) and weak-line Hα emission stars (crosses) with respect the molecular clouds indicated by the distribution of 100 μm emission observed by IRAS in the region of IC 2118.

Table 1: T Tauri stars in IC 2118

2MASS	Sp.T.	J	$J-H$	$H-K$	$W(\mathrm{H}\alpha)$	$W(\mathrm{LiI})$
0502063−085046	M2IV	10.987	0.782	0.441	−60.72	0.28
0506030−071547	M4V	11.535	0.538	0.285	−4.11	0.03
0506091−071239	M3V	10.888	0.557	0.246	−0.97	0.00
0506535−061712	K7IV	11.182	1.255	0.754	−112.35	0.53
0507115−061509	M0V	13.009	1.730	1.225	−293.20	1.19
0507301−061015	K5IV	10.839	1.254	0.963	−79.35	0.37
0507306−061059	K7IV	10.127	1.081	0.743	−13.47	0.41

J, H, and K magnitudes of the pre-main sequence stars were obtained from the 2MASS Second Incremental Survey Catalog (IPAC, 2000). We used these data to place the stars on the Hertzsprung–Russell diagram. Table 1 shows the 2MASS identifications, spectral types, J, H, and K magnitudes, Hα and LiI equivalent widths of the new pre-main sequence objects. Figure 3 displays their positions on the $(H-K)$ vs. $(J-H)$ color-color diagram together with the lines indicating the position of zero-age main-sequence, the giant branch, direction of the interstellar reddening and the locus of classical T Tauri stars determined by Meyer et al. (1997).

In order to place the stars on the HRD their effective temperatures and bolometric luminosities are to be determined. T_{eff} comes from the spectral type, according to *e.g.* Kenyon & Hartmann (1994), whereas L_{bol} can be determined from the near-infrared photometric data. For this purpose we make the widely used assumption that the total emission of our target stars in the J band originates from the photosphere (e.g. Hartigan et al., 1994). Thus the color index $J-H$ can be written as

$$J-H=(J-H)_0+E_{\mathrm{CS}}(J-H)+E_{\mathrm{IS}}(J-H),$$

where $(J-H)_0$ is the true photospheric color of the star, $E_{\mathrm{CS}}(J-H)$ is the color excess due to the emission from the circumstellar disk in the H band, and $E_{\mathrm{IS}}(J-H)$ is the color excess originating from the interstellar extinction in the H band.

The locus of unreddened T Tauri stars in the $H-K$ vs. $J-H$ color-color diagram (Meyer et al., 1997) allows us to determine $E_{\mathrm{IS}}(J-H)$, the interstellar

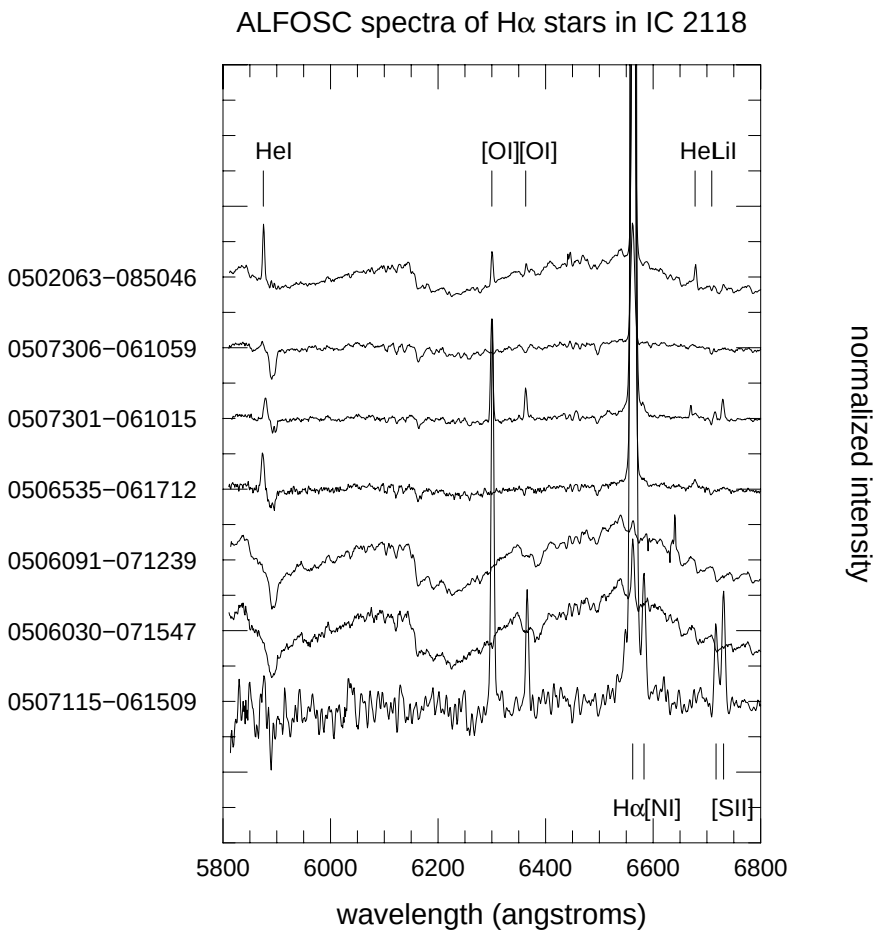

Figure 2: Spectra of the new pre-main sequence stars in IC 2118 in the wavelength region 5800–6800 Å.

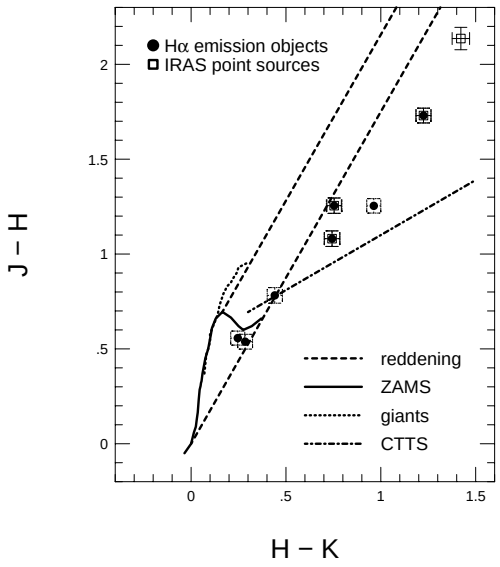

Figure 3: Positions of the T Tauri stars in IC 2118 in the $J-H$ vs. $H-K$ diagram. Loci of zero-age main sequence, giant branch, and classical T Tauri stars, as well as the slope of interstellar reddening are indicated.

component of the $E(J-H)$ color excess. The bolometric luminosities of the stars were derived by using the interstellar extinction law $A_{\rm J} = 2.65 \times E_{\rm IS}(J-H)$, given by Rieke & Lebofsky (1985) and the bolometric corrections tabulated by Hartigan et al. (1994).

The positions of our target stars in the HRD are shown in Fig. 4 together with evolutionary tracks and isochrones given by D'Antona & Mazzitelli (1994) (model 1). It can be seen that the masses of these stars are in the 0.3–0.8 $M_\odot$ interval, and they are grouped along the isochrone corresponding to a mean age of 10^6 years, comparable to the age of the youngest subgroup of Orion OB1.

4. Conclusions

We found five classical T Tauri stars in the molecular clouds associated with IC 2118. We estimated their masses and ages, and found them to be nearly coeval, at a mean age of 10^6 yrs. Our results suggest that the T Tauri stars associated with IC 2118 are significantly younger and less massive than most of the weak-line T Tauri stars discovered by ROSAT (Alcalá et al., 1998) in the Orion–Eridanus region. Both the small, high-latitude clouds and the low-mass stars in them have most probably been produced by the interaction of the Orion–Eridanus Bubble with diffuse HI clouds.

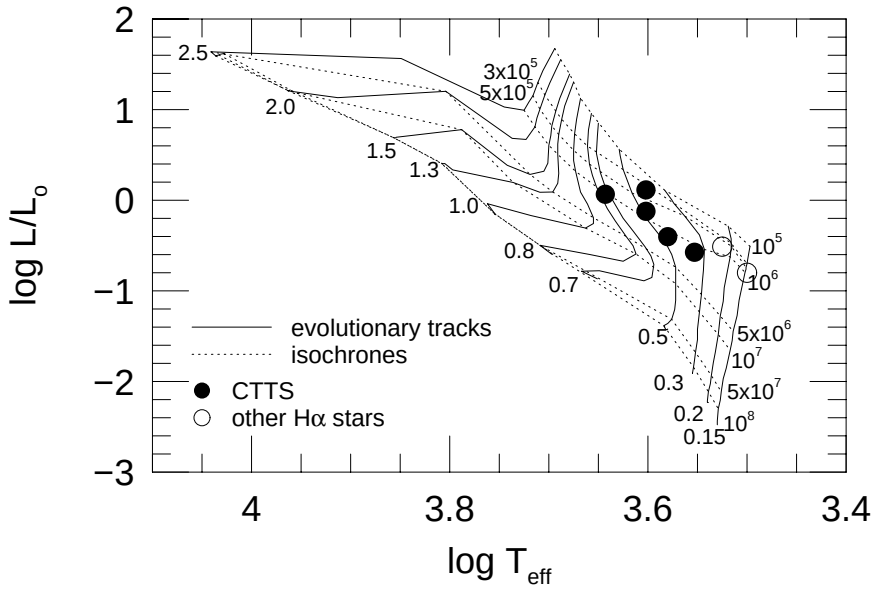

Figure 4: The T Tauri stars of IC 2118 in the HRD. Solid lines indicate the isochrones and dashed lines show the evolutionary tracks from D'Antona & Mazzitelli's (1994) model 1.

Acknowledgements

This work is based on observations with Nordic Optical Telescope operated on the island of La Palma jointly by Denmark, Finland, Iceland, Norway, and Sweden, in the Spanish Observatorio del Roque de los Muchachos of the Instituto de Astrofisica de Canarias. The data presented here have been taken using ALFOSC, which is owned by the Instituto de Astrofisica de Andalucia (IAA) and operated at the Nordic Optical Telescope under agreement between IAA and the NBIfAFG of the Astronomical Observatory of Copenhagen. This research has been supported by the Hungarian grants OTKA T022946 and T034584, and also partly funded by the Ministery of Science and Technology of Serbia grant P1191.

References

Alcalá, J.M., Chavarria-K. C., Terranagra, L., 1998, A&A 330, 1017
Brown, A.G.A., Hartmann, D., Burton, W., 1995, A&A 300, 903
Cardelli, J., Clayton, G.C., Mathis, J., 1989, ApJ 345, 245
Cowie, L.L., 1982, Symposium on the Orion Nebula to Honor Henry Draper, eds. A.E. Glassgold, P.J. Huggins, E.L. Schucking, Ann. NY Acad. Sci. 395, p.17
D'Antona F. & Mazzitelli I. 1994, ApJS 90, 467
Hartigan P., Strom K.M., Strom S.E., 1994, ApJ 427, 961
Hartmann, D., Burton, W.B., 1997, Atlas of Galactic Neutral Hydrogen, Cambridge Univ. Press
Kenyon, S.J., Hartmann, L., 1994, ApJS 101, 117
IPAC 2000, The 2MASS Second Incremental Catalog, URL:"http://www.ipac.caltech.edu
Kirkpatrick, J.D., Henry, T.J., McCarthy, D.W., 1991, ApJS 77, 417
Kun, M., Aoyama, H., Yoshikawa, N., Kawamura, A., Onishi, T., Yonekura, Y., Fukui, Y., 2001, PASJ 53, 1063
Martín, E.L., Kun, M., 1996, A&AS 116, 467
Meyer, M.R., Calvet, N., Hillenbrand, L.A. 1997, AJ 114, 288
Rieke, G.H., Lebofsky, M.J., 1985, ApJ 288, 618
Yonekura, Y., Hayakawa, T., Mizuno, N., Mine, Y., Mizuno, A., Ogawa, H., Fukui, Y., 1999, PASJ 51, 837

Study of Pre-Main Sequence Stars Born in LDN 1251

M. Eredics[1], M. Kun[2]

[1] Eötvös Loránd University
H-1518 Budapest, P.O.Box 32., Hungary
[2] Konkoly Observatory of the Hungarian Academy of Sciences
H-1525 Budapest, P.O.Box 67.
E-mail: eredicsm@astro.elte.hu, kun@konkoly.hu

Abstract

We observed the spectra of Hα emission stars in the molecular cloud L1251 using the CAFOS spectrograph on the 2.2 m telescope of Calar Alto Observatory. We found 7 pre-main sequence stars born in the cloud and determined their spectral and luminosity classes. These spectroscopic data, supplemented with near-infrared (JHK) magnitudes allowed us to place these stars in the HR diagram. This paper discusses the evolutionary status of star formation in LDN 1251.

1. Introduction

Observational studies of dark clouds aimed at finding low mass star formation and the evolutionary status of young stellar objects have a long history. Observations of Lynds 1251, a part of the Cepheus Flare, located at 300±30 pc Kun (1998) from the Sun have shown this region to be forming low-mass stars at high efficiency. Several Hα emission stars, probable pre-main sequence stars born in LDN 1251, have been found here (Grasdalen et al. 1973; Kun & Prusti 1993). In this paper, we present the spectral and luminosity classes for 8 pre-main sequence candidates. The placement of the stars on the Hertzsprung–Russell diagram allows a conservative estimate of the age of LDN 1251 as well.

2. Results

We studied the spectra of 8 Hα emission star candidates in the molecular cloud LDN 1251 and determined their spectral types. Spectral types can be estimated using the strength of molecular bands and presence of atomic lines. The observed stars are late-K and M type objects, therefore we set them against G, K, M standards observed with the same resolution, and Pickles' (1998) spectral flux

library data. Spectral types were estimated using the depths of several molecular bands at λ7000–7200 Å (Kirkpatrick et al.1991) and the Na I at λ5890 Å and λ5896 Å.

Hα emission and Li I absorption are the most important indicators of youth of solar type stars. We measured the equivalent width of Hα and Li I λ6707 Å. We found that all but one our programme stars show Hα and Hβ emission, and the emission lines show inverse P Cygni profile except in Hα 1. We found neither Hα emission nor Li absorption in the spectrum of Hα 41. This star is probably a foreground object not related to the cloud, therefore we omitted it from further studies. Li I absorption was neither detected in the spectrum of Hα 2 due to the low S/N. We also identified the forbidden lines [OI] $\lambda\lambda$ 6300Å 6364Å in the spectra of Hα 1, Hα 44 and Hα 45, and [SII] at $\lambda\lambda$ 6717Å 6731Å in Hα 1. He I emission is also present in most spectra. Fig. 1 shows the observed spectra in the wavelength region 5800–7800 Å. The $J-H$ vs. $H-K$ two-colour diagram is presented in Fig. 2.

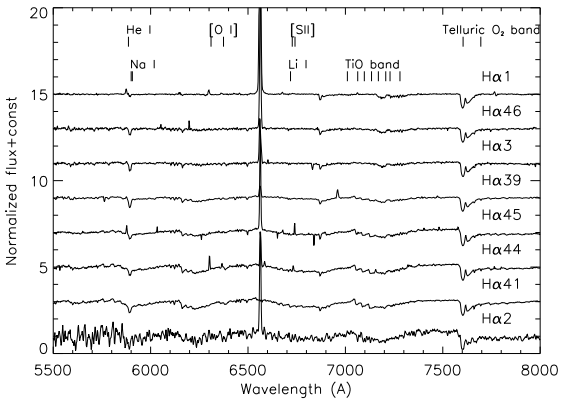

Figure 1: Spectra of the PMS stars in L 1251 in the wavelength region 5800–7800 Å.

In order to place the stars in the HRD we estimated their effective temperatures and bolometric luminosities. Effective temperatures can be obtained directly from the spectral types of the stars Hartigan et al. (1994). The J, H and K magnitudes of the stars were used to determine the bolometric luminosities with the assumption that the whole flux at 1.25μm (J band) comes from the stellar photosphere. Then $J - M_{\rm J} = 5\log r - 5 + A_{\rm J}$ and $M_{\rm bol} = M_{\rm J} + BC_{\rm J}$ were used, where $r = 300 \pm 30$ pc is the distance of LDN 1251 Kun (1998), $A_{\rm J} = 2.635 E_{\rm J-H}$ is the interstellar absorption in the J band Rieke & Lebofsky (1985), and $BC_{\rm J}$ is the bolometric correction (Hartigan et al. 1994). The results

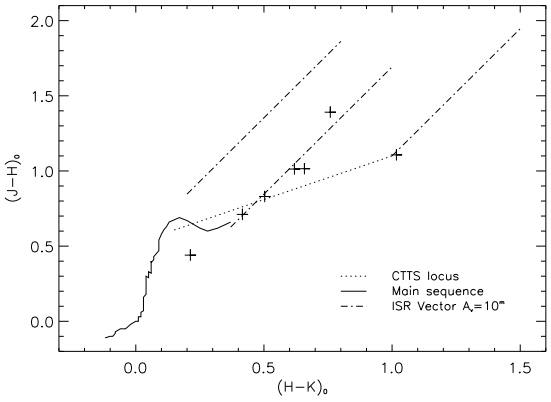

Figure 2: Positions of the T Tauri stars in L 1251 in the $J-H$ vs. $H-K$ diagram. Loci of zero-age main sequence and classical T Tauri stars, as well as the slope of interstellar reddening are indicated.

Table 1: Results of spectroscopy and photometry

Hα star	Sp ±1	EW[Å] [Hα]	[Li I]	J–H	H–K	$\log T_{eff}$	$\log(L/L_\odot)$	M $[M_\odot]$	age [Myr]
1	K5	−96.07	0.24	1.391	0.759	3.643	0.668	0.6	0.2
2	M2$\leq$	−42.18	–	1.013	0.619	$\leq$3.580	≤ -0.205	$\leq$0.4	0.7
39	M0	−5.90	0.35	1.015	0.658	3.580	−0.325	0.4	1
3	K7	−24.35	0.41	–	–	–	–		
41	M2	–	–	0.440	0.213	–	–	–	–
44	M1.5	−12.12	0.30	0.711	0.416	3.553	−0.687	0.4	2
45	M1	−37.22	0.26	0.830	0.503	3.562	−0.445	0.4	1
46	K5	−60.22	0.35	1.107	1.017	3.643	−0.077	0.8	2

of spectroscopy and photometry are shown in Table 1, and the positions of the programme stars in the HRD are displayed in Fig. 3.

3. Conclusions

We examined basic spectroscopic properties and near-infrared data of 8 pre-main sequence star candidates in the cloud LDN 1251. We confirmed the pre-main sequence nature of 7 of them. All the seven pre-main sequence stars are low mass (0.3-0.8 $M_\odot$) objects, and their spectra show classical T Tauri features. The Li absorption in the spectra and their positions in the HRD indicate that they are young objects, having ages of 1–2 million years. By the estimated age of Hα 46 we think that the cloud is at least 2×10^6 yr old. The inverse P Cygni profile in the Hα emission (except Hα 1) suggests that gathering of mass from

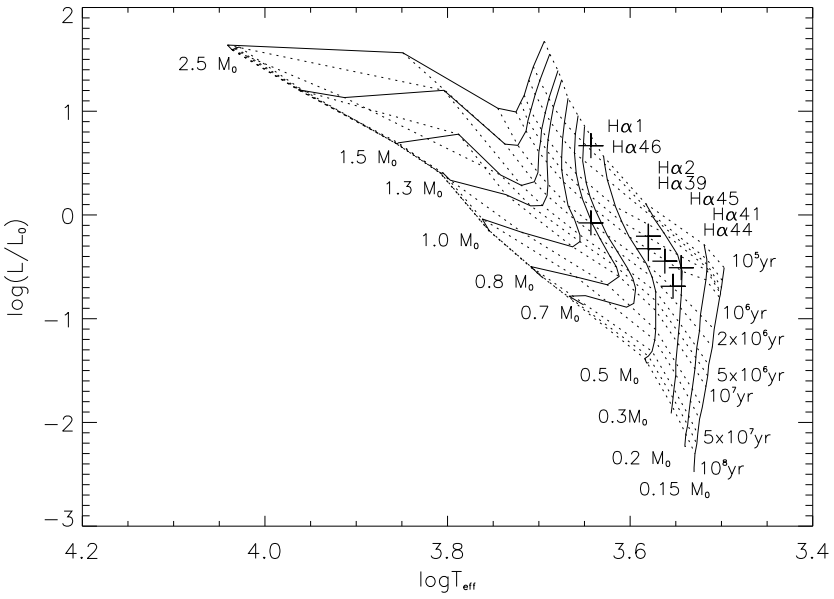

Figure 3: The T Tauri stars of L 1251 (crosses) in the HRD. Dotted lines indicate the isochrones and solid lines show the evolutionary tracks from D'Antona & Mazzitelli's (1994) model 1.

the accretion disks has not been finished in the Hα stars yet.

Acknowledgements

This research is based on spectroscopic observations obtained in the German-Spanish Astronomical Centre, Calar Alto, operated by the Max-Planck-Institute for Astronomy, Heidelberg, jointly with the Spanish National Commission for Astronomy, as well as on near-infrared observations taken at TIRGO (Gornergrat, Switzerland). TIRGO is operated by CAISMI-CNR Arcetri, Firenze, Italy. We acknowledge support by the OTKA grant T034584.

References

D'Antona, F., Mazzitelli, I., 1994, ApJS 90, 467
Grasdalen, G.L., Kuhi, L.V., Harlan, E.A., 1973, PASP 85, 193
Hartigan, P., Strom, K.M., Strom, S.E., 1994, ApJ 427, 961
Kirkpatrick, J.D., Henry, T.J., McCarthy, Jr., D.W., 1991, ApJS 77, 417
Kun., M., 1998, ApJS 115, 59
Martín, E.L., Kun., M., 1996, A&AS 116, 467
Kun., M., Prusti, T., 1993, A&A 272, 235
Meyer, M.R., Calvet, N., 1997, AJ 114, 288
Pickles, A.J. 1998, PASP 110, 863
Rieke, G.H., Lebofsky, M.J., 1985, ApJ 288, 618

Near-Infrared Study of Large Bok Globules

T. Khanzadyan

Armagh Observatory
College Hill, Armagh BT61 9DG, Northern Ireland, UK
E-mail: tig@star.arm.ac.uk

Abstract

We present results from a near-infrared study of CB 3, CB 34, CB 39 and CB 54 as a part of an ongoing project, which is set to determine how Bok globules form, evolve and disperse.

Our observations have revealed the presence of active star formation in CB 3, CB 34 and CB 54, by the discovery of new knots in the H_2 1-0 S(1) emission line images.

We have discovered no indication of star formation in the Bok globule CB 39 which may suggest that this globule is in an early stage of evolution. Meanwhile the globules CB 3, CB 34 and CB 54 are obviously in their later stages of evolution.

Keywords: *infrared: ISM – stars: formation – ISM: jets and outflows – ISM: clouds*

1. Bok Globules

Bok globules are dark patches on the sky against the background of stars, which have small angular extent and were stated as possible sites of star formation (Bok & Reilly, 1947). This statement has been confirmed recently by the work of Yun & Clemens (1990), who actually found manifestations of active star-formation in some globules.

The Catalouge of Northern Bok Globules has been published by Clemens & Barvainis (1988, hereafter CB88). The average catalogue members are small ($\approx$0.7 pc in diameter), with average masses of $\approx 10\,M_\odot$ and nearby ($d \leq 600$ pc; Bok, 1977; Leung, 1985; Launhardt & Henning, 1997). But CB88 contains some objects (e.g. CB 3, CB 34, CB 39, CB 54, CB 205) which are situated beyond 1 kpc and therefore are bigger in size ($\approx$2 pc) and larger in mass up to $120\,M_\odot$ in the case of CB 205 (Launhardt & Henning, 1997; Huard et al., 2000).

The importance of Bok globules is that they are sites of low-mass star formation (see Yun & Clemens, 1990; Khanzadyan et al., 2002). This is very important, because if there are some 10^5 globules in our Galaxy (Clemens et al., 1991), and we assume an average lifetime of 10^6 yrs and mass of $10\,M_\odot$ for them

(Launhardt & Henning, 1997), then a total mass of $10^{10}\,M_{\odot}$ could be processed through them during the lifetime of the Galaxy. This leads us to the conclusion that many field stars including our Sun, as well as T-Tauri stars may find their origin in Bok globules (Yun et al., 1997; Launhardt & Henning, 1997).

LBG vs. SBG: Large Bok Globules (LBGs) are sites for multiple and high-mass star formation, which tends to be a continuous process rather than a relatively instantaneous event like star formation in Small Bok Globules (SBGs) (Knee & Sandell, 2000; Motte et al., 1998). In LBGs powerful outflows, ejected from protostars interact with the globule material and are detectable even at the outskirts. In contrast to SBGs, which are nearby, outflows are not detected due to low column density and big outflow extent. So by detecting outflows from LBGs we are able to trace them back to the globule and associate with protostars (Khanzadyan et al., 2002).

2. Observations and Data Reduction

Observations of Bok globules were carried out during the nights of 7-10 December, 2000 using the Omega Prime (Bizenberger et al., 1998) infrared camera installed on the Calar Alto 3.5m telescope, Almeria, Spain. Omega Prime is equipped with a Rockwell 1024 × 1024 pixel HAWAII array detector. It provides a pixel scale of 0.4 arcsec/pixel and a total field of view of 6.8 × 6.8 arcmin^2 on the sky. Table 1 summarizes the observations.

Table 1: Log of the observations.

Object Name	R.A. (2000)	Decl. (2000)	Observed in Filters	seeing (arcsec.)
CB 3	$00^h28^m46^s$	$+56°42'06''$	K_s, H_2	1.5, 1.4
CB 34	$05^h47^m02^s$	$+21°00'10''$	J, H, K_s, H_2	1.5, 1.4, 1.2, 1.8
CB 39	$06^h02^m00^s$	$+16°31'00''$	K_s, H_2	1.7, 1.4
CB 54	$07^h04^m21^s$	$-16°23'18''$	J, H, K_s, H_2	1.5, 1.7, 1.6, 1.9

The data reduction and mosaicing proceeded through standard routines using several IRAF packages. In the later stage several packages from STARLINK software, such as CCDPACK and KAPPA, has been used for comparison of results and for correcting the array defects (Khanzadyan et al., 2002).

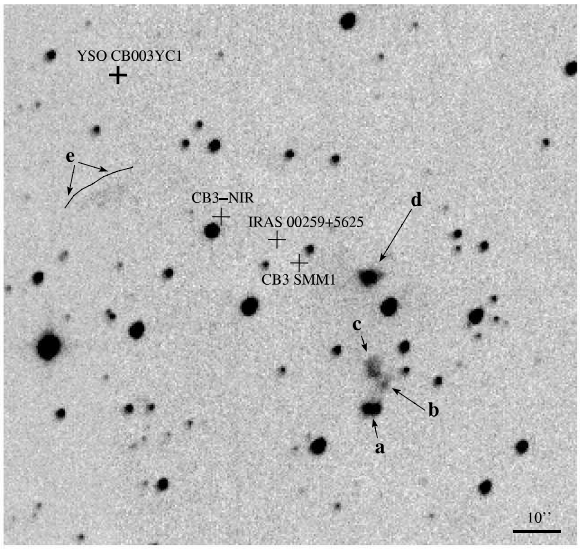

Figure 1: The central part of globule CB 3 in H_2 + cont. Newly found objects are labeled by letters **a** to **e**. The relative positions of several known sources are indicated on the image. The total integration time of this frame is 1120 seconds.

3. Results and Discussion

We found new H_2 excited objects in CB 3 marked by letters **a** to **e** in Fig. 1. The globule is excluded from the Bok globule study by Launhardt & Henning (1997) due to its large distance and mass, although it has a mass of $\approx$110 $M_\odot$, whereas CB 34 and CB 205, which are included, have masses of $\approx$80 $M_\odot$ and $\approx$120 $M_\odot$ (Huard et al., 2000).

CB 34 displays extremely well aligned chains of knots extending from sub-millimetre cores till the outskirts of the cloud, where they disappear without any trace of terminating bow shocks, due to lower density there (see Fig. 2).

CB 39 has several VLA sources in it and does not show any outflow activity (see Fig. 3), which may suggest relatively early stage of evolution.

The new near-infrared knots in CB 54 prove the active nature of cloud and indicate the advanced stage of its evolution (see Fig. 4).

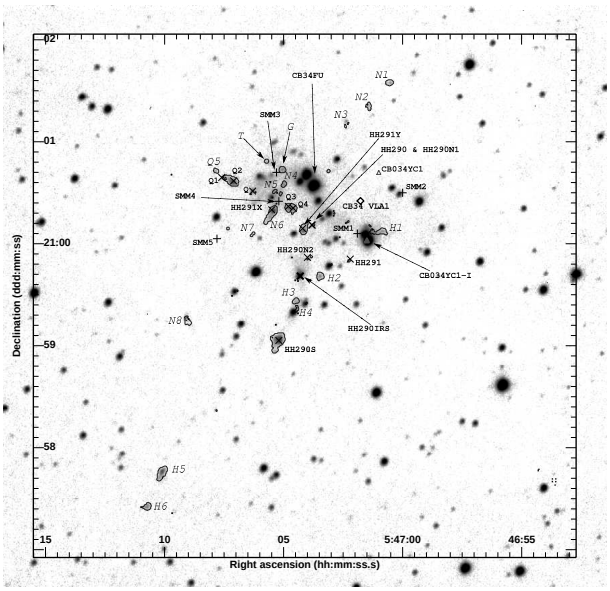

Figure 2: The central part of CB 34 in H_2. Total integration time of this frame is 3800sec. Crosses are SMM objects from Huard et al. (2000) and the asterixs are HH objects and H_2 knots discovered by Moreira & Yun (1995). CB34 VLA1 is marked by a diamond (Yun et al., 1996). The YSOs CB034YC1 and CB034YC1-I (triangles) are from Yun & Clemens (1994). Our discovered objects are indicated as chains of letters H and N as well as G and T. A further Q knot has been found – Q5.

4. Summary

CB 3, CB 34 and CB 54 are in advanced stage of evolution. We have discovered outflows from all of them by detecting their interaction with their environment.

We discovered no indication of active star formation in CB 39, which may suggest that the globule is in an early stage of evolution.

We suggest to classify CB 3 as a typical member of LBGs and therefore to connect it to the main evolutionary scenario of Large Bok Globules, if it exists.

Is there any sequence of LBGs and SBGs? Possibly LBGs are separate group of objects and should be treated apart from SBGs.

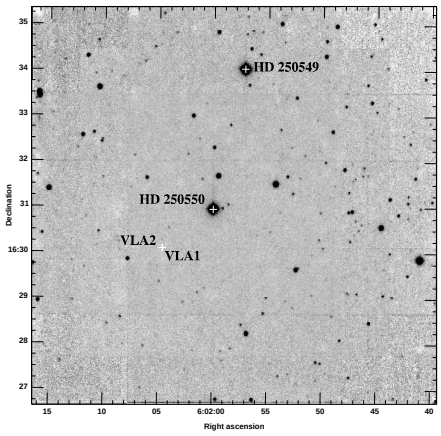

Figure 3: CB 39 in H_2 with total integration time of 1120 seconds.

Acknowledgements

Research at Armagh Observatory is grant-aided by the Department of Culture, Arts and Leisure for Northern Ireland.

References

Bizenberger, P., McCaughrean, M.J., Birk, C., Thompson, D., Storz C., 1998, SPIE 3354, 825
Bok, B.J., Reilly, E.F., 1947, ApJ 105, 255
Bok, B.J., 1977, PASP 89, 597
Clemens, D.P., Barvainis, R.E., 1988, ApJS 68, 257
Clemens, D.P., Yun, J.L., Heyer, M.H., 1991, ApJS 75, 877
Huard, T.L., Weintraub, D.A., Sandell, G., 2000, A&A, 362, 635
Khanzadyan, T., Smith, M.D., Gredel, R., Stanke, T., Davis, C.J., 2002, A&A 383, 502
Knee, L.B.G., Sandell, G., 2000, A&A 361, 671
Launhardt, R., Henning, Th., 1997, A&A 326, 329
Leung, C.M., 1985, Protostars and Planets II, eds. Black, D.C. & Matthews, M.S., Univ. of Arizona Press, Tucson, p.104
Moreira, M.C., Yun, J.L., 1995, ApJ 454, 850
Motte, F., Andre, P., Neri, R., 1998, A&A 336, 150

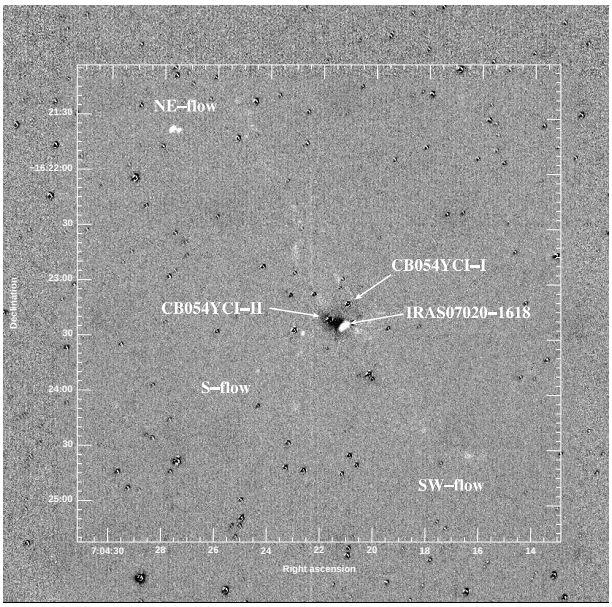

Figure 4: CB 54 in H_2-Continuum. Total integration in H_2 is 2700 seconds.

Yun, J.L., Clemens, D.P., 1990, ApJ 365, L73
Yun, J.L., Clemens, D.P., 1994, ApJS 92, 145
Yun, J.L., Moreira, M.C., Torrelles, J.M., Afonso, J.M., Santos, N.C., 1996, AJ 111, 841
Yun, J.L., Moreira, M.C., Alves, J.F., Storm, J., 1997, A&A 320, 167

Cold Dust in Luminous Star-Forming Regions

O. Krause, R. Vavrek, U. Klaas, L.V. Tóth, D. Lemke, M. Stickel

Max-Planck-Institut für Astronomie
Königstuhl 17, D-69117 Heidelberg, Germany
E-mail: okrause@mpia.de

Abstract

Using the 170 μm ISOPHOT Serendipity Survey (ISOSS) we are searching for high-mass star forming regions. Our sample consists of cold and luminous ISOSS sources coinciding with embedded young stellar objects detected by the MSX, 2MASS and IRAS infrared surveys. The large amount and low temperature of gas and dust, which has not been dispersed, indicates a recent beginning of the ongoing star formation. (Sub)millimeter and infrared follow-up observations confirmed the early evolutionary stage in two candidate regions.

Keywords: *stars: formation – ISM: clouds, dust – instrument: ISO, ISOPHOT*

1. Searching for the earliest stages of high-mass star formation

Massive stars form in clusters and the initial conditions for their birth are expected to be found in dense ($N(H_2) \sim 10^6$ cm^{-3}), cold (T $\sim$ 15 K) and massive (M $\sim$ 5000 $M_\odot$) molecular cloud cores (Evans et al. 2002). Due to the short evolutionary time scales of high-mass star formation such objects are rare. Since the spectral energy distributions of these cloud cores are expected to peak beyond 100 μm, far-infrared and (sub)millimeter continuum surveys are well suited for their identification.

The 170 μm ISOPHOT (Lemke et al. 1996) Serendipity Survey (ISOSS, Bogun et al. 1996) is the largest high spatial resolution survey performed in the far-infrared beyond the IRAS 100 μm band. In order to discover very young star forming regions and their parental clouds, we selected luminous and compact sources with a flux ratio $S_{170\mu m}/S_{100\mu m} > 2$ from the ISOSS data base. These criteria imply a high mass and low temperature of the cold ISM in the objects. Since the clustered mode of massive star formation commonly involves young stellar objects of different evolutionary stages, we require the presence of embedded compact sources with a thermal infrared excess as indicated by the 2MASS and MSX infrared surveys. The latter criterion avoids the confusion

with cold interstellar cirrus, which becomes severe at 170 μm. About 200 sources have been identified using our method and we present here results from follow-up observations of two objects.

2. Multi-wavelength follow-up observations of cold ISOSS sources

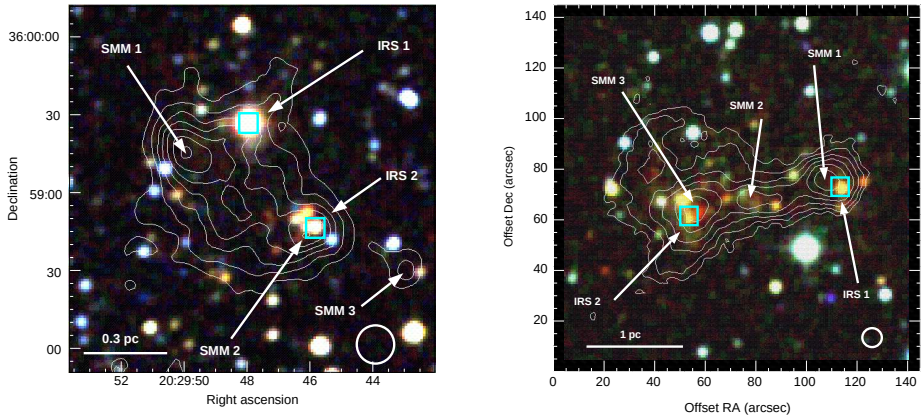

Fig 1: 850 μm and 450 μm continuum maps of the two ISOSS sources 20298+3559 (left) and 04225 (right), overlaid onto a JHK near-infrared composite from 2MASS. While the 1.5 arcmin ISOPHOT beam provided an integral flux measurement, our SCUBA observation resolve compact dust condensations (SMM1, SMM2 and SMM3) surrounded by extended envelopes. Young stellar objects detected by the MSX-satellite are marked (IRS1 and IRS2). The ellipse indicates the position of a very cold (T_{dust} = 11 K) cloud core in ISOSS20298+3559.

Ground-based 450 μm, 850 μm and 1.2mm continuum observations with high spatial resolution have been obtained with the SCUBA bolometer array at the JCMT on Mauna Kea, Hawaii, and MAMBO at the IRAM 30m telescope on Pico Veleta, Spain (Fig. 1). The IRAS and ISOPHOT data near the peak of thermal dust emission in combination with the proper sampling of the Rayleigh-Jeans part from the SCUBA/MAMBO observations allow a precise color temperature determination of the involved dust components (Fig. 2). In order to compare the physical conditions derived from our dust continuum, ammonia molecular line measurements reflecting the gas phase ISM have been performed at the 100m telescope in Effelsberg. For the characterization of the photosphere

and circumstellar environment of the embedded young stellar objects, we have performed spectroscopy with the TWIN spectrograph at the 3.5m telescope on Calar Alto in combination with diffraction-limited mid-infrared imaging using MAX at UKIRT on Mauna Kea. Fig. 3 presents our dereddened energy distribution for the source ISOSS20298+3559-IRS1.

3. ISOSS20298+3559 – A young star forming region

Our follow-up observations confirmed the presence of cold and massive molecular cloud cores. The peak column densities, average dust temperatures and total masses of the central regions of the two sources presented in Fig. 1 are $n(H_2) = 2 \cdot 10^{22} cm^{-2}, T_{dust} = 16K$ and $M = 120 M_\odot$ for ISOSS20298+3559 and $n(H_2) = 3 \cdot 10^{23} cm^{-2}, T_{dust} = 17K$ and $M = 4700 M_\odot$ for ISOSS04186. ISOSS20298+3559 is associated with an optical dark cloud complex in the Cygnus X giant molecular cloud (Krause et al. 2002). Several very young embedded objects have been detected, the most luminous one is the Herbig B2e star IRS1 ($M_\star = 6.5 M_\odot$) with a luminosity of 2200 $L_\odot$ and an age of less than 40000 years as derived from evolutionary tracks. SMM1 and SMM3 are two candidate Class 0 objects of intermediate mass. The externally heated cloud core with a mass of 50 $M_\odot$ is gravitationally bound and a good candidate for a massive pre-protostellar core. A star formation efficiency of 14 % was determined for the region.

4. Outlook

Follow-up observations showed evidence for the low age of star forming regions with red FIR colors ($S_{170\mu m}/S_{100\mu m} > 2$) detected by the ISOPHOT Serendipity Survey. All objects so far have been selected to contain near- and mid-infrared sources being signposts for ongoing clustered star formation. We plan to extend our sample of cold ISOSS sources without evidence for stellar counterparts but only coinciding with molecular clumps detected by carbon-monoxide ^{12}CO, ^{13}CO and CS line surveys. These objects are expected to be further candidates for studies of the earliest stages of massive star formation.

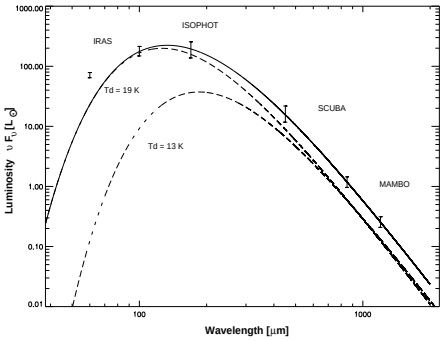

Fig. 2: Spectral energy distribution of ISOSS20298+3559. The total flux density is well described by optically thin thermal radiation of two single temperature modified blackbodies ($\epsilon \propto \lambda^{-2}$) corresponding to the cold cloud core and the warmer envelope with dust temperatures of $T_{dust} = 13 \pm 2K$ and $T_{dust} = 19 \pm 2K$ respectively.

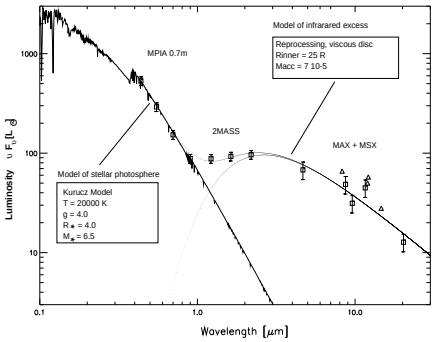

Fig. 3: Dereddened spectral energy distribution of the Herbig B2 star ISOSS20298+3559-IRS1. Our model of the system consists of the stellar photosphere (Kurucz model with $T_{eff} = 20000$ K, log g = 4) and an optically thick, viscous accretion disc, in agreement with the observations obtained with the MPIA 0.7m telescope and MAX at UKIRT.

Acknowledgements

The ISOPHOT Data Centre at MPIA is supported by Deutsches Zentrum für Luft- und Raumfahrt e.V. (DLR) with funds of Bundesministerium für Bildung und Forschung, grant No. 50QI0201. OK thanks the Wernher von Braun-Stiftung zur Förderung der Weltraumwissenschaften e.V. for financial support.

References

Bogun, S., Lemke, D., Klaas, U., et al., 1996, A&A 315, L71

Evans, N.J. II, Shirley, Y.L., et al., 2002, Proc. "Hot Star Workshop III: The earliest phases of massive star birth", ed. P.A. Crowther, ASP Conference Series, in press

Krause, O., Lemke, D., Vavrek, R., et al., 2002, Proc. "Galactic star formation across the stellar mass spectrum", ed. J. De Buizer & van der Bliek, ASP Conference Series, Vol. 287, p.174

Lemke, D., Klaas, U., Abolins, J., et al., 1996, A&A 315, L64

Cold Clouds in Cepheus Flare - Methods and Preliminary Results

Z. Kiss[1], L.V. Tóth[1,2]

[1]Astronomy Department, Eötvös Loránd University
H-1518 Budapest, P.O.Box 32., Hungary
[2]Max-Planck-Institut für Astronomie
Königstuhl 17, D-69117, Heidelberg, Germany
E-mail: Z.Kiss@astro.elte.hu, L.V.Toth@astro.elte.hu

Abstract

We study the physical parameters of the interstellar medium in the Cepheus Flare Region. We investigated the large scale dust temperature and density distribution based on COBE DIRBE, IRAS and ISOSS data. We give optical B band extinction maps of 26 subregions covering ≈ 25 square degrees. We found several opaque spots on the extinction maps, examined their optical, infrared and radio properties. We selected the suspected pre-protostellar clouds in order to perform further detailed studies in the near future. Many of dense clouds we found have very low DIRBE temperature ($T < 15\,K$) and former ^{13}CO and NH_3 detection. The majority of the objects seem to be starless, one third of them show ongoing star formation.

1. Introduction

We intend to gather and analyse multiwavelength data on nearby low mass star forming regions focusing on the phases when no embedded stellar object is seen. Low mass star formation is expected in low and moderate mass (from ten to few hundred solar masses) clouds, in dense ($n(H_2) > 10^3\,cm^{-3}$) and cold ($T \approx 10\,K$) cores. These dense cold cloud cores are optically thick for the visible light and can be identified as obscuring spots on optical images in case of nearby ones. On the other hand they are optically thin for their own quasithermal emission, which has a spectral maximum in the far infrared between 100 and $200\mu m$ wavelength. This FIR radiation can efficiently cool the clouds and also helps us to reveal these clouds. In this paper we use the optical extinction and FIR emission data to explore the clouds of the Cepheus Flare.

2. Data processing

We used the Lynds Catalogue of Dark Nebulae (Lynds, 1962) to select the most interesting subregions of the Cepheus Flare, catalogued earlier as dense regions from optical data. The high resolution parts of our studies were made on these subregions. We computed the DIRBE FIR colour temperature and optical depth map of the whole region, defined opaque objects based on extinction maps of subregions and gave the DIRBE temperature at the position of object defined. The high resolution IRAS (HIRES) maps were made for all subregions. We examined the FIR properties of clouds and the relations between FIR and optical features.

2.1. Optical data

To draw extinction maps in the region we considered 26 selected subregions having dark optical clouds of LDN catalog. The fields of these subregions are 1x1 degree sized. Extinction maps were computed via performing star counts (Dickman, 1978) on a $3'$ grid up to 18 mag using the USNO A2.0 catalog data.

Reference counts for unobscured fields were obtained from the galaxy model by Wainscoat et al. (1992) using a FORTRAN programme written by L. Balázs. The actual value of extinction in magnitudes can be obtained according to the following formula:

$$A = \frac{1}{b} log \left(\frac{N_{ref}}{N} \right) \quad (1)$$

where N is the actual count, N_{ref} is the modelled reference count and b is the slope of the modelled $logN(m)$ function. We defined the clouds as ellipses surrounding the 2 mag contours. We estimated cloud masses by the formula given by Dickman:

$$M = (\alpha_c d)^2 (N_{\mathrm{H}_2}/A_V) \mu \sum_i A_V^i \quad (2)$$

where α is the size of a grid cell in radians, d is the distance to the cloud, (N_{H_2}/A_V) is the considered ratio of H_2 column density and the visual extinction, μ is the average mass of particles in the cloud and A_V is the actual visual extinction. Distance data were taken form Hilton & Lahulla (1995).

2.2. Infrared data

For infrared studies we used the data of COBE DIRBE at 60, 100, 140 and 240 μm, IRAS (HIRES) at 60 and 100 μm and ISOSS at 170 μm.

The COBE DIRBE maps having low (≈ 0.7 degree) resolution give the basis of IRAS data ($\approx 4'$ resolution) calibration at 60 and 100 μm as well as the dust temperature and optical depth determination at 100, 140 and 240 μm. The IRAS 60 and 100 μm data were used for further calibration to obtain the high resolution ($90''$) HIRES maps. The fields of high resolution maps are the same as the extinction map fields. The ISOSS data were calibrated by the DIRBE data interpolated to 170 μm. The interpolation, the temperature and the optical depth were computed assuming that the dust emission follows a modified Planck function with $\beta = 2$.

We computed 100 and 170 μm FIR colour excesses defined as $E_{100} = I_{100} - I_{60}/\theta_{60-100}$ and $E_{170} = I_{170} - I_{100}/\theta_{100-170}$ using the values of galactic cirrus $\theta_{60-100} = 0.21$ and $\theta_{100-170} = 0.28$. These quantities are related to the actual dust temperatures, which are typically in the 10–20 K range. High colour excess values are good tracers of cold matter mainly at the longer wavelengths. This way we obtained high resolution maps of temperature distribution of the subregions. We computed the the characteristic values of defined quantities for all of our dense objects.

2.3. Other data

We examined the presence of ^{13}CO clouds from the Nagoya survey (Yonekura et al., 1997), NH_3 detections (Benson & Myers, 1989), YSOs and Hα (Kun, 1998) emission stars within the boundaries of clouds defined above.

3. Results

Using the method described above we defined 61 dense objects in the region possessing extinction value greater than 2 mag. According to DIRBE data these objects are cooler than the 18 K cirrus emission; the coldest ones have temperatures below 15 K. The higher resolution FIR colour excess maps also show low temperatures for our objects. There are some warmer objects with known embedded heating sources, showing notably high extinction and molecular emission (e.g. LDN 1174, LDN 1251). We determined the mass of each cloud and found that they are in the range of ten to some hundred solar masses, which is expected for low mass star forming clouds. Two third (41) of the objects defined are apparently starless, half of them (21) are remarkably cold according to the colour excess maps. Some of them show molecular emission, these are the best candidates for early phase star forming clouds with no embedded point-like object.

4. Conclusions

We studied the multiwavelength features of dark clouds in the Cepheus Flare region. Our methods allowed us to distinguish between the clouds with ongoing star formation, staying at an early phase of prestellar collapse and non-star-forming cloudlets, considering optical and infrared data. We found a number of early phase star forming cloud candidates without any detectable embedded point-like object. However, there are areas in the region without any optically catalogued dense clouds, where the molecular emission in ^{13}CO or the high FIR excess suggest notably high density and low temperature. This inspires us to extend the study to the whole area of the region, in order to find a complete sample of these objects for detailed examination.

Acknowledgements

We would like to thank Lajos Balázs, Mária Kun and Péter Ábrahám for their useful help. This research has made use of USNOFS Image and Catalogue Archive operated by the United States Naval Observatory, Flagstaff Station (http://www.nofs.navy.mil/data/fchpix/). This work was funded by the OTKA, project no. T034998.

References

Benson, P.J., Myers, P.C., 1989, ApJS 71, 89
Dickman, R.L., 1978, AJ 83, 363
Hilton, J., Lahulla, J.F., 1995, A&AS 113, 325
Kun, M., 1998, ApJS 115, 59
Lynds, B.T., 1962, ApJS 7, 1
Wainscoat, R.J., Cohen, M., Volk, K., Walker, H.J., Schwartz, D.E., 1992, ApJS 83, 111
Yonekura, Y., Dobashi, K., Mizuno, A., Ogawa, H., Fukui, Y., 1997, ApJS 110, 21

Indication of Star Formation Trigger on Cold Clouds†

L.V. Tóth[1], S. Hotzel[1], O. Krause[1], D. Lemke[1], Cs. Kiss[2], A. Moór[2]

[1]Max-Planck-Institut für Astronomie
Königstuhl 17, D-69117 Heidelberg, Germany
E-mail: lvtoth@mpia-hd.mpg.de
[2]Konkoly Observatory of the Hungarian Academy of Sciences
H-1525 Budapest, P.O.Box 67., Hungary

Abstract

We investigated the role of trigger mechanisms in the low mass star formation process. Star bearing and pre-protostellar cloud cores were searched as very cold objects of the ISO Serendipity Survey. We compared the distribution of cold starless cores VCCs to the distribution of FIR loops found on IRAS images. The distribution of VCCs follows the large scale ISM density distribution described by the FIR loops. Assuming that the 30pc-200pc scale trigger effects are reflected in the loop/shell structures, this result suggest a link between these effects and the VCCs.
Keywords: *ISM: clouds – dust, extinction – ISM: molecules – Infrared: ISM: continuum – Surveys*

1. Introduction

Our galaxy forms stars on a low enough rate to allow the existence of 10% ISM in spite of the fact that high fraction of the ISM is stored in Jeans unstable clouds. As a solution for the Zuckerman-Evans (1974) paradox, all sorts of support mechanisms were introduced in the 70s. This led to the magnetic field regulated star formation theory. Numerical simulations late last century showed that magnetic braking is not an important support for interstellar cloud cores. Recent observational and modelling evidence suggests that actually there is no need for support since the clouds indeed collapse almost on free-fall time scale. This lowers the importance of star formation trigger mechanisms. Ten years ago those were still thought to be responsible for setting the location and/or timing and/or efficiency of star formation.

†Based on observations with ISO, an ESA project with instruments funded by ESA Member States (especially the PI countries: France, Germany, the Netherlands and the United Kingdom) and with the participation of ISAS and NASA.

One of the major unknown factors in theories of star formation is a detailed observational determination of the initial conditions of the collapse phase that forms a protostar. The pre-protostellar (or prestellar for short) core phase (Ward-Thompson et al. 1994) is believed to be the stage of star formation that precedes the formation of a protostar and hence should represent observationally the initial conditions of protostellar collapse. Some recent observations have even indicated that the Initial Mass Function (IMF) of stars may be determined before the protostellar collapse phase (see eg. Motte et al. 2001). It is thus important to know whether trigger plays an important role in the early (collapse) phase of cloud core evolution, prior to star formation.

Tracing trigger in the galactic ISM we use large FIR structures seen widely on IRAS FIR images. We compiled the first catalogue of FIR Loops which will be briefly discussed here. It is important to check the distribution of gravitationally bound starless cloud cores i.e. pre-protostellar cores whether it follows the large scale ISM density distribution. One has to collect a statistical sample of cloud cores well sampling both the on-loop and off-loop class. We then compare the physical parameters of both classes. Comparing the numbers in the two classes already allows us to draw a statement on the trigger effect of the process responsible for the creation of the loops. We evaluate the ISO Serendipity Survey (ISOSS) data which cover 15% of the sky with serendipitous slews observed at 170 μm with the ISOPHOT camera (Lemke et al. 1996) in board of ISO. We will discuss the parameters of ISOSS cores and their relation to the FIR loops.

2. What we know on low mass star formation

2.1. Tracers and efficiency

We outline important aspects of low mass star formation research, and give observational examples. First of all we list the most common indicators of recent low mass star formation. Various observational and theoretical results on the efficiency of star formation are also given below. Our selection of examples of low mass star formation is biased towards cases where trigger is apparent or expected. The trigger is considered strong when the star formation efficiency is increased.

Tracers of (low mass) star formation:

- Hα emission line stars. Star formation in the L134 complex: few$\times 10^6$ years old Hα stars around L1780, whose formation may be triggered by winds from the Sco-Cen-Lup association (Martin & Kun 1996).

- IRAS point sources as YSOs. Selection criteria were given by eg. Emerson (1987), statistical study of the "whole" IRAS Point Source Catalog was carried out by Prusti et al. (1992). Apparently the YSO distribution is not random.
- NIR point sources with $> 3\%$ NIR excess (Lada 1992)
- bipolar molecular outflows (Bally, 1982, Sato & Fukui 1989)
- cold molecular cloud cores as NH_3 (1,1) density peaks. The most cited NH_3 survey for dense cores in dark clouds (Benson & Myers 1989) indicates a physical association of young type IRAS sources and $T_{kin} \approx 10\,\mathrm{K}$ cold, and $n(\mathrm{H_2}) > 10^4 \mathrm{cm}^{-3}$ dense cloud cores.
- very cold, $T_d \approx 10\,\mathrm{K}$ dust, found in cloud cores eg. in B35 by Lada et al. (1981) and in L1172 by Ladd et al. (1991).

Regulation of star formation - theory: Most of the molecular clouds in the Galaxy are Jeans' unstable, which results in a star-formation rate of $130 < SFE < 400\,\mathrm{M_\odot yr}^{-1}$ (see, e.g., Evans 1991). But this number is two orders of magnitude higher than the average Galactic star-formation rate over the last few Gyr (see, e.g., Scalo 1986). It was generally believed that magnetic fields play a crucial role in supporting the clouds (Mouschovias & Spitzer 1976; Nakano & Nakamura, 1978). A magnetized cloud is virial stable when $M_v > 10^3 \mathrm{M_\odot}$. As it has recently been claimed, magnetic brake (e.g. ambipolar diffusion) cannot prevent local collapse for much longer than the global free-fall time (Heitsch et al., 2001). Does turbulence control the star formation? Is there a still larger scale trigger? Radiation driven implosion (RDI) shapes the clouds: gas condensations in molecular clouds irradiated by an O star and the cloud will have a cometary shape after re-expansion in $\approx 10^6$years (recently e.g. Kessel-Deynet & Burkert, 2002).

Increased efficiency of star formation - observations: The star formation efficiency (SFE) seems to vary with time and location. Large variations of SFE were observed in L1630 where all the massive cores contain regions with densities of at least $10^5\,\mathrm{cm}^{-3}$. The cores with rich embedded clusters (with high SFE), tend to be larger (i.e. to have larger areas of detectable CS($J = 5 \rightarrow 4$) emission) than those without clusters and with low SFE (Lada et al., 1997). It is strange, however, that in the Rosette molecular cloud a majority (65%) of the high-mass ^{13}CO clumps ($M > 450\,\mathrm{M_\odot}$) are not associated with any embedded cluster. The cluster formation may be triggered by the ionization fronts from the nearby HII region associated with NGC 2244 (Phelps & Lada, 1997). The distribution of

YSOs or embedded like IRAS point sources of the Upper Cep-Cas follows a large loop shell (Pásztor et al., 1993) YSOs in L1251 indicate 5% SFE and an age gradient (Kun & Prusti 1993). A shock travelled through L1251 according to Tóth & Walmsley (1996). A few times 10^6 years old Hα stars around L1780 are related to a slowly expanding old SNR shell (Tóth et al., 1995; Martin & Kun, 1996). Cometary clouds RNO 6 and RNO 6NW with embedded IR point sources are cases of formation of intermediate mass stars triggered by RDI according to Bachiller et al. (2002). Star formation propagates with a speed of $1\,\mathrm{kms}^{-1}$, as it can be inferred from the average separation and age difference of aligned cores in the Eagle nebula. Cloud P contains "core b", "core a", and the NIR source P1, with an average projected separation of < 0.1 pc. These objects most likely correspond to a starless core, a Class 0 object, and a Class I object, respec-tively. The age difference is then roughly 10^5 yr. The apparent propagation speed is a little slower than the shock propagation speed of $1.3\,\mathrm{kms}^{-1}$ (White et al., 1999). Conclusion: O5 star is triggering star formation in Cloud P.

2.2. Cold interstellar matter

Star formation occurs in dense cores within molecular clouds (e.g. Williams et al., 2000), although study of such regions was hampered for many years by their very large optical depths at near-infrared and optical wavelengths. It is only since the opening up of the far-infrared and submillimetre regimes that astronomers have been able to study molecular clouds in detail. Density enhancements of the interstellar medium far enough from heat sources and sources of moment can cool efficiently, which leads to collapse. Detailed study of the cold and very cold phase ISM and many pre-stellar cores is central to our understanding of star formation.

Cold interstellar matter (CISM) was introduced in the three phase ISM model of McKee & Ostriker (1977) with density and temperature of $n(\mathrm{H}) = 42\mathrm{cm}^{-3}$ and $T_{kin} \leq 80$K and with a volume filling factor of $\approx 2\%$. The CISM as appears in FIR, is mostly cirrus. At high galactic latitudes it has a temperature of $T_d = 17.5$K (Dwek et al., 1997; Lagache et al., 1998). The ISM gets very cold at shielded regions, efficiently cooled by FIR and mm-lines. It forms molecular clouds ($T_{kin} = 20$K), and starless cloud cores ($T_{kin} = 10$K). The dust is also cold in these clouds and cloud cores. Thus they may be located by excess of FIR relative to 60μm surface brightness. The dust temperature in the very cold ISM is $T_d \leq 15$K (Laureijs et al., 1991; Boulanger et al., 1998; Lagache et al., 1998). An example of FIR radiation of CISM in other galactic disks is given by Haas et al. (1998).

The dust radiation models account for FIR-NIR-optical-UV radiation (e.g. Desert et al., 1990). They assume three components: PAHs and VSGs ($a <$ 10nm, $\lambda \leq 60\mu$m) and large grains (inferred from optical). As simulations show, the heating-cooling instabilities in clouds may lead to collapse (Clarke & Pringle, 1997; Burkert & Lin, 2000). The very cold cloud cores are thought to be the results of such instabilities, and were found to be related to star formation.

IRAS Loops in the 2nd Galactic Quadrant: In order to study the role of trigger in star formation we have carried out a search for interstellar bubble tracers i.e. loops. To achieve a high angular resolution we analysed IRAS maps instead of eg. HI surveys. Due to its low opacity the $100\,\mu$ radiation of dust is useful in a search for both diffuse and dense ISM. All IRAS ISSA maps of the 2nd galactic quadrant were searched for arc-shape bright regions. Our eye-biased search resulted over 150 loops (loop is a $> 60\%$ complete ring with significant surface brightness excess over its surroundings). These FIR loops bear point sources of all types. At intermediate galactic latitudes, the surface density of the TTau-like IRAS point sources is two times higher on the loops than elsewhere whereas the ISM column density is only 50% higher towards the loops than elsewhere (see Kiss et al. 2002).

3. ISO observations and data analysis

ISOSS: The coldest cloud cores are believed to be in the phase of thermal instability induced collapse, and will eventually form low mass stars. The most relevant recent survey to find these objects is the ISO Serendipity Survey (Bogun et al., 1996; Stickel et al., 1998; Tóth et al., 2000). Below we summarize what we have to know on ISOSS and the ISOSS very cold cores (VCCs).
ISOSS - the measurement: Slews between pointed observations of ISO were used to scan the sky with ISOPHOT's C200 array in a broad wavelength band centred at $170\,\mu$m. The slew paths are unpredictable and curved in order to avoid the forbidden regions near Sun and Earth.
ISOSS Calibration Accuracies (errorbars): Photometric accuracy of 30% can be achieved (Müller et al., 2002). Pointing $rms < 1'$, rms reproducibility error is $< 15\%$ as measured at scan crossings (Stickel et al., 2000).

ISOSS very cold cores (VCC): Besides the ISOSS extragalactic point source catalogue (Stickel et al. 1998) the galactic FIR objects were also studied resulting a number of candidate pre-protostellar cores. Very cold (< 15K),

fairly bright (> 6Jy) ISOSS/IRAS sources were located. Their optical associates on DSS2 are mostly opaque cloud cores in cloud complexes or in isolated dark clouds. There are associated NIR point sources seen usually around, but not "inside". As mm spectroscopy followups (CO, CS, NH_3 lines with Effelsberg-100m, Parkes-64m, IRAM-30m telescopes) revealed, these cold ISOSS sources are associated with dense parts of molecular clouds. In Chamaeleon (Tóth et al., 2000), the $I(170)$-excess clouds have $T_{\rm col}$(dust) $< 14\,$K with a 3% area filling factor. The $I(170)$ and $I(100)_{\rm cold}$ FIR surface brightnesses are well correlated, and $I(170)$ is correlated up to $A_V = 7\,$mag with the NIR based extinction. The very cold ISOSS sources were found to be cloud cores and thus were named as very cold cloud cores (VCCs). There are 14 VCCs with $T_d \approx$ 12K in the Cepheus region. these VCCs are inside $A_{\rm V} > 3\,$mag dark clouds, and mostly associated with $T_{kin} \approx 10\,$K NH_3 cores.

4. Relating very cold cores to FIR loops

The distribution of VCCs, which are candidate pre-protostellar cores, is compared to the distribution of FIR loops (Kiss et al. 2002). The FIR loops are most likely projections of 3D bubble shells, as shown by a statistical investigation of the apparent shapes. These are the most prominent features of the nearby (2kpc) interstellar medium on 30–200 pc scales. Thus these shells are considered to be proper tracers of large scale trigger effects. The investigation is limited to the 2^{nd} galactic quadrant which is, however, the region with best sky coverage fraction in the ISOSS database. The resuls of the comparison are:

- 89 VCCs are inside the 2nd Galactic Quadrant
- the VCCs appear within $-40° < b < 30°$ (limited b range)
- the FIR loop shells cover 32% of total sky area within $-40° < b < 30°$
- 70 of the 89 VCCs (79%) are associated with loops, 34 are on loops
- only 6 VCCs are seen inside a loop and 2 VCCs are far from loops

We conclude that the formation of the ISOSS VCCs is likely triggered by the same physical processes which formed the large shells seen as FIR loops. Is it a weak trigger only i.e. modifying the location of otherwhise spontaneous star formation by moving the ISM into shells, or may the high pressure events directly trigger cloud collapses? Further investigation of individual VCCs may answer to this question.

Acknowledgements

We acknowledge the valuable comments by Prof. Kalevi Mattila. The ISOPHOT project and Postoperation Phase was funded by the Deutsche Agentur für Raumfahrtangelegenheiten (DARA, now DLR), the Max-Planck-Gesellschaft, the Danish, British and Spanish Space Agencies and several European and American institutes. Members of the Consortium on the ISOPHOT Serendipity Survey (CISS) are MPIA Heidelberg, ESA ISO SOC Villafranca, AIP Potsdam, IPAC Pasadena, Imperial College, London.
This research was partly supported by the OTKA F-022566 grant and by the Academy of Finland through grants No. 158300 and 173727 and received HAS-JSPS support of Hungarian-Japanese exchange.
This research has made use of the Digitized Sky Survey, produced at the Space Telescope Science Institute, NASA's Astrophysics Data System Abstract Service, the Simbad Database, operated at CDS, Strasbourg, France.

References

Bachiller, R., Fuente, A., Kumar, M.S.N., 2002, A&A 381. 168
Bally, J., 1982, ApJ 261, 558
Benson, P.J. & Myers, P.C., 1989, ApJS, 71, 89.
Bogun, S., Lemke, D., Klaas, U., et al., 1996, A&A 315, L71
Burkert, A., Lin, D.N.C., 2000, ApJ, 537, 270
Clarke, C.J. & Pringle, J.E., 1997, MNRAS 288, 674
Desert, F.-X., Boulanger, F., Puget, J.-L., 1990, A&A 237, 215
Dwek, E., Arendt, R.G., Fixsen, D.J., et al., 1997, ApJ 475, 565
Emerson, J.P., 1987, "IRAS and star formation in dark clouds", in: Star forming regions, IAUS 115, p.19
Evans, N.J.II., 1991, ASP Conf.Ser., 20, 45
Heitsch, F., MacLow, M.M., Klessen, R.S., 2001, ApJ 547, 280
Foster, P.N.; Chevalier, R.A., 1993, ApJ 416 303.
Haas, M., Lemke, D., Stickel, M., et al., 1998, A&A 338, 33
Harjunpää, P., Liljeström, T., Mattila, K., 1991, A&A 249, 493.
Henriksen, R., André, P., Bontemps, S., 1997, A&A 323, 549.
Hotzel, S., 2001, PhD Thesis, Heidelberg.
Hotzel, S., Harju, J., Juvela, D., et al., 2002, A&A 391, 275
Kessel-Deynet, O. & Burkert, A., 2002, RMxAC 12, 25
Kiss, Cs., Moór, A., Tóth, L.V.: Catalogue of IRAS Loops in the 2nd Galactic Quardant, URL:*http://astro.elte.hu/IRASLoops/IRASLoops.html*
Kun M., 1998, ApJS 115, 59
Kun, M. & Prusti, T. 1993 A&A 272. 235

Lada, C.J., Thronson, H.A.Jr., Smith, H.A., et al., 1981, ApJ 251, 91
Ladd, E.F., Adams, F.C., Fuller, G.A., et al., 1991, ApJ, 382, 569
Lada, E.A., 1992, ApJ 393, 25
Lada E.A., Evans, N.J. II, Falgarone, E., 1997 ApJ 488, 286
Lagache et al. 1998, A&A 333, 709
Laureijs, R. J.; Clark, F. O.; Prusti, T., 1991, ApJ 372, 185
Lemke D., Klaas U., Abolins J., et al., 1996, A&A 315, L64
Lynds, B.T., 1962, ApJS, 7, 1.
Martin, E.L. & Kun, M., 1996, A&AS 116. 467
McKee, C.F. & Ostriker, J.P., 1977, ApJ 218, 148
Motte, F. André, P., Ward-Thompson, D., Bontemps, S., 2001, A&A 372, L41
Mouschovias, T.C., & Spitzer, L., 1976, ApJ, 210, 326.
Müller, T.G., Hotzel, S., Stickel, M, 2002 A&A 389, 665
Nakano, T., & Nakamura, T., 1978, PASJ 30, 681
Pásztor, L., Toth, L.V., Balazs, L.G., 1993, A&A 268, 108
Phelps, R.L.& Lada, E.A., 1997 477, 176
Prusti, T., Adorf, H.-M., Meurs, E.J.A., 1992 A&A 261, 685
Reach, W.T., Dwek, E., Fixsen, D.J., et al., 1995, ApJ 451, 188
Sato, F. & Fukui, J. 1989, ApJ
Scalo, J.M., 1986 FCPh 11, 1
Stickel, M., Bogun, S., Lemke, D., et al., 1998, A&A, 336, 116.
Stickel, M., Lemke, D., Klaas U., et al., 2000, A&A 359, 865
Tóth, L.V., Walmsley, C.M., 1996 A&A 311, 981
Tóth, L.V., Hotzel, S., Krause, O., et al., 2000, A&A, 364, 769
Ward-Thompson, D., Scott, P.F., Hills, R.E., Andre, P., 1994, MNRAS 268, 276.
Ward-Thompson, D., André, P., Kirk, J.M., 2002, MNRAS 329, 257
Wheelock, S.L., Gautier, T.N., Chillemi, J., et al., 1994, IRAS sky survey atlas: Explanatory supplement. JPL Publication 94-11, IPAC, JPL
White, G.J., Nelson, R.P., Holland, W.S., et al., 1999, A&A 342, 233
Whitworth, A., Summers, D., 1985, MNRAS 214, 1.
Whitworth, A.P., Ward-Thompson, D., 2001, ApJ 547, 317.
Williams, J.P., Blitz, L., McKee, C.F., 1999, Protostars and Planets IV, 97.
Yonekura, Y., Dobashi, K., Mizuno, A., et al., 1997, ApJS 110, 21.

PDRs in Star Forming Regions

M.E. Lebrón[1], L.F. Rodríguez[2], S. Lizano[2]

[1]Max Planck Institut für Radioastronomie
Auf den Hügel 69, D-53121, Bonn, Germany
[2]Universidad Nacional Autónoma de México - Unidad Morelia
Apdo. Postal 3-72, Morelia, Michoacán, México
E-mail:[1]mlebron@mpifr-bonn.mpg.de

Abstract

The molecular gas can be photodissociated if it is exposed to intense far-ultraviolet (FUV) radiation. Intermediate and high mass stars generate enough flux in the FUV range to produce a significant photodissociation region (PDR) around them. In order to characterize the PDR that forms near these regions high resolution infrared and centimeter wavelength observations are required. Current centimeter-wave telescopes/interferometers offer the required spatial resolution to detect and to study in detail the PDRs in star forming regions. We present a short review of observations of PDRs and discuss the particular case of G111.61+0.37.

KEYWORDS: *ISM: HII regions, clouds – Radio lines: ISM – ISM: Individual objects: G111.61+0.37*

1. Introduction

Young massive stars not only form HII regions but also create significant photodissociated regions and the radiation field excites various transitions in the surrounding molecular material. In the last 25 years many theoretical works were done on PDRs (e.g. Hill & Hollenbach, 1978; Roger & Dewdney, 1992; Bertoldi & Draine, 1996; Hollenbach & Tielens, 1997; Díaz-Miller et al., 1998; Gorti and Hollenbach, 2002). PDRs of young massive stars are simply the intermediate region between the HII region and the quiescent molecular gas. For better illustrate the PDRs produced by young massive stars a simple diagram is shown in Fig. 1. The ionizing photons form an HII region close to the star, while the photodissociating photons penetrate more into the cloud generating, first, a zone where the hydrogen is neutral (HI zone), and then a molecular excited zone. The carbon is ionized deeper than the HI zone into the cloud. The PDR ends when all the oxygen is contained in O_2 and CO molecules (for details about PDRs see the review of Hollenbach & Tielens, 1997).

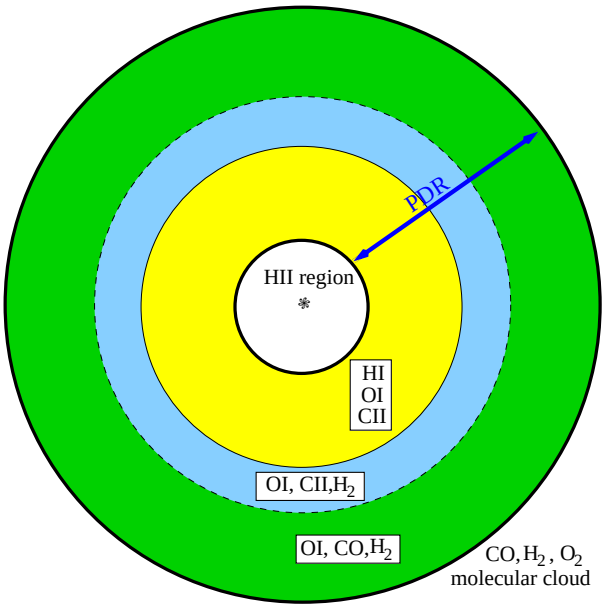

Figure 1: Diagram of a photodissociated region formed around a young massive star that also forms an HII region. The PDR starts with the HI zone where the hydrogen is in neutral phase, carbon is ionized and oxygen neutral. The zone of ionized carbon (CII) extends deeper into the cloud where the hydrogen is already molecular but the oxygen is still neutral. The last zone corresponds to the neutral oxygen (OI), that goes even deeper into the cloud, where the carbon is already contained in CO molecules. The PDR ends when all the oxygen is contained in O_2 and CO molecules.

The main coolants of the PDRs are [CII] 158 μm, [OI] 63 μm lines, CO rotational lines, flourescent H_2 lines, dust continuum emission and PAH features. The FIR and millimetric emission of PDRs are used to determine their physical parameters (e.g. Liu et al., 2001; Vastel et al., 2001). Because of the low angular resolution of FIR telescopes ($\sim$1 arcmin), it is not possible to study in detail the kinematic and the spatial distribution of PDR in compact sources (e.g. star-forming regions). Although the main coolants are in the IR band, PDRs also emit in the cm wavelength range.

The radio emission of PDRs is detected in the 21 cm HI line, and also in carbon recombination lines (e.g. Wyrowski et al., 1997; Lebrón & Rodríguez, 1997; Gómez et al., 1998; Wyrowski et al., 2000). The lines at cm wavelengths are weaker than the IR lines, but with the high spatial and spectral resolution that can be achieved with radio telescopes/interferometers, the observation of radio lines are a valuable tool for studying the kinematics of PDRs in compact sources. An example of a detailed study of the neutral region of the PDR in a star-forming region was done in G111.61+0.37 (Lebrón et al., 2001). The compact HII region G111.61+0.37 was studied in the HI 21cm line (that traces the neutral region of the PDR), ammonia transitions (1,1) and (2,2) (that trace

the dense molecular gas) and the recombination line H92α (that traces the HII region) with the VLA interferometer.

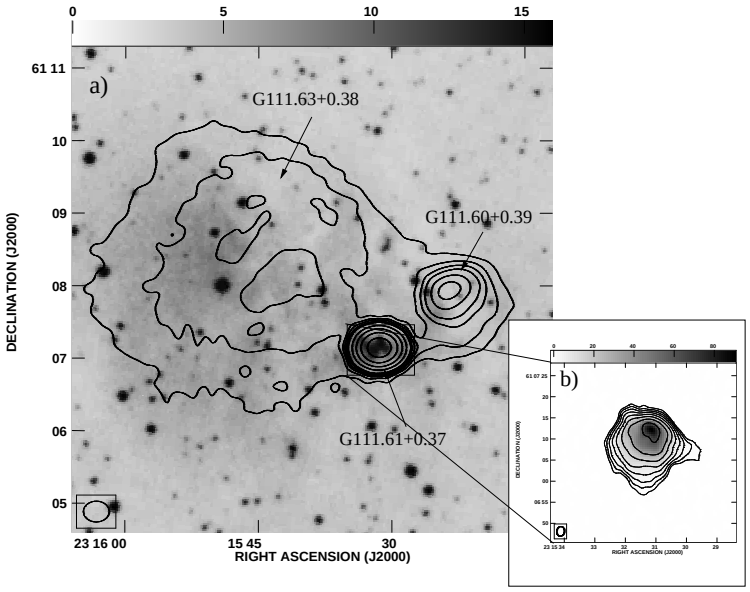

Figure 2: (**a**) 1.4 GHz continuum emission in Sharpless 159 (contours). G111.61+0.37 is located in the center of the map. The background image is the red POSS plate of the region. (**b**) 3.6 cm continuum emission of G111.61+0.37. The continuum emission shows a cometary shape distribution.

2. The PDR in G111.61+0.37

G111.61+0.37 (hereafter called G111.61) is a compact HII region in the Sharpless 159 region at a distance of 3.1 kpc (Brand & Blitz, 1993). Fig. 2a shows a continuum map at 1.4 GHz (contours) of the Sharpless 159 region. G111.61 is the brightest source in the region and is associated with the IR source IRAS 23133+6050. The cometary shape of the continuum emission in G111.61

(see Fig. 2b) is due to a champagne flow of the ionized gas (Lebrón et al., 2001; Kurtz et al., 1994).

The photodissociated region in G111.61 was detected in the 21cm line of HI. The HI spectra of G111.61 shows absorption and emission features (see Fig. 3), being the absorption ones the most prominent. Nevertheless, the emission feature is of our particular interest.

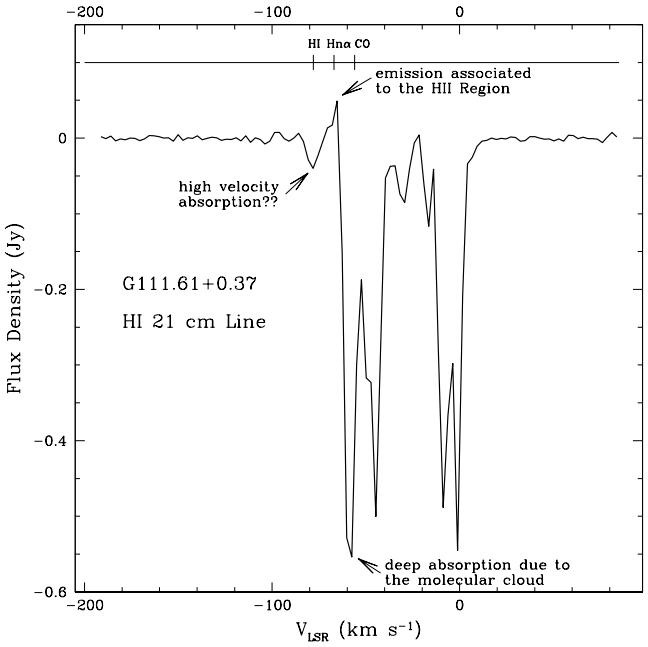

Figure 3: HI 21cm line spectrum of G111.61+0.37.

A contour map of the integrated HI emission between -58 and -67 km s^{-1} (emission feature) is shown in Fig. 4. The HI in emission (continuous line contours) is compact ($25'' = 0.4$ pc) and located next to G111.61. The HI in emission appears to the SE of G111.61. This asymmetry in the emission distribution is interpreted as a consequence of density gradients in the molecular gas. Sizes of PDRs have strong dependence on the density of the molecular gas (Díaz-Miller et al., 1998).

In the case of G111.61 we found dense molecular gas (density $> 10^6$ cm^{-3}), located to the NW of the HII region (see Fig. 5). This dense gas is confining the

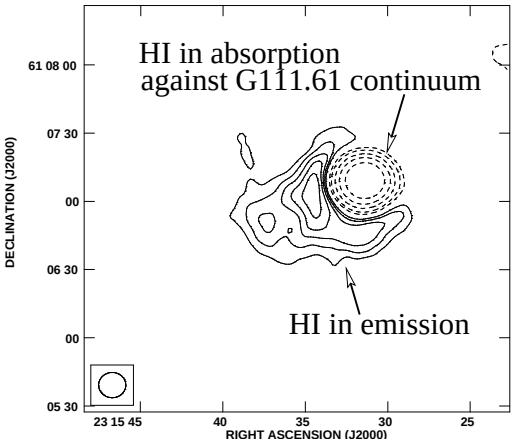

Figure 4: HI 21cm velocity-integrated map of G111.61+0.37. The line emission was integrated between -58.6 to -68.9 km s^{-1}. The continuous line contours show the HI in emission, while the dashed-line contours show the HI in absorption. The contour levels are -100, -50, -25, -12, -9, -6, -4, 4, 5, 6, 7, 8, and 9 $\times$ 1.1 mJy beam^{-1}.

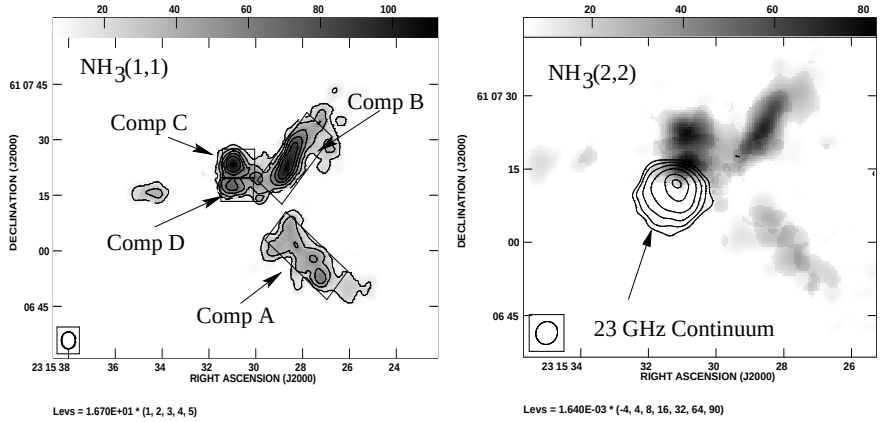

Figure 5: NH_3(1,1) and (2,2) velocity-integrated line maps (grey scale) and 23 GHz continuum map of G111.61+0.37 (contours on right panel). Component D is located near the HII region and is hotter than the other ammonia clumps. Clump D is confining the HII region and the PDR in the NW direction.

HII region in the NW direction (Lebrón et al., 2001). The expected size for a PDR that developes in a medium of density greater than 10^5 cm^{-3} is $<$0.03 pc

(Díaz-Miller et al., 1998). Such small structures could not be detected with the HI observations dicussed here. No PDR was detected between the HII region and the dense molecular gas (traced by ammonia), but a prominent HI zone extends into the low density molecular gas.

The HI emission observed in G111.61 is a clear example of the neutral region of a PDR in a massive star-forming region. The structure of the PDR is also shaped by the molecular environs like the HII region. The determined column density and mass of the HI emission are 5.9 $\times$ 10^{20} cm^{-2} and 0.8 $M_{\odot}$, respectively (a T_{ex} of 300 K was assumed).

3. Conclusions

In this paper we presented the results of the HI 21 cm line observations of the star-forming region G111.61+0.37. The neutral zone of the PDR is bigger than the HII region. The spatial distribution of the HI emission also suggests a density gradient in the molecular gas. This result is confirmed by ammonia observations. The spatial resolution that can be obtained in the cm wavelength range permits the study the PDRs in compact sources.

References

Bertoldi, F., & Draine, B. 1996, ApJ, 458, 222
Brand, J., & Blitz, L. 1993, A&A, 275, 67
Díaz-Miller, R.I., Franco, J., Shore, S.N., 1998, ApJ, 501, 192
Gómez, Y., Lebrón, M., Rodríguez, L.F., Garay, G., Lizano, S., Escalante, V., Cantó, J., 1998, ApJ, 503, 297
Gorti, U, Hollenbach, D.J. 2002, ApJ, 573, 215
Hill, J. K., & Hollenbach, D.J. 1978, ApJ, 225, 390
Hollenbach, D.J., & Tielens, A.G.G.M., 1997, ARA&A, 35, 179
Kurtz, S., Churchwell, E., Wood, D.O.S., 1994, ApJS, 91, 659
Lebrón, M.E., & Rodríguez, L.F. 1997, Rev. Mexicana Astron. Astrofis., 33, 165
Lebrón, M.E., Rodríguez, L.F., Lizano, S. 2001, ApJ, 560, 806
Liu, X.-W., Barlow, M.J., Cohen, M., Danziger, I.J., Lou, S.-G., Baluleau, J.P., Cox, P., Emery, R.J., Lim, T., Peguignot, D. 2001, MNRAS, 323, 343
Roger, R.S., Dewdney, P.E., 1992, ApJ, 385, 536
Vastel, C., Spaan, M., Ceccarelli, C., Tielens, A.G.G.M., Caux, E. 2001, A&A, 376, 1064
Wyrowski, F., Schilke, P., Hofner, P., Walmsley, C.M., 1997, ApJ, 487, L171
Wyrowski, F., Walmsley, C.M., Goss, W.M., Tielens, A.G.G.M., 2000, ApJ, 543, 245

Reducing and Analyzing Chemical Networks

D. Semenov[1], D. Wiebe[2], Th. Henning[3]
[1]Astrophysical Institute and University Observatory
Schillergäßchen 2-3, 07745 Jena, Germany
E-mail: dima@astro.uni-jena.de
[2]Institute of Astronomy of the RAS
Pyatnitskaya St. 48, 109017 Moscow, Russia
[3]Max Planck Institute for Astronomy
Königstuhl 17, 69117 Heidelberg, Germany

Abstract

A new efficient method allowing the reduction of the number of species and reactions in chemical networks is outlined. We applied it to the UMIST 95 astrochemical database in order to find a subset of species and reactions governing the evolution of carbon monoxide under conditions, typical of dense molecular clouds. We succeeded in isolation of such a tiny set for the pure gas-phase chemistry which gives the reliable estimation of the CO abundances under a wide range of the gas temperatures, densities, and visual extinctions. We showed that the reduction is only modest when gas-grain interactions and surface reactions are taken into account.
Keywords: *astrochemistry – stars: formation – molecular processes – ISM: molecules – ISM: abundances*

1. Introduction

Nowadays large progress is achieved in modelling of the chemical and dynamical evolution of various astrophysical environments, like protostellar cores or protoplanetary disks. Still the coupled self-consistent chemical and dynamical modelling of such objects is beyond the capabilities of modern computers. The main reason is that typical chemical networks used in astrophysical simulations contain hundreds of species involved in thousands of reactions. Their accurate handling together with hydrodynamical calculations requires enormous computational efforts.

However, in many cases only a few species are of the main interest for an astronomer. For instance, the most important species for the evolution of magnetized interstellar clouds are few dominant ions, as mainly their abundances regulate the ionization degree. Then it seems intuitively clear that one may neglect some of "exotic" species, like long carbon chains, in order to speed up the calculations and still have reasonable estimations on the degree of ionization.

Notwithstanding, the qualitative considerations of this kind require a rigorous mathematical analysis to be proven.

Ruffle et al. (2002) made a first attempt to apply such a method – objective technique developed in other scientific community – for the reduction of astrochemical networks. They were able to discriminate among about 200 species only 33 which are necessary to follow the evolution of CO abundances within accuracy of 30% at $t > 10^5$ years in static translucent regions. In the paper of Rae et al. (2002) the same reduction technique has been applied to identification of reduced networks governing the fractional ionization in molecular clouds under a wide range of physical circumstances. It has been found that one has to keep about thirty species from the entire set of more than two hundred species in order to predict the ionization degree without significant errors.

In this paper, we introduce a new reaction-based method of reduction which allows to reduce *simultaneously* the number of species and reactions in chemical networks. Using this reduction technique, we perform an analysis of the UMIST 95 database of chemical reactions in order to select species and reactions that are needed for accurate estimations of carbon monoxide abundances under conditions of dense molecular clouds. Our special aim is to investigate the possibility to reduce the chemical networks when complicated gas-grain interactions and dust surface reactions are taken into account beside the common gas-phase reactions.

2. Chemical Model

The detailed description of our chemical model is given in the paper of Wiebe et al. (2002). Here, we briefly summarize its main features.

We take into account gas-phase reactions, gas-grain interactions, and dust surface reactions. The species set and gas-phase reaction rates are taken from the UMIST 95 database (Millar et al. 1997). Dust surface reactions are adopted from Hasegawa et al. (1992). The desorption energies of the surface species are taken or estimated from Hasegawa & Herbst (1993). The gas-grain interactions include the following physical processes: accretion of neutral species onto dust grains, their desorption due to the thermal evaporation and cosmic ray heating, and dissociative recombination of ions on grain surfaces.

Two chemical networks are investigated, namely, the pure gas-phase network consists of electron, 12 atoms, 137 molecules, and 245 ions (in total 395 species) involved in 3864 gas-phase reactions and the gas-grain network having additional 148 surface species, 729 gas-grain and 192 dust surface reactions.

The probability of species to stick on the dust surfaces is assumed to be 0.3 for all ions and all neutral species except for H, He, and H_2. The sticking coefficient of the atomic hydrogen is estimated from the expression given in Hollenbach & McKee (1979), Equation (3.7). Sticking probabilities for helium and molecular hydrogen are assumed to be zero.

We consider the gas density $n_{\rm H} = 10^7$ cm^{-3} and fix gas and dust temperatures to 10 K. No photoprocessing by the interstellar UV radiation is assumed ($A_V \geq 10$). Dust grains are considered as silicate-like spheres having a uniform size 0.1 micron, density 3 g cm^{-3}, and 10^6 surface sites for adsorption. Dust is assumed to constitute 1% of the gas density by mass.

We use well-known "high metal" and "low metal" initial abundances (see, for instance, Lee et al. 1998). The "high metal" means standard solar composition with a modest depletion of 2 for S and stronger depletions of $\sim 10 - 100$ for Si and metal atoms. The "low metal" values contain additional depletion factors of 100 for each of these elements. The abundances of He, C, N, O, S, Si, Na, Mg, and Fe are taken from Aikawa et al. (1996). For P and Cl we take the values from Grevesse & Sauval (1998) and use the same depletion factors as for Fe. We suppose that only these atomic neutral species and molecular hydrogen are present at initial time $t = 0$.

3. Reaction-based Reduction Technique

The new method of reaction-based reduction allows us to select from the entire network only those species and reactions that are *necessary* to compute abundances of chosen (*important*) species with a reasonable accuracy.

The basic idea of this reduction technique is to search for the production and destruction reactions, critical for the evolution of the important species, and determine their relative importance. It can be done by the analysis of the sensitivity of the net formation (or loss) rate of given species in respect to the presence of particular reactions at a certain time.

Below we briefly outline the algorithm of our reduction approach.

First, one runs the chemical model with the full network for certain physical conditions in order to obtain abundances of all species in the network during the entire evolutionary time.

Then, important species for which reduction will be made, are specified. The algorithm estimates weights of all species $w_{\rm s}$ and reactions $w_{\rm r}$ in order to quantify their significance for the evolution of the important species at a particular time moment by the following iterative process:

1. During the first iteration, weights of important species are set to 1 and weights of all other species and all reactions are set to 0;

2. For the iteration i and the current species s_i all relevant formation and destruction reactions are found and their weights $w_{\rm r}^i$ are specified as

$$w_{\rm r}^i(j) = \max\{w_{\rm r}^{i-1}(j),\ \frac{k_j n_{r_1}(j) n_{r_2}(j)}{\sum\limits_{l=1,N_{\rm r}(i)} k_l n_{r_1}(l) n_{r_2}(l)} w_{\rm s}(i)\} \qquad (1)$$

   Here k_j is the rate of jth reaction, $n_{r_1}(j)$ and $n_{r_2}(j)$ are the abundances of the first $r_1(j)$ and second $r_2(j)$ reactants in the jth reaction, respectively, $N_{\rm r}(i)$ is the amount of the reactions having s_i as a reactant or a product, and $w_{\rm s}(i)$ is the weight of the species s_i;

3. Consequently, a new set of species, those found at that iteration to be related to the evolution of the important species and not considered in previous iterations, is formed. Their weights $w_{\rm s}$ are estimated as the maximum possible values of the weights $w_{\rm r}$ of the reactions they are involved in.

The iterations are finished when all species and all time steps are passed. Then one easily obtains a reduced chemical network from the full network by choosing only those reactions, that have weights above a predefined cut-off threshold.

We assume that if there is a difference greater than 30% in abundances of the important species computed with the full and reduced networks for any time moment, then the cut-off is readjusted to a new, smaller value, and the last step is repeated. Utilizing this rather strong selection criterion for the reduced networks, we preserve ourself from introducing severe computational errors in abundances of the important species.

4. Chemistry of Carbon Monoxide

We follow the approach described in the previous section to build the gas-phase and gas-grain reduced networks for CO. The carbon monoxide is chosen as the only important species to be used with the reaction-based reduction technique.

In the case of the purely gas-phase chemistry in a dense cloud the main chemical processes for the evolution of CO are the following. At very early

evolutionary stages, $t < 10^2$ years, key formation processes are the neutral-neutral reactions of oxygen with various light carbon-bearing molecules, like CH and CH_2. Later, CO is formed due to destruction of OCS, H_2CO, and CO_2 by the cosmic ray induced UV photons. The removal of CO during the entire evolutionary time is controlled by the cosmic ray ionization and destruction due to the cosmic ray induced UV photons.

The evolution of carbon monoxide under such circumstances is shown in Figure 1 (left panel). As can be clearly seen, in the absence of the gas-grain interactions the evolution of CO is rather simple – its abundance is rapidly increasing till the chemical equilibrium value of about 10^{-4} (in respect to the amount of hydrogen nuclei) is reached at $\sim 3\,10^3$ years. The rest (and most!) of the evolutionary time the abundance of carbon monoxide remains almost a constant. Remarkably, there is no difference between the high and low metallicity cases.

Applying our reduction approach, we found that one may keep from the entire set of 395 species and 3864 reactions only 8 species involved in 9 reactions in order to accurate estimation CO abundances for all 10^7 years of the evolution. The corresponding reduced network is given in Table 1. The size of this network is so small that the computational time which is needed to solve the relevant system of the ordinary differential equations (ODE) is negligible, less than a second. Still the uncertainties of the resulting abundances do not exceed 15% during the entire evolutionary time.

This extraordinary result demonstrates the power of our reduction technique and explains why there is no difference between the high and low metallicity cases. The reason is that the evolution of these 8 necessary species (see Table 1) depends only on the total amount of H, C, and O available in the gas phase at $t = 0$. As the initial abundances of these atoms are exactly the same for both metallicities, it leads to the nearly identical values of CO abundances for all $0 - 10^7$ years.

It is interesting to examine if such extremely small amount of necessary species and reactions is caused by merely favorable circumstances or it is due to the nature of the CO chemistry itself. In the latter case, the relevant reduced network must reproduce accurately the abundances of carbon monoxide in a range of the physical conditions.

We discovered that this network is functional within accuracy of 50% under the following circumstances:

$$10^4 \text{ cm}^{-3} \leq n_{\rm H} \leq 10^{10} \text{ cm}^{-3},\ T \leq 250 \text{ K},\ A_{\rm V} \geq 1$$

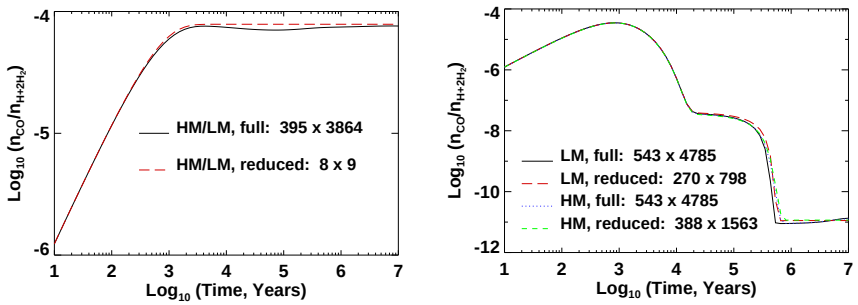

Figure 1: The evolution of CO in a dense cloud computed with the full and reduced networks in the case of the purely gas-phase chemistry (**left panel**) and the gas-grain chemistry involving the surface reactions (**right panel**). The "HM" and "LM" mean high and low metallicity cases, respectively. The sizes of the chemical networks are indicated as "$N_1 \times N_2$", where N_1 is the number of chemical species and N_2 is the number of reactions.

It implies physical conditions, typical of dense and translucent interstellar clouds and "hot cores" of molecular clouds. Thus one may use essentially the same tiny set of species and reactions in order to follow the evolution of CO in the case of the purely gas-phase chemistry in a very wide range of conditions. Compared to the similar network obtained by Ruffle et al. (2002), that has 33 species involved in 116 reactions and is valid for $n_{\rm H} \sim 10^3$ cm^{-3}, $A_{\rm V} = 4-10$, and $t > 10^5$ years our network is much smaller and still is applicable under a much wider range of the physical circumstances.

The situation is more complicated from the chemical point of view when the gas-grain interactions and the dust surface reactions are taken into account. The accretion of species onto the grain surfaces is efficient at high gas density, $n_{\rm H} = 10^7$ cm^{-3}, leading to significant amount of mantle material. Then the quantum tunneling of H and H_2 and thermal hopping of other atoms and light molecules drive the rich surface chemistry, which results in production of heavier species, mostly complex organic molecules. Occasional impulse heating of the dust grains by the energetic cosmic ray particles returns some of the surface species back to the gas phase. All these processes alter the gas-phase chemistry in a high degree.

The evolution of carbon monoxide in this case is shown in Figure 1 (right

Table 1: Reduced network for CO (DENS model)

1 $H + CH_2 \rightarrow CH + H_2$	6 $O + C_2H \rightarrow CO + CH$
2 $H_2 + C \rightarrow CH_2 + PHOTON$	7 $H_2 + CRP^a \rightarrow H + H$
3 $C + CH_2 \rightarrow C_2H + H$	8 $CH + CRPHOT^b \rightarrow C + H$
4 $O + CH \rightarrow CO + H$	9 $CO + CRPHOT \rightarrow C + O$
5 $O + CH_2 \rightarrow CO + H + H$	

[a]"CRP" is an abbreviation for "cosmic ray particle",
[b]"CRPHOT" means "CRP-induced UV photon"

panel). The abundance of the gas-phase CO is increasing at early evolutionary times, till the maximum value of $n_{CO}/n_H \sim 10^{-4}$ is reached at $t \sim 10^3$ years. Then, accretion of CO molecules onto the grains becomes efficient and its abundance in the gas phase is decreasing. The bump on the curve at $t \sim 10^4 - 10^6$ years is due to the influence of the surface reactions as they become quite important at these times. Finally, the equilibrium value $n_{CO}/n_H \approx 10^{-11}$ is reached after about 10^6 years of evolution. Again, as in the previous case, there is no difference between the high and low metallicities.

Our method of reduction is able to select two sets of 388 species and 1563 reactions for the high metallicity case and 270 species and 798 reactions for the low metallicity case. The relevant computational speed gains are only about factors of 3 and 15 for the former and latter cases, respectively. The accuracy of the predicted CO abundances is better than 15% during the entire evolutionary time.

The number of necessary species and reactions is high due to perplexity of the chemical processes in this model. Indeed, the selectivity criterion of the reduction method recognizes many of the surface reactions to be important, so they remain in the reduced chemical network. Consequently, it leads to larger amount of necessary reactions and species compared to the case of the purely gas-phase chemistry.

There is a large ($> 50\%$) difference between the number of the species found to be necessary in the high metallicity case compared to the low metallicity case. The reason is that the reduced networks with smaller amounts of species cannot be used in the calculations because the relevant ODE systems are too stiff to be solved in reasonable time. This is a common situation when the surface reactions are taken into account as they have far too high kinetic rates compared to the gas-phase chemical reactions.

5. Conclusions

We have developed a robust technique to reduce the amount of species and reactions in the chemical networks. It is shown that by utilizing this method the size of the gas-phase chemical network used to compute CO abundances in the dense clouds can be significantly reduced. We have found that such reduction is of no practical use when the gas-grain interactions and the surface chemistry are taken into account since the relevant computational time gains are about factors a few only.

Acknowledgements

DS was supported by the German *Deutsche Forschungsgemeinschaft, DFG* project "Research Group Laboratory Astrophysics" (He 1935/17-1), the work of DW was supported by the INTAS grant YS 2001-1/91 and the RFBR grant 01-02-16206.

References

Aikawa, Y., Miyama, S.M., Nakano, T., Umebayashi, T., 1996, ApJ 467, 684
Grevesse, N., Sauval, A.J., 1998, Space Sci. Rev. 85, 161
Hasegawa, T.I., Herbst, E., Leung, C.M., 1992, ApJSS 82, 167
Hasegawa, T.I., Herbst, E. 1993, MNRAS 263, 589
Hollenbach, D., McKee, C.F., 1979, ApJSS 41, 555
Lee, H.-H., Roueff, E., Pineau des Forêts, G., Shalabiea, O. M., et al., 1998, A&A 334, 1047
Millar, T.J., Farquhar, P.R.A., Willacy, K., 1997, A&AS 121, 139
Rae, J.G.L, Bell, N., Hartquist, T.W., et al., 2002, A&A 383, 738
Ruffle, D.P., Rae, J.G.L., Pilling, M.J., et al., 2002, A&A 381, L13
Wiebe, D., Semenov, D., Henning, Th., 2002, A&A, in preparation

Chemistry in Star-Forming Regions: Making Complex Modelling Feasible

D. Wiebe[1], D. Semenov[2], Th. Henning[3]

[1]Institute of Astronomy of the RAS
48, Pyatnitskaya str., Moscow 119017, Russia
[2]Astrophysical Institute and University Observatory
Schillergäßchen 2-3, 07745 Jena, Germany
[3]Max Planck Institute for Astronomy
Königstuhl 17, 69117 Heidelberg, Germany
E-mail: dwiebe@inasan.rssi.ru

Abstract

In this paper we discuss possible ways to reduce the chemical reaction network for the situations when the accurate abundances are only needed for a limited number of species to compute, for example, such dynamically important factors as the ionisation degree or molecular cooling. We show that it is possible to reduce the number of reactions and species so that the computational time in some astrophysically interesting situations will be reduced by orders of magnitude without appreciable loss of accuracy. For example, to model magnetised dark clouds, self-consistently estimating the ionisation degree with the UMIST 95 database, one only needs to retain about 100 of 395 species with the computational time cut by a factor of a hundred. In the case of dynamical modelling with changing density, extinction, UV-intensity, temperature etc., the reduced chemical network may help to distinguish between feasible and non-feasible tasks.
Keywords: *molecular processes – ISM: molecules – ISM: abundances*

1. Introduction

One of the main problems of the star formation studies is the absence of easily detectable emission from molecular hydrogen, which is the most abundant molecule in molecular clouds that are sites of star formation. Gas motion in star-forming clouds, pre-stellar, protostellar, and young stellar objects (YSO) is essentially motion of H_2 molecules. Yet we have to infer this motion observing far less abundant species.

Molecular diagnostics has now developed into effective tool for the investigation of interstellar clouds. It allows to determine physical conditions in the ISM, may help to elucidate the evolutionary state of different objects (through

the concept of chemical clock), and even sheds some light on the problem of life origins (through observations of complex organic molecules). However, species that are used as tracers for the study of the star formation are not necessarily well mixed with molecular hydrogen and thus with bulk gas. To relate observed distributions of trace molecules to that of molecular hydrogen, the modelling of the chemical evolution of the region under investigation seems to be inevitable.

There are more than 120 species that are known now to exist in the ISM. As they do not form a closed chemical system, one has to assume that many other chemical species are present there that are not (yet) observable. A typical chemical network used in the modelling of the ISM, like the UMIST 95 database (Millar et al. 1997), consists of hundreds of species and thousands of reactions. Differential equations of chemical kinetics that describe time-dependent molecule production and destruction rates are usually stiff and require special methods of solution, implemented, e.g., in LSODE and DVODE packages. Solving of these equations is a demanding computational task even for the fixed relevant physical conditions (density, temperature, extinction, etc.). But interferometric observations that are now becoming abundant allow not only to determine the chemical composition of a particular object but also reveal its detailed chemical structure. To confront these data with theoretical predictions one has to model the chemical evolution at least in several points across the object with the physical conditions that vary, in general, not only in space but also in time.

One way to do this is to place the chemical model over the pre-computed dynamical model. However, it is sometimes necessary to model the chemical and dynamical evolution of the ISM self-consistently in order to take into account a feedback that chemistry has on dynamics either through heating and cooling processes that depend on abundances of certain molecules or through chemically determined ionisation degree (Ciolek & Mouschovias 1993). This makes the situation more complicated.

Even in the case of a static cloud or a cloud with the pre-defined dynamics, modelling of its detailed chemical structure is very time-consuming, if one recalls the number of parameters that can be varied. It seems to be clear that self-consistent coupling of the full-fledged chemical model to the (more or less) full-fledged dynamical model is next to impossible, even with ever-increasing computational power.

2. Motivation and Reduction Model

While one can only guess if the chosen chemical network contains all the needed species and all the needed reactions, the natural question to ask is if we really need all this information. To compare results of chemical modelling with observational data one usually needs to compute abundances of a few selected molecules (like CO, NH_3, CS, HCN, etc.) without spending much computational time on the accurate predictions about, say, complex carbon chains. To model thermal balance in a cloud self-consistently it is in most situations enough to have accurate abundances of CO which is a major molecular coolant in interstellar clouds (Glassgold & Langer 1973). Ionisation degree is determined not by the entire species set but only by a few dominant ions that are involved in a handful of chemical reactions. Intuitively, it seems obvious that in such cases the number of species and reactions can be significantly reduced. However, for now attempts to use abridged chemical networks have been mainly based on a more or less qualitative arguments, without accurate mathematical consideration (e.g. Gerola & Glassgold 1980; Shematovich et al. 1997; Desch & Mouschovias 2001).

So, we can formulate the following task: to reduce the number of species and reactions into a subset that is necessary in a particular situation using mathematically proven arguments that will ensure reliability of the reduced network. Ruffle et al. (2002) and Rae et al. (2002) made the first attempt of this kind found in the astronomical literature. They used methods developed in different branches of science to reduce networks used in modelling of combustion processes. They show that it is possible to isolate species and reactions governing the CO abundance and the ionisation degree at the conditions typical of diffuse illuminated clouds. Their reduced network for CO contains 33 species involved in 116 reactions and is valid for $n_{\rm H} \sim 10^3$ cm^{-3} and $A_{\rm v} = 4 - 10$.

In this paper we present a similar approach to the chemical network reduction and check it for a wider range of physical conditions. We utilise two methods that we refer to as species-based reduction and reaction-based reduction. With these two methods we built reduced networks needed to compute electron and CO abundances for the conditions typical of diffuse ($n_{\rm H} \sim 10^3$ cm^{-3}) and dense ($n_{\rm H} \sim 10^7$ cm^{-3}) molecular clouds. We assume no photoprocessing by interstellar UV photons, implying obscured regions with $\rm A_V > 10$. We consider both purely gas-phase chemistry and gas-phase chemistry coupled to the surface chemistry with two different sets of initial abundances usually referred to as high and low metallicities (e.g. Lee et al. 1998).

We use the UMIST 95 rate file for the gas-phase reactions. Rates for surface

reactions are taken from Hasegawa et al. (1992) and Hasegawa & Herbst (1993). As surface chemistry is included here for illustration purposes only, the rate equation approach is used to model these reactions, even though its validity is now questioned. Gas-phase network consists of 395 species (including electrons) taking part in 3864 reactions. All 148 neutral species but helium and molecular hydrogen are allowed to stick to dust grains where they are involved in 192 surface reactions. Gas-dust connection is realized through accretion and desorption processes. Desorption energies are taken from Hasegawa & Herbst (1993) or interpolated from their data.

The species-based reduction rests upon the first part of the Ruffle et al. (2002) technique and consists of choosing species that are important in a particular context and then selecting from the entire network only those species that are necessary to compute abundances of important species with reasonable accuracy. The analysis is based on sensitivities B_i defined in Ruffle et al. (2002) as

$$B_i = \sum_{j=1,N'} \left(\frac{n_i}{g_j} \frac{\partial f_j}{\partial n_i} \right)^2 , \quad (1)$$

where n_i is the abundance of ith species, N' is the current number of important and necessary species,

$$f_j = G_j - L_j$$

is the net rate of the jth species abundance change expressed as the difference between the net gain G_j and loss L_j rates, and

$$g_j = \max(G_j, L_j).$$

With these definitions, the quantity in parentheses gives the normalised rate of jth species abundance change due to those reactions only that involve ith species. B_i value thus gives a measure of the relative importance of the ith species. The important feature of B_i values pointed out by Ruffle et al. (2002) is the clear cutoff between species with large B_i and small B_i. Before the first step the reduced set contains only important species. Then B_i values are computed for all species from the full network, and those of them, having B_i above the cut-off threshold, are added to the reduced network, and the process starts over. If after the current iteration no new species are added to the reduced network, the process stops.

In the reaction-based method analysis starts from reactions that govern the abundance of important species. All reactions in the entire network are assigned weights according to the influence they have on the abundance of an important

species. Then, only those reactions are selected that have weights above some cut-off parameter that is selected on the basis of the requested accuracy. Only those species are included in the reduced network that participate in selected reactions. Details on the algorithm of the reaction-based reduction are given in Semenov et al. (2003).

3. Ionisation Degree

To build the reduced chemical network that could be used to compute ionisation fraction in molecular clouds we adopted the following approach. First, the model was computed with the full chemical species set. Then, with the abundances of all species corresponding to $t = 0 - 10^7$ years, we estimated which of them are needed to estimate the abundances of dominant ions. Finally, we checked the reduced networks by comparing the ionisation degrees computed with the full and reduced networks.

In a purely gas-phase chemistry case, at $n_{\rm H} = 10^3$ cm^{-3} and high initial metal abundances, the dominant ions during most of the computational time are S^+ and Mg^+. By considering only ionised sulphur as an important species in species-based approach we can reduce the number of species from 395 to 123 and to achieve the computational speed gain of order of 25, but at the expense of $\sim$ 20% uncertainty at times approaching 10^7 years. If we consider both dominant ions to be important species, the number of species in the reduced set is 126, and the computational gain is almost the same with the uncertainty less than 10%. With the reaction-based reduction technique, we choose electron to be the only important species. In this case the number of necessary chemical reactions can be reduced from 3864 to 111 and the number of species from 395 to 58. The computational gain exceeds 500.

The low metallicity case is more complicated from the chemical point of view since in the absence of abundant metals the role of dominant electron suppliers goes to complex species involved in a more diverse chemistry. At this low density gas-dust connections are not important again. In the diffuse cloud case, the dominant ion is H_3^+ most of the time, however it alone does not determine the ionisation degree with enough accuracy. Errors are negligible at earlier times when the chemistry is relatively simple, however, after 10^4 years the error grows significantly, exceeding a factor of 3 at the end of computation. To account for later chemistry, one has to take into account another important ion, HCO^+. When these two species are designated as important, errors do not exceed 15% during entire computational time in the case of species-based

approach. However, due to the perplexed chemical connections of the two ions, the species set reduction is only modest in this case. About one hundred species can be excluded from the set with the reduction of the computational time by a factor of 3 (if errors like 200% cannot be afforded). The reaction-based algorithm is better suited for such situation. From the complicated chemistry involving H_3^+ and HCO^+ it is able to isolate 169 most important reactions, simultaneously reducing the number of species to 73. The speed gain in this case approaches 500, as in the high metallicity case.

Inclusion of accretion and desorption processes, as well as surface reactions, into the diffuse cloud model does not lead to any noticeable changes, primarily because the density is so low that it prevents the effective gas-grain interactions.

When no gas-dust interaction is taken into account, the case of dense cloud ($n_H = 10^7$ cm^{-3}) at high metallicity is qualitatively similar to the low-density case. The difference between high and low metallicity cases is much smaller for a dense cloud than for a diffuse cloud. In a denser environment, such chemically active ions as H_3^+ and HCO^+ are much less abundant, and metal ions dominate the ionisation degree both in high and low metallicity cases. As a result of this similarity, in a dense cloud reduced species sets are nearly the same both for high and low metallicity, with similar errors and computational gains.

The situation changes drastically, when gas-dust connection is taken into account. In high metallicity case, at early stages of the evolution the dominant ions are the same as in diffuse medium, i.e., metals. However, after 10^4 years the metal depletion becomes important, and the dominant ions are H_3^+ and HCO^+. Basically, a dense cloud at high metallicity with accretion and desorption processes behaves similarly to the low metallicity diffuse cloud.

In the low metallicity case, which is more diverse from the chemical point of view, difference between initial and final stages of the cloud evolution (separated by the moment when depletion takes over) is so prominent that the reduced network estimated from the final abundances is not valid at earlier phase, at $t < 10^4$ years, leading to a factor of 2 errors, even though it still predicts later abundances with much better accuracy (less than 20%). In order to take the two different stages into account, we build the reduced set for two times, $t \sim 10^3$ years and 10^7 years, and then use the combined set during the entire time span.

The addition of surface chemistry changes the evolution of the ionisation degree somewhat, but in the absence of effective desorption mechanisms these changes are not strong enough to affect the list of necessary species, so that it is possible to use the same reduced sets as in the case when only accretion and desorption are taken into account, with similar accuracy and computational

gain. Both methods are able to remove about two hundred species from the entire network with the gas-grain interaction (remember that the full network consists of 542 species in this case). This reduction provides the decrease of the computational time by a factor of a few. The greatest speed gain (~ 8) in the model with surface reactions included is achieved with the reaction-based technique due to its ability to remove not only excessive species but excessive reactions as well.

4. Carbon Monoxide

Reduction results for CO are more impressive if no surface chemistry is taken into account. For both metallicities and both cloud densities, the reduced set consists of no more than 35 species and provides accuracy better than 20%. Even though we build reduced sets for each of the considered models separately, it is possible to use a common reduced set for all of them with error less than 100%. This is true both in the case of the purely gas-phase chemistry and in the case when accretion and desorption processes are taken into account. The resulting speed gain is very large. In fact, while it takes about 5 minutes to run the full model, with the reduced network time needed to compute the CO abundance is lost in technical operations (like input/output etc.).

The reduction is most effective in a dense cloud. The reaction-based method shows that 8 species and 9 reactions completely determine the CO abundance when only gas-phase reactions are taken into account (for more details see Semenov et al., 2003).

The situation changes drastically again if surface reactions are switched on. In this case the species-based reduction is less effective. The reduced set contains about 340 species and produces overabundance of CO at later times, when depletion becomes important. The species-based reduction has the disadvantage of not being able to include properly surface molecules. To obtain reasonable results one has to add manually surface species that serve as sinks for surface CO, that is, CO_2 and HCO. The computational gain is only about 2. When surface reactions are taken into account, reaction-based reduction provides modest computational gain, too, though somewhat larger than species-based reduction, with more controllable accuracy and without the need of manual corrections. The speed gain is only about 3 in the high metallicity case, but reaches 16 in the low metallicity case.

So, the species-based reduction is an effective tool for constructing limited chemical networks in situations that do not involve surface chemistry. When

surface reactions are taken into account, species-based reduction is not that effective and reliable. The reaction-based method gives more impressive results.

5. Conclusions

We show that purely gas-phase chemical networks can be significantly reduced to compute electron and CO abundances in dark clouds. The computational gain varies from a few tens up to the point where the computational time needed for chemical modelling is lost in service operations. If the surface chemistry is included, both methods are only able to accelerate the computation by a factor of a few.

Acknowledgements

DS was supported by the German *Deutsche Forschungsgemeinschaft, DFG* project "Research Group Laboratory Astrophysics" (He 1935/17-1). Work of DW was supported by the INTAS grant YS 2001-1/91 and the RFBR grant 01-02-16206.

References

Ciolek, G.E., Mouschovias, T.Ch., 1993, ApJ 418, 774
Desch, S.J., Mouschovias, T.Ch., 2001, ApJ 550, 314
Glassgold, A.E., Langer, W.D., 1973, ApJ 179, 147
Gerola, H., Glassgold, A.E., 1978, ApJS 37, 1
Hasegawa, T.I., Herbst, E., Leung, C.M., 1992, ApJS 82, 167
Hasegawa, T.I., Herbst, E., 1993, MNRAS 263, 589
Millar, T., Farquhar, P., Willacy, K., 1997, A&AS 121, 139
Rae, J.G.L., Bell, N., Hartquist, T.W., et al., 2002, A&A 383, 738
Ruffle, D.P., Rae, J.G.L., Pilling, M.J., Hartquist, T.W., Herbst, E., 2002, A&A 381, L13
Shematovich, V., Wiebe, D., Shustov, B., 1997, MNRAS 292, 601
Semenov, D., Wiebe, D., Henning, Th., 2003, "Reducing and Analyzing Chemical Networks", Comm. Konkoly Obs. 103, proc. of the conf. "The interaction of stars with their environment II.", eds. Cs. Kiss et al., p.59

Molecular Emission from G345.01+1.79

S.V. Salii[1], A.M. Sobolev[1], N.D. Kalinina[1] S.P. Ellingsen[2], D.M. Cragg[3], P.D. Godfrey[3], P. Harjunpää[4], I.I. Zinchenko[5]

[1]Astronomical Observatory of Ural State University
620083, Ekaterinburg, Lenin str. 51, Russia
E-mail: Svetlana.Salii@usu.ru, Andrej.Sobolev@usu.ru
[2]University of Tasmania, Hobart, Australia
[3]Monash University, Clayton, Australia
[4]Helsinki University, Helsinki, Finland
[5]Institute of Applied Physics, N.Novgorod, Russia

Abstract

We present SEST observations of G345.01+1.79 in maser and 'quasi-thermal' lines of CH_3OH, lines of SiO, CS and some other shock tracing molecules. For the first time weak methanol maser emission was detected at frequencies 165.05 and 165.06 GHz. The observed 'quasi-thermal' CH_3OH and SiO (2-1) lines display pronounced blue wings confined to the G345.01+1.79(S) position. Velocities of CH_3OH and OH maser features lie well within the wing. So, there is a high probability that interaction of the wind from the young star with ambient material is responsible for the creation of masers and production of the blue non-gaussian wing. Comparison of velocities for 'quasi-thermal' and maser lines shows that the bow shock velocity relative to the bulk of cloud material is about 10 kms^{-1}. So, most probably we are dealing with the first clear example of an ultracompact HII region moving through a molecular cloud. Modelling of CH_3OH 'quasi-thermal' emission and consideration of maser profiles shows that the cloud material is greatly inhomogeneous.
Keywords: *stars: formation – ISM: clouds – ISM: molecules – radio lines*

1. Introduction

The southern molecular cloud G345.01+1.79 (hereafter G345) shows various signs of interaction of young massive stars with their environment.

G345 displays strong emission in methanol (CH_3OH), hydroxyl (OH) and water vapor (H_2O) maser transitions (Caswell et al., 1995b; Caswell & Haynes, 1983; Caswell et al., 1983; Braz & Epchtein, 1983). VLBI observations have shown that the source contains 2 Class II CH_3OH maser sites, G345(S) and G345(N), according to Norris et al. (1993) notation. Positions of OH masers

coincide with those of CH_3OH masers in G345(S) (Caswell, 1997; Caswell et al., 1995b). H_2O masers in G345 are situated apart from IRAS point source and near infrared sources (NIR) (Testi et al., 1994). They presumably correspond to the sites containing young stellar objects (YSO) at the stages preceding formation of ultracompact HII regions (UCHII)(Cesaroni et al., 1997). Observations by Testi et al. (1994) have shown that the G345(S) OH maser site is situated at the edge of a strong NIR source coincident in position with IRAS16533-4009. Infrared spectrum obtained by Volk et al. (1991) indicates that this source is an UCHII. Interferometry by Caswell (1997) places CH_3OH and OH masers in G345(S) on the western side of UCHII radio continuum image.

2. Observations

The observations were made in October 1997 and March 1999 with the SEST(Swedish-ESO Submillimetre Telescope, La Silla, Chile). The molecular cloud was mapped in SiO(2-1), CH_3OH $5_K - 4_K$ and $C^{34}S$(5-4) lines. Altogether 54 positions were observed with a $20''$ spacing. Direction ($\alpha_{1950.0} = 16^h53^m19.7^s$, $\delta_{1950.0} = -40°09'46''$) toward the methanol maser cluster G345(S) was chosen as a map center. A number of additional lines were observed toward this position. Full list of observed lines includes 32 lines of CH_3OH and the lines of SiO, HCN, HCO^+, DCN, $C^{34}S$, $C^{33}S$, $C^{18}O$, ^{13}CO, H_2S, and SO at frequencies around 80, 86, 88, 96, 110 156, 165, 216 and 241 GHz.

3. SiO

The SiO(2-1) and (5-4) lines peak at V_{LSR} about –15 kms^{-1}. They exhibit asymmetric wing emission extending from about –50 kms^{-1} on the blue-shifted side to +10 kms^{-1} on the red-shifted side. In the SiO(5-4) spectrum the blue wing is more pronounced while the intensity of this line is lower. The SiO(2-1) spectrum towards the map center is shown in Fig.1.

Velocity channel maps for the SiO(2-1) emission over the range –50→ 10 kms^{-1} are shown in Fig.2. The wing emission in four ranges corresponding to high-velocity and low-velocity blue-shifted wings ($-50 \rightarrow -25$ kms^{-1} and $-25 \rightarrow -18$ kms^{-1}, respectively), and low- and high-velocity red-shifted wings ($-12 \rightarrow -8$ kms^{-1} and $-8 \rightarrow 10$ kms^{-1}, respectively) are shown as contour maps. The distribution of the line core emission ($-18 \rightarrow -12$ kms^{-1}) is shown as a grey scale image in each panel.

SiO emission from the quiescent gas ($-18 \rightarrow -12$ kms^{-1}) peaks near the

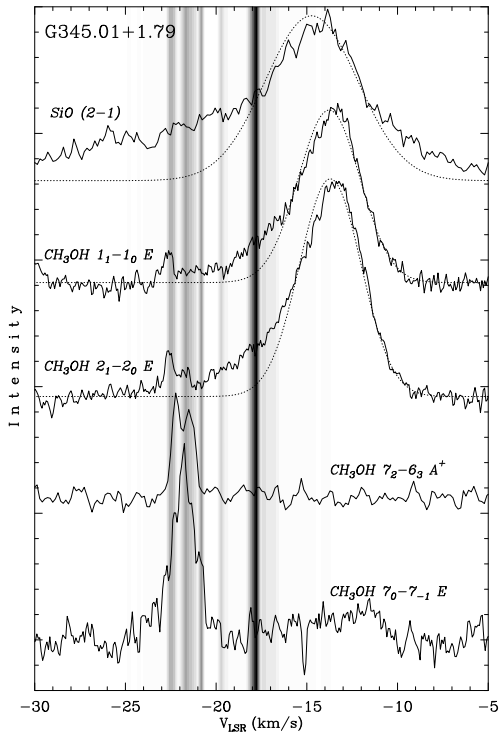

Figure 1: Non-gaussian wings in the spectra of SiO (2-1) and CH_3OH quasi-thermal lines and weak CH_3OH maser lines toward G345(S). Intensity of SiO (2-1) line is 0.6 K, intensities of the CH_3OH lines are listed in the table. Spectrum of the CH_3OH $5_1 - 6_0$ A^+ maser line is shown by shades of grey

methanol maser cluster G345(N). The low-velocity wing emission ($-25 \rightarrow -18$ and $-12 \rightarrow -8\,\mathrm{kms}^{-1}$) is extended. The emission in the low-velocity blue wing is more extended and the intensity maximum is located $10''$ west of G345(N), while emission in the low-velocity red wing peaks $30''$ east of G345(N).

The high-velocity blue-shifted wing emission ($-50 \rightarrow -25\,\mathrm{kms}^{-1}$) is clearly concentrated to the western side of the map and the intensity maximum lies at $(20'', 20'')$, i.e., about $30''$ west of G345(N). Weak high-velocity red-shifted emission ($-8 \rightarrow 10\,\mathrm{kms}^{-1}$) arises predominantly east of G345(N). Separate blue- and red-shifted high-velocity wing emission regions suggest the presence of a bipolar molecular outflow. Its central source is probably located near G345(N) and its projected position angle in the plane of the sky is close to 90°.

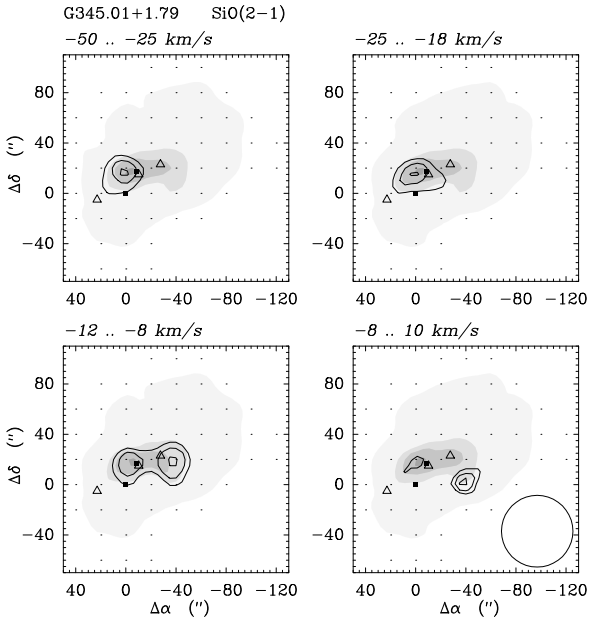

Figure 2: Channel maps of the SiO line wing emission (contours) superimposed on the line core emission (grey scale). The locations of 6.7 GHz methanol maser sites G345(S) and G345(N) are marked by filled squares, and locations of H_2O masers (Caswell et al., 1983) are marked by open triangles. The half power beam size is shown in the lower right panel

4. Methanol

Distribution of methanol emission in G345 resembles that of SiO. However, CH_3OH lines are considerably narrower indicating that turbulent motions are more developed in SiO abundant regions.

CH_3OH lines manifest strong and extended non-gaussian wings (see Fig.1). The blue wing is most pronounced at the map center. Noteworthy that velocities of components of the brightest CH_3OH maser ($5_1 - 6_0$ A^+ at 6.7 GHz) toward G345(S) correspond to velocities of the blue wing of the CH_3OH and SiO lines (Fig.1).

One remarkable feature of the G345(S) maser site is that the maser spots show clear increase in V_{LSR} with the distance from the center of UCHII (Norris et al., 1993). Such a velocity pattern corresponds well to the motions of matter in the wake of the bow shock produced by the movement of UCHII ionizing star toward the observer (Van Buren et al., 1990; Raga et al., 1997).

Other feature of G345(S) is that maser spots show dramatic increase in the ratio of fluxes of 6 GHz and 12 GHz methanol maser lines (hereafter F6 and F12, respectively) with the distance from UCHII center. Indeed, comparison

Table 1 CH_3OH weak maser components of molecular cloud G345.01+1.79

Frequency MHz	Transition	Area $Kkms^{-1}$	V_{LSR} kms^{-1}	ΔV_{LSR} kms^{-1}	T_A^* K
86903.06	$7_2 - 6_3 A^+$	0.46(0.02)	-21.82(0.03)	1.33(0.06)	0.33
156488.95	$8_0 - 8_{-1} E$	4.33(0.13)	-19.08(0.10)	3.33(0.22)	1.22
156602.42	$2_1 - 3_0 A^+$	1.32(0.13)	-20.62(0.10)	2.56(0.27)	0.49
156828.51	$7_0 - 7_{-1} E$	3.06(0.07)	-21.78(0.02)	1.76(0.05)	1.66
157048.62	$6_0 - 6_{-1} E$	3.98(0.12)	-21.11(0.05)	2.96(0.11)	1.27
157178.97	$5_0 - 5_{-1} E$	4.72(0.13)	-21.24(0.04)	2.88(0.10)	1.54
157246.10	$4_0 - 4_{-1} E$	3.82(0.12)	-21.73(0.04)	2.99(0.13)	1.20
165050.19	$1_1 - 1_0 E$	0.06(0.01)	-22.64(0.06)	0.60(0.14)	0.09
165061.16	$2_1 - 2_0 E$	0.12(0.02)	-22.46(0.09)	1.12(0.23)	0.10
216945.60	$5_1 - 4_2$ E	0.27(0.14)	-20.45(0.92)	3.29(1.57)	0.08

with spectra from Caswell et al. (1995a,b) show that F6/F12 is about 0.35 for the –23.8 kms^{-1} feature and increases to more than 150 for the –18 kms^{-1} feature.

From the point of view of Class II CH_3OH maser modelling given in Sobolev et al. (1997a,b) such an F6/F12 behavior for the bright maser spots can be explained by the increase of UCHII emission dilution, decrease in hydrogen number density and increase of maser beaming with the distance from UCHII center. Increase of dilution of UCHII emission with offset is straightforward. However, the difference in F6/F12 is too big to be explained by this effect alone. So, we think that the phenomenon is borne by combined action of mentioned factors. This is likely to take place since the increase of offset from the head of bow shock is followed by 1) increasing CH_3OH column density of less dense material and 2) increasing ratio of radial to tangential dimensions of emitting region which brings higher beaming.

In order to elucidate the situation with weaker Class II CH_3OH masers in G345(S) we performed observations of methanol maser candidates.

In the 10 lines listed in the table we detected components with velocities –24 – –20 kms^{-1} which are about 10 kms^{-1} lower than velocities of the quasi-thermal methanol lines. At the same time they show good agreement with velocities of maser features observed in Class II maser lines (Fig.1). The lines are narrow and we believe that they are really masers despite their quite low intensities. Our observations borne clear detection of new weak methanol masers at 165.05 and 165.06 GHz and marginal detection of maser at 216.9 GHz.

Maser modelling presented in Sobolev et al. (1997b) shows that different maser lines may form in different regimes. This is in accordance with our observations displaying noticeable difference in the line profiles shown in Fig.1.

Thus, observations of weaker methanol maser lines indicate that the physical conditions in G345(S) maser formation region are strongly inhomogeneous.

5. Non-LTE modelling of methanol emission

The LVG modelling of methanol emission at map center position provides much better fit than the rotational diagram (see Fig.3) indicating that excitation of methanol lines in this object exhibits great departures from LTE. Moreover, considerations of the previous sections provide evidence that molecular material in G345 is greatly inhomogeneous.

So, we dared to make a step further in order to investigate possible variation of parameters of cloud constituents. In order to do that we applied 2-component LVG modelling of quasi-thermal emission in methanol lines. Fig. 3 clearly shows that the 2-component modelling provides much better fit to observational data. Results of this modelling demonstrate inhomogeneity of molecular material in G345 and will be described in a separate paper.

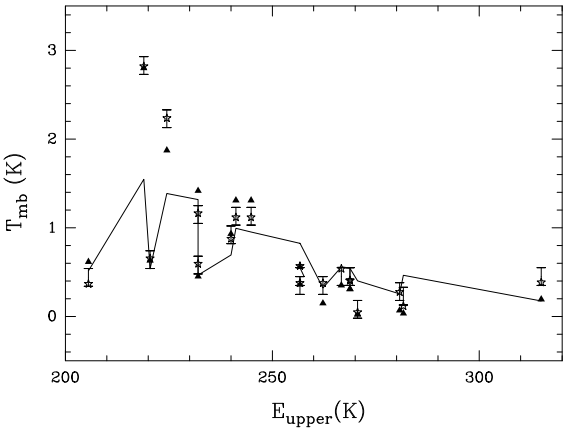

Figure 3: Results of LVG modelling of emission in 'quasi-thermal' methanol lines from map center position. Error bars show observed intensities; solid line connects intensities of rotational diagram; triangles show intensities of the best 1-component LVG fit and stars show intensities from 2-component LVG modelling

6. Conclusions

The G345.01+1.79 cloud was observed in a number of molecular lines. For the first time a weak methanol maser emission in the lines at 165.05 and 165.06 GHz was detected. Maser component in the 216.94 GHz line was marginally detected.

Presence of extended emission of shock tracing molecules shows that the molecular material in the cloud is greatly affected by the passage of shock waves.

Analysis of SiO line emission indicates possible presence of an outflow.

Consideration of the data on methanol and hydroxyl masers in G345(S) maser site suggests that these masers are formed in the region affected by the passage of bow shock borne by interaction of the wind from the young star moving toward the observer with material of the bulk of the G345 cloud. This hypothesis explains observed maser spectra and velocity pattern of maser spots.

LVG modelling of methanol line emission and consideration of methanol maser line profiles show that the molecular material in G345 is greatly inhomogeneous.

Acknowledgements

Studies were supported by INTAS, RFBR and ARC.

References

Braz, M.A., Epchtein, N. 1983, A&AS 54, 167
Caswell, J.L., 1997, MNRAS 289, 203
Caswell, J.L., Batchelor, R.A., Forster, J.R., Wellington, K.J., 1983, Austral.J.Phys. 36, 401
Caswell, J.L., Haynes R.F., 1983, Austral.J.Phys. 36, 361
Caswell, J.L., Vaile, R.A., Ellingsen, S.P., Norris, R.P., 1995a, MNRAS 274, 1126
Caswell, J.L., Vaile, R.A., Ellingsen, S.P., et al., 1995b, MNRAS 272, 96
Cesaroni, R., Felli, M., Testi, L., et al., 1997, A&A 325, 725
Norris, R.P., Whiteoak, J.B., Caswell, J.L., et al., 1993, MNRAS 412, 222
Raga, A.C., Mellema, G., Lundqvist, P., 1997, ApJS 109, 517
Sobolev, A.M., Cragg, D.M., Godfrey, P.D., 1997a, A&A 324, 211
Sobolev, A.M., Cragg, D.M., Godfrey, P.D., 1997b, MNRAS 288, L39
Testi, L., Felli, M., Persi, P., Roth, M., 1994, A&A 288, 634
Van Buren, D., MacLow, M.M., Wood, D.O.S., Churchwell E., 1990, ApJ 353, 570
Volk, K., Kwok, S., Stencel, R.E., Brugel, E., 1991, ApJS 77, 607

Young Stars

ISOPHOT Observations of the Circumstellar Environment of Young Stars

P. Ábrahám

Konkoly Observatory of the Hungarian Academy of Sciences
H-1525 Budapest, P.O. Box 67, Hungary
E-mail: abraham@konkoly.hu

Abstract

ISOPHOT, the photometer on-board the *Infrared Space Observatory*, provided new photometric and spectrophotometric data on a number of pre-main sequence stars in the 2.5–200μm wavelength range. We review the capabilities of ISOPHOT for observing YSOs, briefly report on several projects related to Herbig Ae/Be, T Tau, and FU Ori-type stars, and describe our plans for compiling a homogeneous and easy-to-use photometric catalogue of all young star observations perfomed by ISOPHOT.

KEYWORDS: *Star formation: Herbig Ae/Be stars, T Tau stars, FU Ori stars – Circumstellar matter: accretion disks – instrument: ISO, ISOPHOT – observations: photometry, spectrophotometry*

1. Introduction

In the early phases of their evolution stars are intimately linked to their environment. The spatial and density structure of their circumstellar disk/envelope can be traced by thermal emission of the dust component at infrared wavelengths. 15 years after the successful IRAS mission the *Infrared Space Observatory* (ISO, Kessler et al., 1996) provided new infrared data on the Young Stellar Object (YSO) population during its 28 months cryogenic phase.

Four years after the ISO mission, however, only part of this rich database is published and many observations are still waiting for analysis in the public ISO Archive*. This is also true for ISOPHOT, the imaging photo-polarimeter on-board ISO (Lemke et al., 1996). In many cases the original observers stopped working on their data because (i) the consolidation of the instrumental calibration took several years (and is still on-going for certain observing modes) and this timescale did not fit into the publication plan of the observers; (ii) the necessary exposure time per object turned to be longer than was anticipated prior the mission thus the target list of the proposals had to be cut back seriously.

*www.iso.vilspa.esa.es/IDA

For some proposals of statistical nature the original scientific goal became unrealistic and the observers were not interested in analysing a limited number of individual sources instead of evaluating statistical samples. All these data are freely downloadable now from the ISO Archive for analysis and publication.

In this contribution we discuss ISOPHOT observations of YSOs, with the hope of triggering new interest in the analysis of the archive data. First we review the main technical parameters of ISOPHOT, with special emphasis on the possibilities which could bring new type of information on YSOs. Then, as example, I report on several on-going or finalized YSO projects I was involved in. Finally, future plans are summarized concerning the publication of all YSO-related ISOPHOT data in a photometric catalogue. This catalogue could also be of great help in designing observations for future infrared space missions.

2. ISOPHOT's capabilities for observing YSOs

For a general description of the ISOPHOT instrument we refer to the ISOPHOT Handbook (Laureijs et al. 2002). In this section we discuss only those instrumental aspects which turned to be of special importance for YSO observations.

Photometry: multi-filter observations. The four photometric points of IRAS at 12, 25, 60, and 100μm were useful in identifying YSO candidates but were not sufficient to constrain models on morphology, mass and temperature distribution, heating mechanism and chemical composition. ISOPHOT was designed to provide SEDs in the 3.6–200μm range with much finer spectral sampling. The observer could select up to 24 filters, some of them centred on specific wavelengths, e.g. on PAH emission feaures. In practice typically not more than 4–10 filters were used (with higher preference for the broad-band continuum as well as the IRAS-compatible filters) due to time limitations. Because of the large variety of selectable observing modes, detectors, filters, and apertures, a single accuracy figure cannot be derived for ISOPHOT.

Photometry: spatial resolution. Though the mirror diameters of IRAS and ISO were identical (60 cm), ISOPHOT's design allowed to reach higher spatial resolution. It was a great advantage in observations of YSOs which are often located within dense molecular clumps. ISOPHOT's higher spatial resolution at far-infrared wavelengths was crucial to reduce contamination by the clumps' emission and obtain more precise photometry of the central source.

Shortward of 100 micron a series of apertures was available, and the one matching best the Airy-disk could be selected by the observer. In the 60–105μm range a 3×3 mini-camera could be used, whose pixel size of 43.5″×43.5″ was larger than ideal for matching the PSF (FWHM: 21″ at 60μm, 37″ at 105μm), but it represented a significant improvement compared to the 100 micron detectors of IRAS (3′×5′). At $\lambda > 105\mu$m a 2×2 camera with pixel sizes of 89″×89″ was available. Its angular resolution – dictated again by the pixel size rather than by the PSF – was 1.5′×1.5′, in the order of the IRAS 100 micron detector. Unfortunately, in many observations larger than ideal apertures were used and confusion within the beam remained one of the main limiting factors for the accuracy of far-infrared ISOPHOT observations.

There were a number of observations intended to resolve the extended envelopes of selected YSOs. Most of these measurements, however, utilized the PHT32 (oversampled) observing mode which suffered from serious instrumental problems and is still difficult to calibrate. On the other hand, observations in other modes were able to measure the size of small extended sources of 30–60″.

Mid-infrared spectrophotometry of YSOs is a good tool to detect – in addition to the continuum due to photospheric emission or to radiation of the inner warm part of the accretion disk – broad spectral features like the one of amorphous silicate around 9.7μm, the set of features attributed to PAHs (3.3, 6.3, 7.7, 8.6, 11.3μm), interstellar ices towards deeply embedded objects, the signature of crystalline silicate, etc. The grating spectrophotometer ISOPHOT-S covered simultaneously the 2.5–4.9μm and 5.8–11.6μm ranges with a spectral resolution of about 100, and delivered low-resolution spectra of young objects too faint for the higher resolution ISO-SWS instrument.

Far-infrared mapping. Star forming regions as well as the environment of YSOs could be mapped with the two far-infrared cameras. Especially the $\lambda > 100\mu$m maps are unique and provide information on molecular cloud structure, on the initial phases of star formation, and on the distribution of cold dust in the vicinity of more evolved YSOs.

Polarimetry. For completeness we mention the polarimetric capability of ISOPHOT which was used only occasionaly for young stellar objects. An example for such a programme which searched for polarization towards NGC 7538 IRS9, HH 100 IR, and L1551 IRS5 at 25 micron was presented by Wright & Laureijs (1999).

Simultaneous SED. The possibility to observe the full 3.6–200μm SED and obtain mid-infrared spectrophotometry quasi-simultaneously (within a timescale of 1-2 hours) was important for some projects looking for temporal variation of the infrared emission. As an example we refer to Sect. 3.4 where photometric observations of five FU Ori-type stars are presented.

3. ISOPHOT observations of young stars

A number of ISOPHOT observing programmes were initiated to obtain detailed SEDs of young stars. The results are usually compared with model predictions; first of all with the expected spectral shape of a geometrically-thin, optically-thick circumstellar disk ($\lambda F_\lambda \propto \lambda^{-4/3}$). Deviations from this shape are interpreted in terms of structural changes in the circumstellar matter: deficiency at near-infrared wavelengths may indicate an inner hole while a too high far-infrared flux (which is typically the case) is the signature of a flared outer disk or of an envelope. Low-density gaps dynamically cleared by companions cause dips in the SED at the corresponding wavelengths.

3.1. Far-infrared photometry of Herbig Ae/Be stars

Herbig Ae/Be stars represent the pre-main sequence evolutionary phase of intermediate mass (2–8 $M_\odot$) stars. We observed 7 of these stars to deduce the structure of their circumstellar matter from the SEDs (Ábrahám et al. 2000). Since Herbig Ae/Be stars are often embedded in dense molecular clumps ISOPHOT's higher spatial resolution at far-infrared wavelengths was crucial to reduce contamination by the clumps' emission. Fig. 1 presents our results for two stars.

The SED of LkHα 233, composed of ISOPHOT and IRAS photometry as well as data from the literature, can be described by a power-law in the 5–60μm range. The peak of the SED was predicted at around 100μm by the earlier IRAS measurement, but our 90μm photometry showed that the larger beam of IRAS was contaminated at this wavelength and the circumstellar region of LkHα 233 contains mainly material warmer than 90 K (see Fig. 1). A high resolution ISOPHOT scan at 150μm (not presented here) supports this result by detecting only the clump with no indication for the star. These results fully support a geometrically thin accretion disk model for LkHα 233 as proposed by Leinert et al. (1993).

The other Herbig Ae/Be star, MWC 1080, shows a completely different SED: the flux density is constant in the mid-infrared but the spectrum exhibits a steep raise starting between 20 and 25μm as revealed by the ISOPHOT data

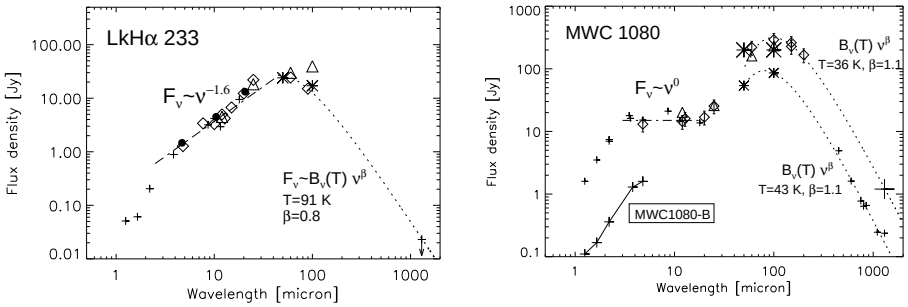

Figure 1: Spectral energy distributions of 2 Herbig Ae/Be stars. *Diamonds:* ISOPHOT; *dots:* UKIRT/MAX; *triangles:* IRAS; *small plus signs and asterisks:* ground-based and KAO observations of small beam size; *large plus signs and asterisks:* ground-based and KAO observations of large beam size (from Ábrahám et al. 2000).

points at these two wavelengths. The strong emission peak centred at 100μm has been thought to originate from the circumstellar region of the star. The typical temperature of the emitting material, however, is almost the same in the large 3′ beam of ISOPHOT and in the smaller ∼20″ aperture used in several KAO and SCUBA observations. The lack of temperature gradient towards the central source indicates that the heating of the emitting dust is independent of MWC 1080, and is more likely due to the embedded cluster of stars seen on K-band images around the Herbig star. Thus models of the circumstellar structure of MWC 1080 do not have to reproduce the far-infrared peak of the SED which is to a large extent unrelated to the central source. The true far-infrared spectrum of MWC 1080 at $\lambda > 20\mu$m cannot be determined from our observations because it would require a significantly higher spatial resolution than available at the moment.

3.2. Circumstellar structure of T Tauri stars

In an on-going project we are studying 34 T Tauri-type stars by analysing their 3.6–200μm SEDs composed of 8–12 ISOPHOT photometric bands. More than half of the sample consists of binary stars. Our goals are twofold: (1) taking advantage of the unprecedented filter coverage of ISOPHOT we determine a detailed SED and compare it with models, e.g. the ones proposed by Chiang & Goldreich (1997); (2) in a young binary system the evolution of the circumstellar disks may depend on the separation and the orbits of the components. Sorting

the binaries in our sample according to the separation of their components and looking for systematic changes in the shape of their SEDs we could shed some light on the size and structure of the circumstellar disks in binary systems. Since the flux density of T Tau stars typically varies within one order of magnitude in the whole infrared range, this comparison requires photometric accuracies around 10% which is a challenge even to the present calibration of ISOPHOT. On the other hand contamination in the beam is less problematic than in the cases of Herbig Ae/Be stars, since T Tau stars are usually not able to heat up their environment creating an extended emitting area around the source.

In Fig. 2 we present some preliminary results. The SED of AK Sco, a binary system, is an example for a rather typical case: the infrared excess emission follows a power-law in the 15–60μm range and peaks around 60μm. At longer wavelengths the emission drops quickly demonstrating the lack of a significant amount of cold dust in the system. The environment of MWC 863 is probably different from that: the emission peak at 20μm indicates a higher average dust temperature, i.e. the outer part of the accretion disk seems to be completely missing. The SED of LkHα 332-20 is virtually very noisy. However, the high flux around 10μm originates from a strong silicate emission feature, and the alternation of peaks and dips at 25, 60, and 100μm are reproduced by the earlier IRAS data, too. Thus the relatively low 60μm emission might be a signature of a low-density ring in the disk.

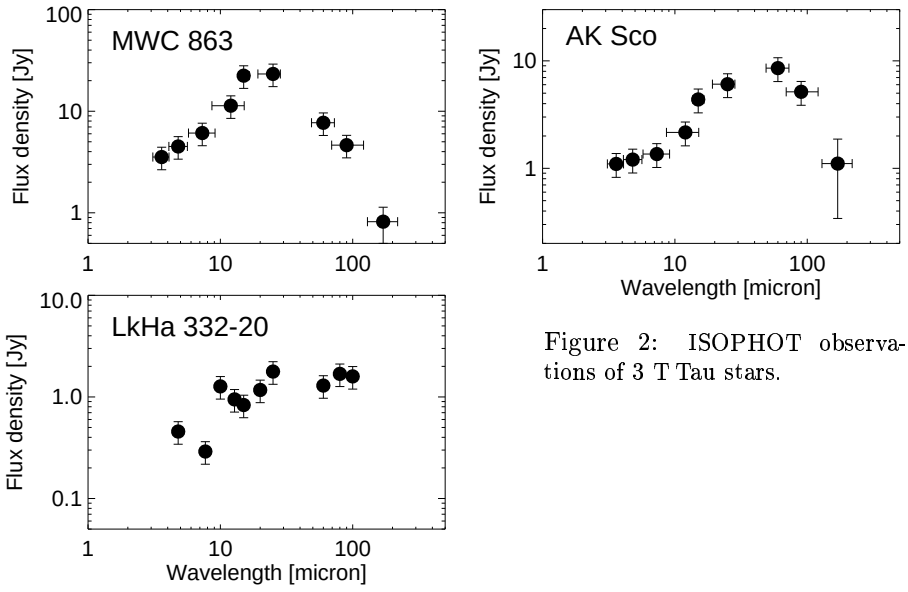

Figure 2: ISOPHOT observations of 3 T Tau stars.

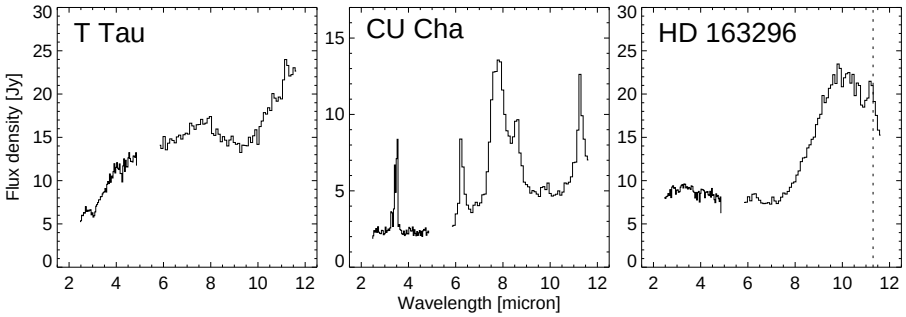

Figure 3: Mid-infrared spectrophotometry of 3 YSOs. T Tau exhibits a strong silicate absorption at 10μm, probably due to the infrared component T Tau-S. CU Cha, an A0-star, emits enough UV photons to excite PAH molecules. In HD 163296 the weak emission feature at 11.3μm on top of the strong 10μm amorphous silicate emission was also observed by ISO-SWS and is attributed to the presence of crystalline silicate.

3.3. Mid-infrared spectrophotometry of YSOs

During the ISO mission the ISOPHOT-S subinstrument performed about 90 observations on YSOs. We are working on an atlas including all these measurements. The atlas will contain 23 observations of embedded objects, 26 spectra of T Tau stars, 17 intermediate-mass pre-main sequence stars, as well as repeated observations of several FU Ori, EX Lup, and UX Ori-type objects. Fig. 3 shows three spectra as examples.

3.4. Evolution of FU Ori-type stars as seen by ISOPHOT

An FU Ori outburst is defined as a dramatic increase in the brightness of a T Tauri-type star (ΔV=4–6 mag). Since the phenomenon is connected to the circumstellar medium (probably caused by the increased accretion rate) the infrared emission spectrum is also expected to change during and after the outburst. The wavelength dependence of the change – which has never been observed before – provides crucial information on this physics of the phenomenon.

We studied 5 FU Ori stars and compiled their SEDs from the ISOPHOT data supplemented with other (2MASS, MSX, etc.) observations performed during the ISO mission (1995-98). These SEDs were compared with 15 years earlier ones derived from the IRAS photometry as well as from ground-based observations carried out around 1983. In 3 cases no difference between the two epochs was seen within the measurement uncertainties, but in one case the

shorter wavelength part of the spectrum ($\lambda \leq 20\mu$m) has decreased by a factor of 2, and in the 5th case a marginal fading was observed. The definite case (V1057 Cyg) shows wavelength-independent fading below 20μm, indicating that the energy source of the inner part of the disk is more re-processed starlight than accretion luminosity. We plan to analyse also similar observational sequences of several other FU Ori and EX Lup type stars.

4. Future work

At Konkoly Observatory we plan to collect and publish all YSO observations of ISOPHOT in a photometric catalogue which, together with the ISOPHOT-S spectral atlas, could be part of ISOPHOT's heritage in the field of star formation. In the catalogue also size of the objects and predicted confusion noise will be included. The database will serve as input catalogue for proposals for future infrared instruments like SIRTF and Herschel.

Acknowledgements

This work has been partly supported by Hungarian Research Fund (OTKA T037508). P.Á. acknowledges the support of the Bolyai Fellowship.

References

Ábrahám, P., Leinert, Ch., Burkert, A., et al., 2000, A&A 354, 965
Chiang, E.I., Goldreich, P., 1997, ApJ 490, 368
Kessler, M.F., Steinz, J.A., Anderegg, M.E., et al., 1996, A&A 315, L27
Laureijs, R.J., et al., 2002, The ISO Handbook Vol. IV, ESA SAI-99-069/Dc, Ver.2.0
Leinert, Ch., Haas, M., Weitzel, N., 1993, A&A 271, 535
Lemke, D., Klaas, U., Abolins, J., et al., 1996, 1996, A&A 315, L64
Wright, C.M., Laureijs, R.J., 1999, ESA-SP 435, 49

Mid-infrared Observations of Brown Dwarfs and their Disks: First Ground-based Detection

D. Apai[1,2], I. Pascucci[1,2], Th. Henning[1,2], M.F. Sterzik[3], R. Klein[2], D. Semenov[2], E. Günther[4], B. Stecklum[4]

[1] Max Planck Institute for Astronomy
Königstuhl 17, Heidelberg, D-69117 Germany
E-mail:[1]apai@mpia-hd.mpg.de
[2] Astrophysical Inst. and University Obs. Jena
Schillergässchen 2-3, D-07745 Jena, Germany
[3] European Southern Observatory
Alonso de Cordova 3107, Vitacura, Casilla 19001, Santiago 19, Chile
[4] TLS Tautenburg
Sternwarte 5, D-07778 Tautenburg, Germany

Abstract

We present the first mid-infrared (MIR) detection of a field brown dwarf (BD) and the first ground-based MIR measurements of a disk around a young BD candidate. We prove the absence of warm dust surrounding the field BD LP 944-20. In the case of the young BD candidate Cha Hα2, we find clear evidence for thermal dust emission from a disk. Surprisingly, the object does not exhibit any silicate feature as previously predicted. We show that the flat spectrum can be explained by an optically thick flat dust disk.

KEYWORDS: *accretion, accretion disks — circumstellar matter — stars: individual (LP 944-20, Cha Hα2) — stars: low-mass, brown dwarfs*

1. Introduction

Brown Dwarfs (BDs) occupy the substellar mass domain. Having masses lower than 75 M_{Jup}, they are unable to burn hydrogen steadily. Although their presence has been already predicted in the sixties by Kumar (1963), their low luminosity delayed their discovery until 1995, when Nakajima et al. (1995) announced the first detection of a BD orbiting the nearby M-dwarf star Gl229A. Recently, the large-scale near-infrared (NIR) surveys 2MASS and DENIS – complemented by optical data – substantially increased the number of known field BDs. Additionally, deep NIR surveys of star-forming regions revealed hundreds of young BD candidates.

In spite of the rapidly growing number of known BDs (Basri, 2000), we do not know if they form like planets or like stars. Proposed scenarios include the straightforward star-like formation via fragmentation and disk accretion (Elmegreen, 1999), the ejection of stellar embryos (Reipurth & Clarke, 2001) from multiple systems and the formation in circumstellar disks like giant planets. The presence of disks and their properties are crucial in distinguishing between the various scenarios: a truncated disk (size of a few AU) would support the ejected stellar embryo hypothesis, a non-truncated one is the sign of stellar-like accretion, while BDs formed like planets should have no dust around them.

In the case of BDs, NIR data are not necessarily a good tracer of disk emission because they are strongly affected by molecular bands of the cool BD atmosphere. Since the emission of warm (100 - 400 K) circumstellar dust peaks around 10 μm, mid-infrared (MIR) excess emission – arising from dust grains close to the star – is the best tool to search for circumstellar disks. The MIR regime is best accessed by space-born telescopes, the last of which was the Infrared Space Observatory (ISO), operating between 1995 - 1998. However, the majority of BDs has been discovered too late to be targeted by ISO.

Up to now, only few BDs with MIR excess are known. These objects, identified in the ISOCAM archive, are located in the Cha I or in the ρ Ophiuchi star-forming regions (Persi et al., 2000; Comerón et al., 1998). Their substellar nature has been deduced from comparing NIR and optical measurements to evolutionary models (Comerón et al., 1998, 2000).

Natta & Testi (2001) proposed a model based on scaled-down disks around pre-main-sequence stars to explain the measured spectral energy distributions (SEDs).

In this paper we present results from our TIMMI2 MIR imaging campaign. Our aim was to detect MIR excess emission and thus to probe the presence of warm circumstellar dust around BDs. We targeted seven very close field BDs of various ages and a young BD candidate in the Cha I star-forming region. Our observations are the first data in the wavelength region of the silicate feature.

2. Observations

We carried out deep MIR observations with the 3.6m/ESO Telescope at La Silla (Chile) using the TIMMI2 camera (Reimann et al., 2000) in 2001 November and December. The targets were seven field BDs and a young BD in the Cha I star-forming region. From the closest field BDs, we selected those which seemed to be the youngest based on their brightness and spectral type.

We used the 9.8 μm filter, where the instrument is the most sensitive, to search for disk emission. In the case of the detected field BD we also complemented the 9.8 μm measurement with 5 and 11.9 μm observations; the BD detected in the Cha I region was also observed at 11.9 μm. We applied long exposure times (typically 2 hrs in each filter) in order to reach the $\sim$10 mJy sensitivity limit of the instrument. Extensive testing of the pointing accuracy shows a typical error not larger than 1.5" towards the Cha I star-forming region. This excludes any confusion with other sources.

3. Results

3.1. Field Brown Dwarfs

Among the seven targeted nearby field BDs, only the object LP 944-20 could be detected. The 3 σ upper limit of the flux density for the other sources is 15 mJy at 9.8 μm. As one of the youngest (475–650 Myr) and closest (5 pc) field BDs (Tinney, 1998), LP 944-20 was the most promising of our targets. Based on its optical spectrum, its spectral type is equal to or later than M9V (Kirkpatrick et al., 1997). Its classification as a BD has been confirmed by the presence of lithium in its photosphere (Tinney, 1998). Excellent atmospheric conditions and a long integration time led to the *first detection of a field BD in the MIR*. The fluxes measured at 5, 9.8 and 11.9 μm are 39 mJy, 24 mJy, and 22 mJy, respectively. These measurements correspond to more than 5 σ detections in each filter. We estimate a photometric error smaller than 15% for each measurement.

3.2. Cha Hα2

In contrast to the older field BDs, we found clear evidence for excess MIR emission in the case of the much younger (2 - 4.5 Myr) BD candidate Cha Hα2. The observed fluxes are 17$\pm$2 and 21$\pm$3 mJy at 9.8 and 11.9 μm, respectively. The object is close to or in the substellar domain, depending on its exact age (Comerón et al., 2000). There is some evidence that Cha Hα2 is actually a close binary with the components in the substellar domain (Neuhäuser et al., 2002).

4. Discussion

4.1. Field Brown Dwarfs

The non-detection of the six field BDs proves the lack of significant amount of warm dust around older field BDs. These data clearly show that the disk dissipation time is below a few 100 Myr, consistent with recent measurements of BDs in the young σ Orionis cluster (Oliveira et al., 2002). Even the detection of the closest target, the 475-650 Myr old LP 944-20, confirms this hypothesis. Compared to a simple blackbody with $T_\star$=2300 K, $R_\star$=0.1 $R_\odot$, D=5 pc (Tinney, 1998), it is clear that our measurements show no MIR excess, but the photospheric flux of the BD itself.

4.2. Disk Models for Cha Hα2

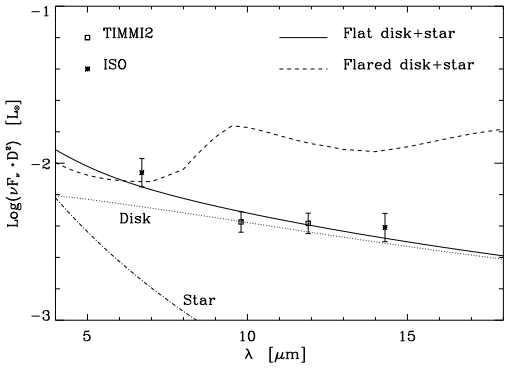

Figure 1: Modelled spectral energy distribution of a flat and a flared disk compared to the observations. Asterisks: ISOCAM measurements at 6.7 and 14.3 μm (20% error bars), while the squares are our TIMMI2 measurements at 9.8 and 11.9 μm (15% error bars).

Modelling the MIR excess emission of Cha Hα2 lead to a surprising result: the SED, plotted in Fig. 1 could be explained by an optically thick, flat disk but not by a T Tauri-like flared one. Fig. 2 shows the schematics of the two different models. A detailed description of the modelling is given in Pascucci et al. (2002).

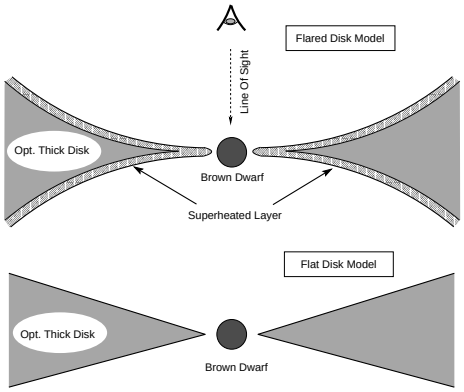

Figure 2: Cross sections of the flared and the flat disk model. The shaded area represents the optically thin superheated layer in the flared disk. This region is the source of the silicate emission feature. The flat disk lacks this disk atmosphere.

5. Summary

Our ground-based measurements represent a new way of probing the properties of disks around BDs, exploring their spectral energy distribution and therefore constraining model prescriptions. We prove the absence of the previously predicted silicate emission feature in the case of the face-on disk around the young BD-candidate Cha Hα2, one of the three known BD-candidates with MIR excess. An optically thick flat disk provides a perfect match to our data. Because no evidence for disks around older field BDs could be detected, disk dissipation times must be shorter than a few 100 Myr. Our results suggest that newborn BDs have disks like young, low-mass stars, but also indicate unexpected differences in their disk geometry. A detailed description of this work can be found in Apai et al. (2002).

References

Apai, D., Pascucci, I., Henning, Th., Sterzik, M. F., Klein, R., Dimitri, S., Günther, E., Stecklum, B., ApJ 573, L115

Basri, G., 2000, ARA&A 38, 485

Comerón, F., Rieke, G. H., Claes, P., Torra, J., Laureijs, R. J., 1998, A&A 335, 522

Comerón, F., Neuhäuser, R., Kaas, A.A., 2000, A&A 359, 269

Elmegreen, B.G., 1999, ApJ, 522, 915

Kirkpatrick, J.D., Henry, T.J., Irwin, M.J., 1997, AJ 113, 1421

Kumar, S.S., 1963, ApJ 137, 1121

Nakajima, T., Oppenheimer, B.R., Kulkarni, S.R., Golimowski, D.A., Matthews, K., Durrance, S.T., 1995, Nature 378, 463

Natta, A., Testi, L., 2001, A&A 376, L22

Neuhäuser, R., Brandner, W., Alves, J., Joergens, V., Comerón, F., 2002, A&A 384, 999

Oliveira, J.M., Jeffries, R.D., Kenyon, M.J., Thompson, S.A., Naylor, T. 2002, A&A 382, L22

Pascucci, I., Apai, D., Semenov, D., Henning, Th., 2003, Comm. Konkoly Obs. 103, proc. of the conf. "Interaction of Stars with their Environment II.", eds. Cs. Kiss et al., p.99

Persi, P., Marenzi, A.R., Olofsson, G., et al., 2000, ApJ 357, 219

Reipurth, G., Clarke, C., 2001, AJ 122, 432

Reimann, H.-G., Linz, H., Wagner, R., Relke, H., Kaeufl, H. U., Dietzsch, E., Sperl, M., Hron, J., 2000, in: "Optical and IR Telescope Instrumentation and Detectors", eds. M. Iye & A.F. Moorwood, ESO, Vol. 4008, 1132

Tinney, C.C. 1998, MNRAS 296, L42

Metamorphosis of a BD Disk: Flared Becomes Flat

I. Pascucci[1,2], D. Apai[1,2], Th. Henning[1,2], D. Semenov[2]

[1] Max Planck Institute for Astronomy
Königstuhl 17, Heidelberg, D-69117 Germany
[2] Astrophysical Inst. and University Obs. Jena
Schillergässchen 2-3, D-07745 Jena, Germany
E-mail:[1] pascucci@mpia-hd.mpg.de

Abstract

We conducted mid-infrared observations of the brown dwarf candidate Cha Hα2. We find that the predicted silicate feature does not appear in its spectral energy distribution (SED). In order to interpret the lack of this feature, we carried out analytical calculations adopting both flared and flat disk geometries. We show that, independently of the chosen parameter set and chemical composition, the flared disk model cannot explain the measured fluxes. On the contrary, the SED emerging from a flat disk fits well the observations.

Keywords: *accretion, accretion disks – circumstellar matter – stars: individual (Chamaeleon Hα2) – stars:low mass, brown dwarfs*

1. The importance of Brown Dwarf disks

Brown Dwarfs (BDs) occupy the substellar mass domain. Having masses lower than 75 M_{Jup}, they are unable to burn hydrogen steadily. In spite of the rapidly growing number of known BDs (Basri, 2000), we do not know if they form like planets or like stars. Proposed scenarios include:

▷ star-like formation via fragmentation and disk accretion (Elmegreen, 1999)
▷ ejection of stellar embryos from multiple systems (Reipurth & Clarke, 2001)
▷ formation in circumstellar disks like giant planets.

The presence of disks and their properties are crucial in distinguishing between the various scenarios: a truncated disk (size of a few AU) would support the ejected stellar embryo hypothesis, a non-truncated one is the sign of stellar-like accretion, while BDs formed like planets should have no dust around them.

Since the emission of warm (100 - 400 K) circumstellar dust peaks around 10 μm, mid-infrared (MIR) excess emission - arising from dust grains close to the star - is the best tool to search for circumstellar disks. Up to now, only few BD candidates with MIR excess have been identified in the ISO archive, all of

them located in the Cha I star-forming region (Persi et al., 2000). Their spectral energy distribution (SED) have been interpreted by Natta & Testi (2001) using a model based on scaled-down disks around pre-main-sequence stars. They followed the Chiang & Goldreich disk geometry which has been rather successful in describing SEDs of T Tauri and Herbig Ae/Be stars (Chiang & Goldreich, 1997).

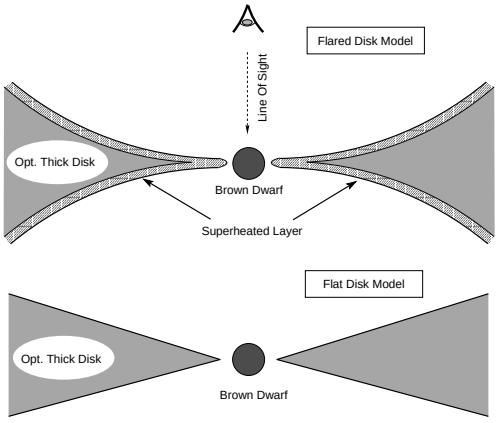

Figure 1: Cross sections of the flared and the flat disk model. The shaded area represents the optically thin superheated layer in the flared disk. This region is the source of the silicate emission feature. The flat disk lacks this disk atmosphere.

2. The flared disk model

The main assumption of the Chiang & Goldreich model is the flaring of the disk, which introduces a superheated surface layer, called the disk atmosphere (see Fig. 1). The major components of this model are: the star, the optically thin disk atmosphere and the optically thick disk interior. In the MIR the stellar radiation is well approximated by a black body, while the optically thick disk emission is given by a power law $F_\nu \propto \lambda^{5/3}$. A simple analytical formula (Natta et al., 2000) is used to describe the optically thin disk atmosphere, which is producing a strong silicate emission around 9.6 μm (Si-O stretching mode).

3. Towards the flat disk model

We observed the BD candidate Cha Hα2 at 9.8 and 11.9 μm using the TIMMI2 camera at the 3.6m/ESO Telescope at La Silla, Chile. Since we find the same

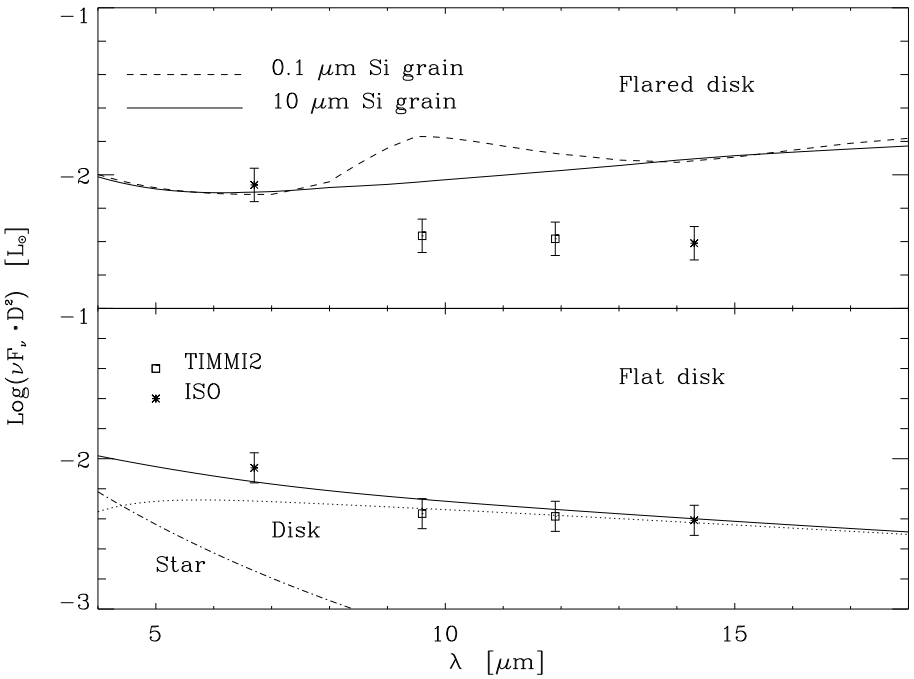

Figure 2: Upper panel: Modelled SED of a flared disk using two different silicate grain sizes. The silicate feature appears in emission for small 0.1 μm grains. The squares and the stars are measurements from TIMMI2 and ISO. Lower panel: Best fit model for an optically thick flat disk. The parameters of the model are as follows: D= 160 pc, $T_\star$ = 2550 K, $M_\star$ = 0.08 $M_\odot$, $L_\star$ = 0.035 $L_\odot$, R_{in} = 4.5 $R_\star$, R_{out} = 100 AU.

flux densities at the peak and on the wing of the feature, we exclude the presence of any silicate feature. This contradicts the prediction of Natta & Testi (Natta & Testi, 2001). We find that changing the disk geometry (inner and outer radii, scale height, inclination) is insufficient to fit the flared model. Altering the optical properties (or composition) of the dust grains has a stronger effect: the absence of the silicate feature could be explained by the lack of this dust component or the presence of large grains (radii larger than 5 μm). However, we stress that the power law continuum, predicted by the flared model, does not fit our data.

A much simpler and more straightforward solution is the assumption that

the BD is surrounded by an optically thick flat disk. We assume a power law disk with a surface density of $\Sigma \propto R^{-3/2}$ and a temperature of $T \propto R^{-3/4}$, typical of reprocessing and viscous disks (Shu, 1990). Since this disk is entirely optically thick, its SED is independent of the dust properties. The model does not show any feature. The continuum of a power-law flat disk has the observed slope. In Fig. 2 we compare the measurements with model predictions.

4. Conclusion

We prove that the lack of the silicate feature in the SED of the BD candidate Cha Hα2 cannot be explained by a T Tauri-like flared disk geometry. Our calculations show that an optically thick flat disk model reproduces the observations.

References

Basri, G., 2000, ARA&A 38, 485
Chiang, E.I., Goldreich, P., 1997, ApJ 490, 368
Elmegreen, B. G., 1999, ApJ 522, 915
Natta, A., Meyer, Michael R., Beckwith, Steven V. W., 2000, ApJ 534, 838
Natta, A., Testi, L., 2001, A&A 376, L22
Persi, P., Marenzi, A.R., Olofsson, G., et al., 2000, A&A 357, 219
Reipurth, B., Clarke, C., 2001, AJ 122, 432
Shu, F. H., 1990 in The Physics of Star Formation (Kluwer)

The Influence of External UV Radiation on the Evolution of Protostellar Disks

S. Richling[1], H.W. Yorke[2]

[1]Institute for Theoretical Astrophysics
University of Heidelberg, Tiergartenstr. 15, D-69121 Heidelberg
E-mail: richling@ita.uni-heidelberg.de
[2]Jet Propulsion Laboratory, California Institute of Technology
MS 169-506, 4800 Oak Grove Drive, Pasadena, CA 91109
E-mail: Harold.Yorke@jpl.nasa.gov

Abstract

We investigate the interaction of an external UV radiation field with protostellar disks of low-mass stars using 2D radiation hydrodynamical simulations. The disks are gradually destroyed via photoevaporation as the UV photons heat the gas in the outer layers of a disk to thermal escape velocities. Beside the UV flux and the luminosity of the stellar wind from the central star, the evolutionary state of the star-disk system at the onset of the external illumination determines the size and the form of the ionized envelope and the resulting spectral appearance of the object. Disks irradiated before one free-fall time after the collapse of the parental molecular cloud lose much of the associated material during the first 10^4 yr of evolution. The star-disk systems remain extremely small in comparison to star-disk systems first irradiated at later evolutionary phases, where the central objects are more massive and much of the clouds mass is already bound in the accretion disk. These results suggest that an early UV illumination favors the formation of low-mass cluster members.
Keywords: *circumstellar matter – hydrodynamics – HII regions – line: formation – radiative transfer – stars: formation*

1. Numerical Methods

We follow the evolution of protostellar disks under the influence of an external radiation field (Fig. 1.) by means of a 2D radiation hydrodynamics code. The code assumes axial symmetry and solves the hydrodynamical equations on nested grids (Yorke & Kaisig, 1995). The transfer of direct UV photons is calculated along lines of sight centered at the star located outside the computational domain. Diffuse UV photons originating from the recombination of hydrogen into the ground state and from scattering on dust grains are treated with the

flux-limited diffusion approximation. Simultaneously, we determine the ionization of hydrogen and carbon. A detailed description of the code is given in Richling & Yorke (1998, 2000).

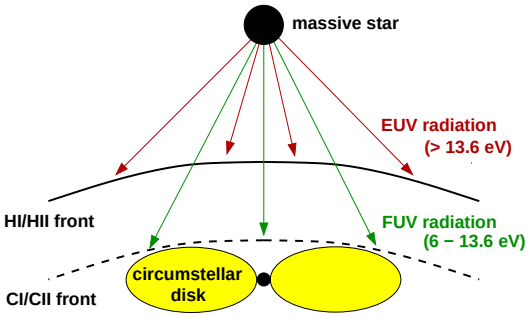

Figure 1: The ionizing radiation of a massive star interacts with a protostellar disk nearby. Both UV components are important.

In a second step, we use the density and temperature distribution of the gas and the velocity field obtained with the hydrocode to calculate emission line maps, continuum maps and spectral energy distributions via a ray-tracing procedure (Kessel et al., 1997). These diagnostic radiative transfer calculations allow us a direct comparison with observations.

2. Ionized Envelope and Micro-Jets

The calculations start with star-disk systems resulting from collapse simulations (Yorke & Bodenheimer, 1999). After the initial launch of a neutral disk wind by FUV photons, the carbon ionization front envelopes the densest parts of the disk. The hydrogen ionization front is prevented from reaching the disk surface by the interaction with the neutral wind and finally forms an envelope with the typical head-tail structure (Fig. 2a). This structure is the natural outcome of our self-consistent simulations and its properties are comparable to the proplyds observed in the Orion Nebula. The size of the ionized envelope and the photoevaporation rate of the disk depend on the distance from the ionizing star. Disks exposed to a UV radiation field are expected to survive no longer than several 10^5 years (Hollenbach et al., 2000; Richling & Yorke, 2000).

If we consider an isotropic stellar wind emerging from the protostar within the disk, we are able to reproduce another feature of proplyds. The spherically symmetric stellar wind is hydrodynamically focused into a jet due to the pressure of the neutral disk wind. The opening angle of the counter-jet is wider, because the neutral wind on this side of the disk shadowed from direct UV photons is

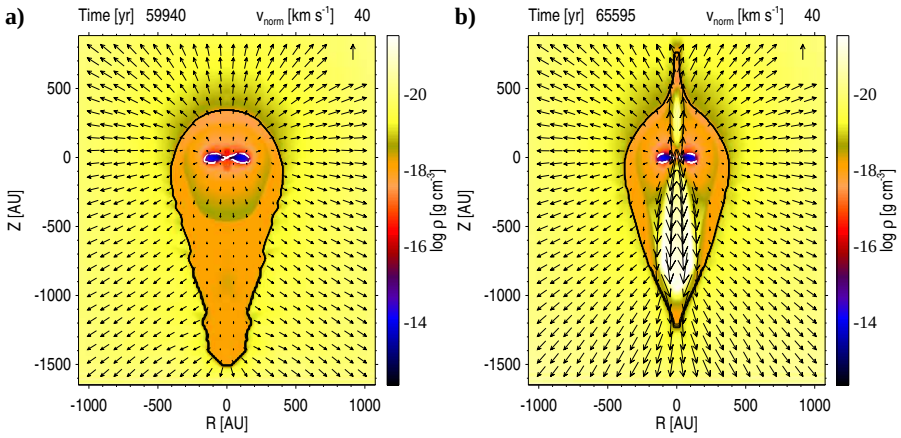

Figure 2: Density distribution, velocity field (arrows), hydrogen ionization front (black contour lines) and carbon ionization front (white contour lines) of a protostellar disk illuminated by an external UV radiation field. a) without a stellar wind b) with an isotropic stellar wind of 100 km/s.

less powerful. The jet changes the form of the ionized envelope as shown in Fig. 2b. In the corresponding emission line maps, the finger in the ionization front appears as a spike emerging from the objects head resembling the micro-jets extending from several proplyds in the Orion Nebula (Fig. 3).

3. The Evolutionary State of the Protostellar Disk

Table 1: Starting models: Elapsed time t since the beginning of collapse, disk radius $r_{\rm d}$ and mass of the protostar $M_\star$ are given.

Model	$t/10^3\,{\rm yr}$	$t/t_{\rm ff}$	$r_{\rm d}/{\rm AU}$	$M_\star/M_\odot$
Y	107	0.5	130	0.64
M	240	1.2	640	0.94
O	438	2.2	1700	1.14

Massive stars evolve relatively fast and reach the main-sequence when low-mass cluster members may still be in earlier phases of evolution. In order to investigate the effect of UV illumination during earlier phases of a protostellar collapse we used three star-disk models at different evolutionary phases all

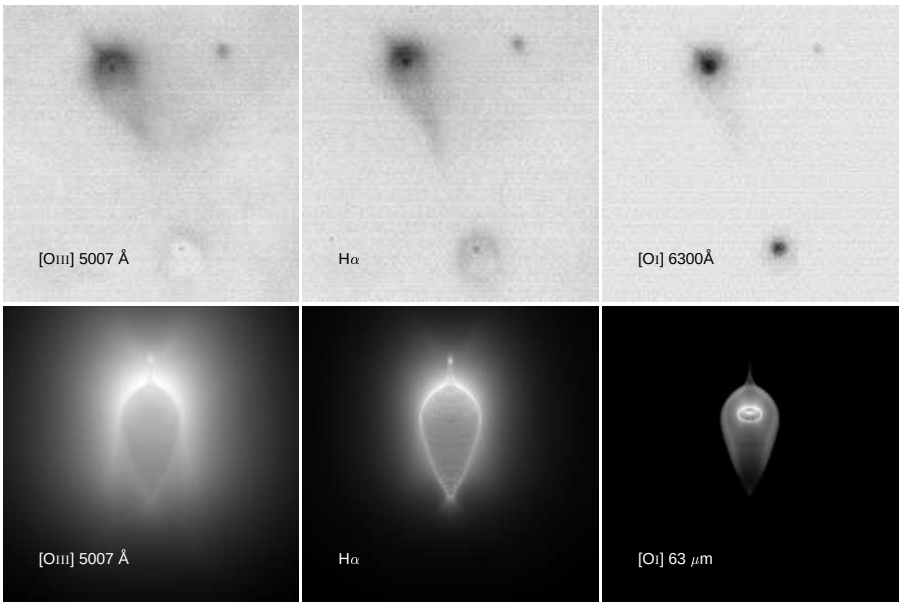

Figure 3: First row: Observed emission line maps of the proplyd HST 2 in M42 (Bally et al., 1998, Fig. 7a). Second row: Calculated emission line maps of the numerical result shown in Fig. 2b. The length of the object is $\sim$ 1500 AU which is about twice as large as HST 2.

resulting from a single collapse simulation of a 2 $M_\odot$ rotating molecular cloud (Table 1).

Fig. 4 shows continuum maps of the three models after 5×10^4 yr of external UV illumination. In the first row are 2 cm radio maps of the whole object. They trace the free-free emission of the dense ionized gas around the head-tail envelope. In the second row are 100 μm maps of an inner part of the domain as indicated in the radio maps. They show the dust emission of the disk itself. The evolution of the mass and the radius of the disk are shown in Fig. 5.

Model Y is younger than one free-fall time of the parental molecular cloud core. Most of the material in its environment is ionized and swept away with the ionized wind during the first 10^4 yr of the evolution. Only a small object remains which will be photoevaporated relatively quickly. The older the starting model the larger is the ionized envelope and the length of the tail. Since the

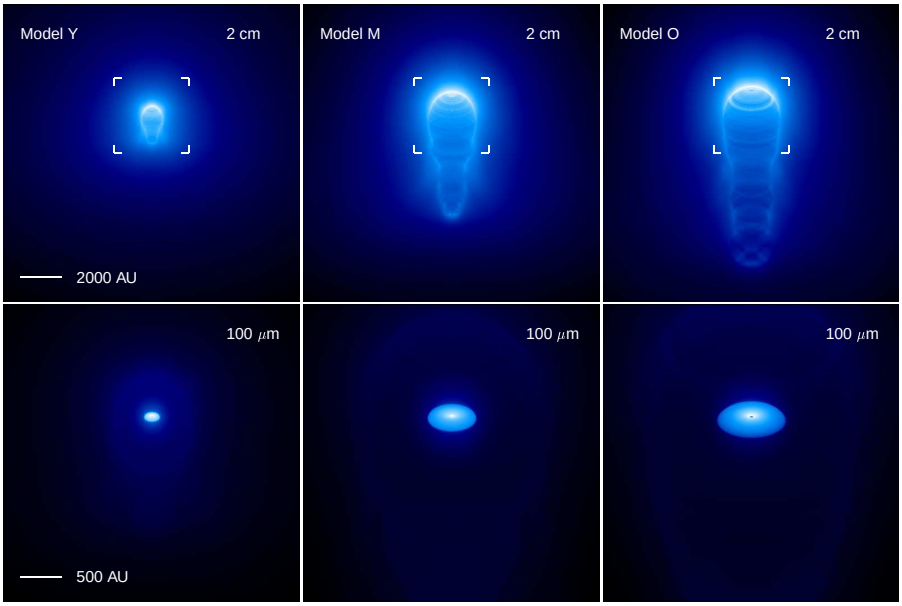

Figure 4: Continuum maps of the models Y, M and O (see Table 1) after 5×10^4yr of external UV illumination.

photoevaporation rate depends on the surface of the disk, model M will survive longer than model O because model O has a larger disk radius during the first 10^5 yr of evolution.

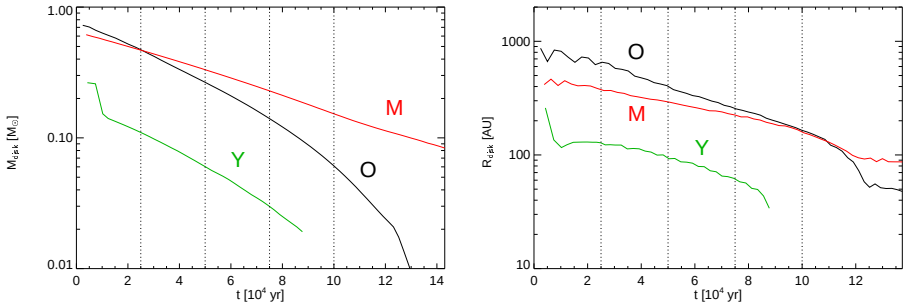

Figure 5: Evolution of mass and radius of the disk.

4. Conclusions

The photoevaporating disk model can explain the observed features of proplyds, e.g. the head-tail structure, the stand-off of the ionization front and the appearance of micro-jets. Photoevaporation is an important disk dispersal mechanism with a time scale of several 10^5 yr which is an upper limit for the time available for planet formation.

The evolutionary state of the protostellar disk at the time when the external UV illumination begins also determines the size and the spectral appearance of the resulting object. UV irradiation during early phases of a protostellar collapse removes the material that otherwise would be accreted onto the disk and finally onto the protostar itself. Thus, an early UV illumination favors the formation of low-mass cluster members and possibly is a mechanism for brown dwarf and brown dwarf disk formation.

Acknowledgements

This work is supported by the Deutsche Forschungsgemeinschaft and by the National Aeronautics and Space Administration (NASA) under grant NRA-99-01-ATP-065. Portions of this research were conducted at Jet Propulsion Laboratory, California Institute of Technology.

References

Bally, J., Sutherland, R.S., Devine, D., Johnstone, D., 1998, AJ 116, 293
Hollenbach, D., Yorke, H.W., Johnstone, D., 2000, in: Protostars & Planets IV, eds. V. Mannings, et al., University of Arizona Press, Tucson, p.401
Kessel, O., Yorke, H.W., Richling, S., 1998, A&A 337, 882
Richling, S., Yorke, H.W., 1998, A&A 340, 508
Richling, S., Yorke, H.W., 2000, ApJ 539, 258
Yorke, H.W., Bodenheimer, P., 1999, ApJ 525, 330
Yorke, H.W., Kaisig, M., 1995, Comp. Phys. Comm. 89, 29

ISO Observations of the Infrared Continuum of the Herbig Ae/Be Stars

D. Elia, F. Strafella, L. Campeggio

Dipartimento di Fisica - Università di Lecce
Via per Arnesano C.P. 193 I-73100 Lecce - Italy
E-mail:[1]eliad@le.infn.it

Abstract

We present a study of the whole sample of the Herbig Ae/Be stars observed with the spectrometers on board of the Infrared Space Observatory (ISO/ESA). These objects have been studied not only by means of their infrared continuum emission but also with respect to all the available photometric data, collected from the optical region to the radio wavelengths. The global spectral energy distributions (SEDs) have been compared with the results of radiative transfer calculations, that have been made in the framework of a circumstellar (CS) model. The results of the selection of the best models allow us to infer on the relationship between the geometry of the CS matter distribution and the evolutionary stage of these objects.
Keywords: *stars: pre-main sequence – circumstellar matter – infrared: stars*

1. Observations, data reduction and results

The ISO data archive has been searched for Short Wavelength Spectrometer (SWS) and Long Wavelength Spectrometer (LWS) observations related to Herbig AeBe stars (HAeBe stars hereinafter). We found 36 objects (out of 108 stars recognized in Thé et al. (1994)), which are listed in Table 1.

Table 1: The observed sample of HAeBe stars

LkHα 198	Z CMa	He 3-1191	WW Vul
V376 Cas	HD 97048	HD 150193	BD +40°4124
Elias 3-1	HD 100546	CoD -42°11721	LkHα 224
AB Aur	HD 104237	HD 163296	PV Cep
MWC 480	IRAS 12496-7650	MWC 297	HD 200775
HD 34282	HD 141569	MWC 300	V645 Cyg
HD 36112	HD 142666	TY CrA	LkHα 234
CQ Tau	HD 144432	R CrA	LkHα 233
MWC 137	HR 5999	HD 179218	MWC 1080

The SWS spectra we discuss here were taken in the range 2.3–45 μm with low resolution ($\lambda/\Delta\lambda \sim 250$) and a typical field of view increasing with wavelength from $14'' \times 20''$ to $20'' \times 33''$ (De Graauw et al., 1996), while the LWS spectra were obtained in the range 43–196.7 μm, $\lambda/\Delta\lambda \sim 200$, (Clegg et al., 1996). In the LWS spectral range the instrumental beam size is $\sim 80''$ so that in some cases (12 objects) the observations were carried out also at an off-source position to account for the contamination due to the local background.

The raw SWS and LWS data were processed using version 10 of the off-line pipeline, which produced series of repeated spectral scans, each composed of 12 and 10 subspectra for SWS and LWS, respectively. These correspond to different spectral ranges, that are arranged to be partially overlapping. The data were further reduced and analysed in subsequent steps:

- removing bad points (glitches, residual detectors responsivity drifts);
- averaging of the many scans obtained on each subspectrum;
- removing of the low-frequency fringes, whose presence affects particularly the LWS spectra (Swinyard et al., 1998).
- smoothing of averaged spectra (SWS only).

Whenever possible, the off-source LWS spectra were subtracted from the corresponding on-source data. Notwithstanding accurate data reduction, the subspectra obtained appear in many cases not perfectly overlapping together, probably because of the variation of the beam size with the wavelength (De Graauw et al., 1996; Swinyard et al., 1998). In Fig. 1. we show examples of two reduced source spectra.

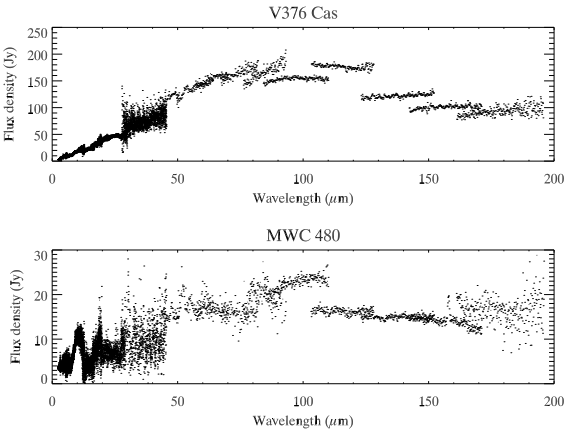

Figure 1: ISO spectra. Both sources show a good continuity between SWS and LWS fluxes despite the different beamsizes involved. On the other hand they clearly present discontinuities in the LWS respective subspectra.

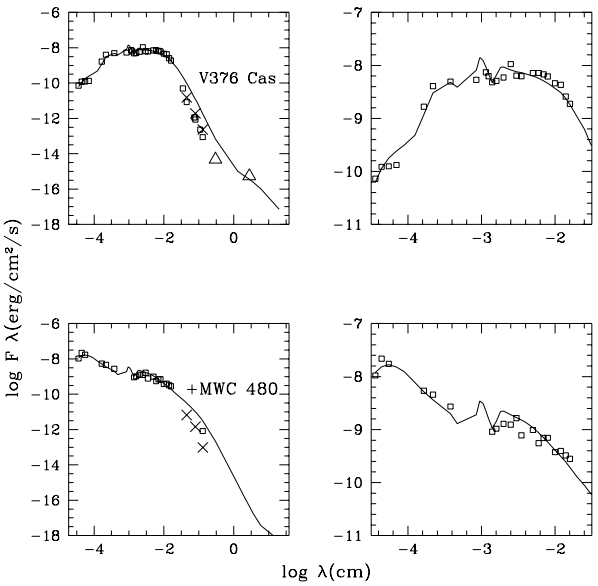

Figure 2: Spectral fits. Computed SEDs (solid line) are superimposed on the observed fluxes (circles, triangles are upper limits). Crosses represent submillimetric model fluxes corrected for diffraction effects due to the instrumental beamsize.

2. Model calculation and comparison with observations

The SEDs emerging from CS envelopes have been computed by means of a model based on a spherical geometry of the circumstellar environment. The model is characterized by a density distribution $n(r)$ around a central star and by the presence of an HII region whose radius is determined by the ionizing luminosity of the central star. A temperature profile $T(r)$ is also considered for the dust component while for the gas we assumed $T = 10^4$ K in the HII region. The gas emission processes considered in the radiation transfer are: free-free, free-bound and electron scattering, while for the dust component the emissivity is computed on the basis of the "astronomical silicate" defined by Draine & Lee (1984). Cases with a modified dust emissivity (at $\lambda > 20\mu$m) have also been computed to take into account the fact that in star forming regions the average dust grain size can be larger than in the diffuse IS medium and consequently the opacity can be described by a $k \propto \lambda^{-\beta}$ law; in our case, $\beta = 1.2$, 0.8, 0.6 (see Pezzuto et al. (1997) for a more complete model description). In addition we also consider:

1) the possible presence of cavities in the CS envelope as can be evacuated by the strong stellar wind associated with the PMS phases;

2) the possibility of two different density distributions describing the inner and outer parts of the envelope, respectively.

A large set of synthetic spectra has been computed; for each object we searched for the best fit with the observed fluxes. Such a comparison, made by means of a "chi square like" method, allows the selection of the best models for each object. In doing this we considered not only the spectral fit but also the consistency of the model fluxes with the spectral type estimated for the star, the distance, and the observed visual absorption. An example of the results obtained is presented in Table 2. and shown in Figure 1..

Table 2: Fit parameters and correspondent observables

Source	β	q	p	n_0	Spectral type		A_V (mag)			Distance (pc)	
				(cm^{-3})	Calc.	Obs.	CS	IS	Obs.	Calc.	Obs.
V376 Cas	1.2	0.5	0.8	$3{\cdot}10^8$	B5	B5 (1)	4	2.5	2.9-5.2 (3,4)	724±32	600 (3)
MWC 480	0.6	0.6	1.3	$3{\cdot}10^{10}$	A3	A3 (2)	1	0	0.25-0.4 (5,6)	101±5	131 (5)

NOTES: V376 Cas was fitted with a simple spherical model, MWC 480 with a model considering also two polar cavities.
REFERENCES TO THE TABLE: 1. Herbig & Bell (1988); 2. Jaschek et al. (1991); 3. Hillenbrand et al. (1992); 4. Pezzuto et al. (1997); 5. van den Ancker et al. (1998); 6. Miroshnichenko et al. (1999).

References

Clegg, P.E., Ade, P.A.R., Armand, C., et al., 1996, A&A 315, L38
De Graauw, T., Haser, L.N., Beintema, D.A., et al., 1996, A&A 315, L49
Draine, B.T., Lee, H.M., 1984, ApJ 285, 89
Herbig, G.H., & Bell, K.R., 1988, Lick Obs. Bull., 1111
Hillenbrand, L.A., Strom, S.E, Vrba, F.J., Keene, J., 1992, ApJ 397, 613
Jaschek, M., Jaschek, C., Andrillat, Y., 1991, A&A 250, 127
Miroshnichenko, A., Ivezić , Z., Vinković, D., & Elitzur, M., 1999, ApJ, 520, L115
Pezzuto, S., Strafella, F., Lorenzetti, D., 1997, ApJ 485, 290
Swinyard, B.M., Burgdorf, M.J., Clegg, P.E., Davis, G.R., Griffin, M.J., Gry, C., Leeks, S.J., Lim, T.L., Pezzuto, S., Tommasi, E., 1998. In: Proc. SPIE, A.M. Fowler (Ed.), Vol. 3354, p.888
Thé, P.S., de Winter, D., Pérez, M.R., 1994, A&AS 104, 315
van den Ancker, M.E., de Winter, D., Tjin A Djie, H.R.E., 1998, A&A 330, 145

(Post-)Main-Sequence Stars

Cepheid Variables and the Circum/Interstellar Matter

L. Szabados
Konkoly Observatory
H-1525 Budapest XII, P.O.Box 67., Hungary
E-mail: szabados@konkoly.hu

Abstract

Various aspects of the relation of classical Cepheids and inter- and circumstellar matter are summarized. Emphasis is given to the question of mass loss from Cepheids and to the role of these pulsating variables in revealing the recent star formation history in their neighbourhood.
Keywords: *Cepheids, reflection nebulae, Stars: chromospheres*

1. Introduction

Classical Cepheids are fundamental objects in astronomy. Being regular radial pulsators, a number of relationships exist between their physical and phenomenological properties. One of them, the period-luminosity (P-L) relationship is instrumental in establishing the cosmic distance scale. In addition to their cosmological role as primary distance indicators, Cepheids serve as astrophysical laboratories for studying structure of post-main sequence stars, hydrodynamics of stellar atmosphere of supergiants, and for checking evolutionary model calculations.

Since Cepheids fall into the mass range of 4-12 $M_{\odot}$, their evolution is rather fast. When they enter the instability strip of the HR diagram and perform radial oscillations, they are old enough that no close connection with the remnants of the star forming cloud is expected, but still too young that mass loss characteristic of late stages of stellar evolution can be expected. Study of mass loss is, however, an interesting topic of Cepheid research for various aspects:
– The circumstellar matter results in reddening and dimming the brightness of the Cepheid, therefore a due extinction correction has to be applied when determining the absolute magnitude of the individual Cepheids.
– The effect of pulsation on the outer region and the atmospheric structure also deserves study. The question is whether the structure of the pulsating atmosphere is different from that of non-pulsating stars located at the same point of the HR diagram.
– Cepheids are unique objects in the sense that their mass can be determined

by various methods, each of them being independent of the others. When comparing the mass predicted by the stellar evolution theory with the mass values determined from various characteristics of stellar pulsation, the evolutionary masses used to be notoriously and significantly larger than the others implying a major mass loss before and/or during the Cepheid phase of evolution (see Cox (1980) for a review). This discrepancy was finally resolved when the new radiative opacities were calculated (Rogers & Iglesias, 1992), but the mass loss from the pulsating atmosphere has remained an important and unsolved issue.

2. Mass loss from Cepheids – multiwaveband studies

According to the theoretical calculations pulsation may result in significant mass loss for Cepheids, predicting mass-loss rates 7×10^{-9} and 2×10^{-7} $M_\odot$ yr^{-1} , for 5 and 7 $M_\odot$ stars respectively (Willson, 1988). Moreover, Willson & Bowen (1984) pointed out that while the star is in the Cepheid phase, mass loss could prolong its lifetime within the instability strip by as much as 5-50 times.

Is there any evidence of mass loss during or prior to the Cepheid phase? The most convincing evidence for mass loss would be the direct detection of the escaped matter. Assuming Pop. I chemical composition, about 1-2% of the mass should be in a form of heavy elements which can form dust grains. These grains could be detected in the IR-region. Several Cepheids show modest mid-IR excess, mainly at 25 μm which could arise from dust with temperatures near 150 K. For these stars the IR excesses are consistent with mass-loss rates of $10^{-8} - 10^{-9} M_\odot$ yr^{-1}, which is really a very low value (McAlary & Welch, 1986). The analysis of the IRAS data also showed that the infrared excess is independent of the pulsation period. This implies that the mass-loss process is largely independent of the size or effective temperature of the Cepheid.

If the outflowing material is hot enough, the ionized matter can be detected by observing its radio emission. VLA observations of 5 very bright Cepheids gave no positive detection at 5 GHz, only resulted in upper limits of the radio radiation, from which upper limits for the ionized mass-loss rates could be derived (Welch & Duric, 1988). These upper limits are an order of magnitude smaller than the calculated values. If Cepheids are indeed losing mass at a rate as high as predicted theoretically, the material must not be ionized.

In addition to the presence of infrared excess, stellar wind may be observed by blueshifted absorption features in lines such as Hα, Ca II H&K and Mg II h&k. The broad emissions of the Mg II resonance lines are particularly sensitive indicators of circumstellar absorption. IUE long-wavelength spectra provide suffi-

ciently high resolution in the 2800 Å region to be able to resolve discrete absorption components. Unfortunately, there are only five classical Cepheids bright enough that could be observed by the IUE in high resolution mode (Schmidt & Parsons, 1984a). The profile of the Mg II h&k line of ζ Geminorum shows two distinct high-velocity blueshifted components near the surface escape velocity which persists for most of the pulsation cycle (Deasy, 1988). The UV spectrum of the 35-day Cepheid l Carinae indicates a mass outflow whose velocity exceeds the escape velocity at the surface. Deasy calculated a mass-loss rate of about $10^{-10}\,M_{\odot}\,\mathrm{yr}^{-1}$ for ζ Gem, and 3 times larger value for l Car.

3. Chromospheric emission in Cepheids

It is an obvious task to search for possible differences between the outer regions of pulsating and stable stars appearing at the same location of the H-R diagram.

As to the chromosphere, the question is whether the observable emission is due to a solar type chromosphere or it is caused by a pulsational shock that propagates through the upper atmosphere of the Cepheid. Shock-induced emission is expected during and just after the brightness maximum because this is the phase when the shock reaches the outer layers of the stellar atmosphere. In the case of a solar type chromosphere the heating is due to some mechanical flux originating in the convection zone, therefore the emission of this origin is more probable during the coolest phases of the pulsational cycle.

The profiles of the Mg II lines in solar-temperature stars are complex and composed of several components. The high-resolution IUE-spectra of Cepheids often show double emission features separated by the circumstellar absorption component (Schmidt & Parsons, 1982, 1984a,b). The general trend in the temporal variation of the total flux of h and k lines is that Mg II turns on rather suddenly and then declines during most of the cycle. The fact that some Mg II absorption components move differently from the photosphere supports the view that they originate at least several tenths of a stellar radius above it. The chromosphere of Cepheids is heterogeneous over the stellar surface and is likely composed of a number of rising and falling columns. The available data are, however, insufficient to decide whether the chromospheric activity is the result of internal convection or it is caused by a shock generated by the pulsation. In any case, for some Cepheids blueshifted chromospheric UV-lines have been observed (Schmidt & Parsons, 1984a) indicating velocities exceeding the surface escape velocity (about 100 km/s).

Hot corona can be studied by X-ray observations. At the sensitivity level of

Einstein, no X-ray emission was detected from three bright Cepheids, δ Cephei, β Dor, and ζ Gem (Böhm-Vitense & Parsons, 1983). A decade later, ζ Gem was reobserved with the more sensitive equipment on board of ROSAT (Sasselov, 1994). No X-ray flux was detected at the upper limit five times lower than previously observed, indicating that classical Cepheids do not have any hot plasma in their upper atmosphere. This means that chromospheric heating is possible in the Cepheid atmospheres but the global envelope pulsation inhibits coronal heating.

4. Cepheids in reflection nebulae

Two classical Cepheids – RS Puppis and SU Cassiopeiae – are connected with reflection nebulae (van den Bergh, 1966). RS Pup is embedded centrally in such a nebula while SU Cas is displaced from the neighbouring nebula but the Cepheid together with some other field stars illuminate the dust particles in their vicinity. These two Cepheids are particularly important because the embedding or nearby reflection nebula offers an independent means for determining their distance, therefore the P-L relation can be calibrated.

A thorough investigation of the region around SU Cas revealed additional reflection nebulae near this Cepheid and from the study of the stars in this region a loose association was discovered (Turner & Evans, 1984). The core group members are at a distance of 258 ± 3 pc and have ages of about 120 million years. The derived luminosity for SU Cas is in agreement with the luminosity obtained from the P-L relation assuming fundamental mode pulsation. It is intriguing, however, that the trigonometric parallax determined from the Hipparcos data places SU Cas at a distance of 433 pc (but the uncertainty is about 100 pc). Moreover, from their Baade-Wesselink analysis, Milone et al. (1999) concluded that SU Cas is pulsating in the first overtone mode.

The reflection nebula surrounding RS Puppis is circularly symmetric around the centrally placed Cepheid. The nebular arcs in these concentric ring structures are higher density regions of reflecting material. In his pioneering study, Havlen (1972) searched for and was able to point out the brightness variations of several nebular features due to the light echo corresponding to the 41.4 day periodicity of the stellar pulsation. The nebulosity varies with the same period as the Cepheid but with a phase delay, owing to the finite light travel time across the nebulosity. It should be emphasized that his study was based on photographic observations, and in spite of the limited accuracy and sensitivity, Havlen could follow the effect of the light echo of the Cepheid on the brightness

of the dust cloud.

The phase difference between the stellar and the nebular variations depends on the linear dimensions of the nebulosity, and a comparison of the linear and angular sizes allows a geometrical determination of the distance to the Cepheid. It would be high time to repeat this study using CCD detectors which are more sensitive and allow to carry out more precise photometry.

In addition, Mayes et al. (1985) pointed out that significant variability is expected in the surface brightness distribution of the reflection nebulosity at IR wavelengths due to variable heating accompanying the effective temperature changes of RS Pup over a pulsation cycle. This infrared echo of the Cepheid variability in the surrounding nebulosity offers a similar but independent method for distance determination. Unfortunately this method has not been applied in practice in lack of dedicated far-infrared observations of this region.

The discrete rings around RS Pup must reflect the nature of the mass ejection process because it is difficult to explain such structure in terms of continuous mass-loss mechanism. The spacing between the successive rings is fairly regular: about 20,000 AU (Deasy, 1988). This is consistent with the regularly repeating phases of intense mass loss from RS Pup whose mass is about 12 $M_{\odot}$. Havlen (1972), however, pointed out that regularly ejected bubbles contradict the generally accepted stellar evolutionary models.

Later calculations performed by **?** showed that pulsationally driven mass loss – even if it is small – reduces the rate of the period change for all masses. According to their evolutionary models mass loosing Cepheids spend more time in the instability strip. A mass loss rate of $10^{-7} M_{\odot}$/yr results in 2-5 times longer crossing time for a 5 $M_{\odot}$ Cepheid, and the rate of period change decreases by a similar factor. Fernie (1984) compared the observed secular period changes of Cepheids with the theoretical values predicted by the evolutionary models of Becker et al. (1977). The observed changes are consistently smaller than the theoretical values which may be evidence of weak mass loss during the Cepheid phase.

5. Effects of binarity on the behaviour of the Cepheids

Presence of a companion may have important consequences on the circumstellar region around the Cepheid. It is known from the evolutionary models that epizodes of intense mass loss may occur during evolution of binary stars (Hilditch, 2001). The effects of the companion, however, have been usually neglected in the Cepheid research in spite of the fact that more than 60 per cent of the

classical Cepheids belong to binary or multiple system (Szabados, 1995).

For example, it is difficult to separate the free-free emission in the mid-IR produced by the hot chromosphere surrounding a Cepheid from the free-free emission which occurs in binary systems consisting a Cepheid and a hot companion where the emission is generated by the stellar wind in the vicinity of the hot component.

Among the key issues related to Cepheids in binaries one can mention searching for traces of current or pre-Cepheid mass loss. Further important problems, e.g. calibration of the P-L relation, theoretical and observational study of period changes or possible nonradial modes excited by the companion, and search for white dwarf companions are not related to the circumstellar matter.

6. Cepheids as tracers of recent star formation history

Cepheids also serve as indicators of star formation occurred in the recent past. Here I refer to two examples. 1. Evidence of propagating star formation in the Large Magellanic Cloud based on the period distribution of Cepheids. 2. The other example shows how the motion of the interaction point of two spiral arms in M31 can be followed with using Cepheids.

About 1800 Cepheids have been analysed based on the data obtained by the MACHO microlensing experiment (Alcock et al., 1999) by comparing the theoretical and observed period-frequency distributions. The main factors that determine the period distribution of Cepheids in a galaxy are: the star formation rate, the initial mass function, metallicity of the galaxy, stellar evolution prior to and during the Cepheid phase, and the location of the instability strip. Evolutionary tracks indicate when a star of a particular mass will be at a given position in the H-R diagram. Pulsation models give the position of the instability strip, and the pulsation period of the star within the strip.

It has been revealed that a significant burst in star formation occurred one hundred million years ago. During the last 10^8 years the central region of this star formation moved from SE to NW along the bar of the LMC. From the regional period distribution of Cepheids Alcock et al. (1999) concluded that the metal content does not change along the bar of the LMC. They were also able to deduce the time scale of the star formation from the period distributions, they derived the mid-epoch and the duration of the star formation epizodes along the bar.

Taking into account the distance of the LMC (assuming a value of 50 kpc), even the velocity could be calculated at which the star formation peak has been

propagating in the bar. It took about 40 million years to reach the northern end of the bar from the southern one, which can be converted into a velocity of about 100 km/s. This large velocity is an independent evidence supporting the finding that star formation was triggered tidally during the last passage of the LMC close to the Milky Way about 150 million years ago.

The star formation history in the superassociation NGC 206 in the Andromeda nebula was studied by comparing the neutral hydrogen emission map, the location and distribution of blue stars and the Cepheid variables (Magnier et al., 1997). It has been pointed out that NGC 206 is located at the intersection of two spiral arms, suggesting that the interaction between spiral arms is responsible for the enhanced level of star formation. The motion of the interaction point can be followed from the distribution of Cepheids. In that study Cepheids were used as age indicators, based on the relationship: $\log A = 8.4 - 0.6 \log P$, where A is the age of Cepheids in years, P is the pulsation period in days.

It is noteworthy that Cepheids are much more frequent in the regions south of NGC 206 where the number ratio of Cepheids/blue stars exceeds 0.5, while in the bulk of the galaxy the ratio of Cepheids to blue stars (for which $B-V < 0.2$ mag) is smaller than 0.2. These blue stars represent the upper part of the main sequence, where stars with ages younger than 30 million years are found.

This difference in number ratio of Cepheids to blue stars can be explained in terms of a region in which star formation is enhanced. In the southern part of M31 the star formation activity has moved during the past $\sim$100 Myr relative to the spiral arm structure seen today. According to this explanation, NGC 206 represents the most recent phase of the enhanced star formation.

The motion of the enhanced star formation can be calculated from the displacement of the region with amply occurring Cepheids relative to NGC 206 and their age difference. Assuming a typical age of 90 Myr for the bulk of these Cepheids, 30 Myr for NGC 206, and an angular distance of 0.15 degrees between the centers of the two groups of different ages, which corresponds to $\sim$1900 pc at the distance of M31, the relative velocity is about 32 ± 15 km/s.

Acknowledgements

This research has been supported by the Hungarian grants OTKA T029013 and T034584. The author is indebted to Dr. Mária Kun for her remarks leading to a considerable improvement of the paper.

References

Alcock, C., Allsman, R.A., Alves, D.R., et al., 1999, AJ 117, 920
Becker, S.A., Iben, I., Tuggle R.S., 1977, ApJ 218, 633
Böhm-Vitense, E., Parsons, S.B., 1983, ApJ 266, 171
Brunish, W.M., Willson, L.A., 1989, in: "The Use of Pulsating Stars in the Fundamental Problems of Astronomy", Proc. IAU Coll. 111, ed. E.G. Schmidt (Cambridge, CUP), p.252
Cox, A.N., 1980, ARA&A 18, 215
Deasy, H., 1988, MNRAS 231, 673
Evans, N.R., Jiang, J.H., McAlary, C.W., Campins, H., 1993, AJ 106, 726
Fernie, J.D., 1984, in: "Observational Tests of Stellar Evolution Theory", Proc. IAU Symp. 105, eds. A. Maeder & A. Renzini (Dordrecht: Reidel), p.441
Havlen, R.J., 1972, A&A 16, 257
Hilditch, R.W., 2001, An Introduction to Close Binary Stars, Cambridge, CUP
Magnier, E.A., Prins, S., Augusteijn, T., et al., 1997, A&A 326, 442
Mayes, A.J., Evans, A., Bode, M.F., 1985, A&A 142, 48
McAlary, C.W., Welch, D.L., 1986, AJ 91, 1209
Milone, E.F., Wilson, W.J.F., & Volk K. 1999, AJ 118, 3016
Rogers, F.J., Iglesias, C.A. 1992, ApJS 79, 507
Sasselov, D.D., 1994, RMxA&A 29, 215
Schmidt, E.G., Parsons, S.B., 1982, ApJS 48, 185
Schmidt, E.G., Parsons S.B., 1984a, ApJ 279, 202
Schmidt, E.G., Parsons, S.B., 1984b, ApJ 279, 215
Szabados, L. 1995, in: "Astrophysical Applications of Stellar Pulsation", Proc IAU Coll. 155, eds. R.S. Stobie & P.A. Whitelock, ASP Conf. Ser. 83 (San Francisco: ASP), p.357
Turner, D.G., Evans, N.R. 1984, ApJ 283, 254
van den Bergh, S., 1966, AJ 71, 990
Welch, D.L., Duric, N., 1988, AJ 95, 1794
Willson, L.A., 1988, in: "Pulsation and Mass Loss in Stars", eds. R. Stalio & L.A. Willson, Kluwer, p. 285
Willson, L.A., Bowen, G.H., 1984, Nature 312, 429

Spectrophotometric Signature of Circumstellar Matter around 89 Her

L.L. Kiss[1], K. Szatmáry[1], J. Vinkó[2]
[1]Astron. Obs. and Dept. of Experimental Physics, University of Szeged
[2]Dept. of Optics and Quantumelectronics, University of Szeged
H-6720 Szeged, Dóm tér 9, Hungary
E-mail: l.kiss, k.szatmary, vinko@physx.u-szeged.hu

Abstract

The bright supergiant and suspected binary star 89 Herculis is studied with help of infrared and optical spectroscopy. The high-resolution sodium D profiles suggest multiple velocity structure of circumstellar clouds. Astrophysical parameters are derived by fitting model spectra in the infrared region. Our results are in agreement with the recently emerged view of the system based on radio and infrared observations. We also discuss photometric and radial velocity variations concluding that pulsations are barely detectable in velocity data. This behaviour is likely to be caused by the spectral line profile distorsions due to circumstellar envelope.
Keywords: *stars: semiregular stars – stars: individual: 89 Her*

1. Introduction

89 Her = V441 Her = HD 163506 = IRAS 17534+2603 is a bright (V = 5.43 mag) supergiant star of spectral type F2 Ibe. This star shows a light change due to semiregular pulsation (SRd type) with P = 65 d and A $\leq$ 0.1 mag. Both the period and the amplitude of the light curve are unstable. So far there is no widely accepted explanation of the mechanism that drives this variability. As many other supergiant stars, 89 Her has circumstellar dust shells due to episodic mass loss. Changes in these shells with time can presumably be revealed by the average brightness of the star. The photoelectric V light curve was analysed with Fourier and wavelet methods earlier (Szatmáry and Kiss 1997).

The radial velocity practically does not vary with the photometric period, although Percy et al. (2000) found a broad peak in the frequency spectrum at 60-70 days. 89 Her is a spectroscopic binary with P_{orb}=288 d.

According to the commonly accepted view of 89 Her, it is a post-AGB star which evolves to a central star of a planetary nebula. The observed circumstellar envelope proves this scenario. This envelope was ejected a few thousand years ago, although there are some signs (mainly spectroscopic pieces of evidence) that

sudden mass-losses occured in the last few decades too. On the other hand, the physical properties of the star are very uncertain. Neither its mass nor luminosity are known with acceptable accuracy. We obtained near-infrared spectra in the Ca-triplet regime. Fitting the hidrogen Paschen-lines with ATLAS9 models, we have obtained $T_{\rm eff} = 6000$ K and $\log g = 0.5$, as a preliminary result. This may confirm the supergiant status of the star.

The period study has revealed a 288 day variation in the light curve which is probably caused by the orbital motion: the varying distance means varying optical path in the circumstellar cloud. This periodicity cannot be detected in the color curve, hence the cloud in the line-of-sight is very homogeneous. The orbital parameters of the 89 Her system (Waters et al. 1993) are: $P_{\rm orb} = 288.36$ d, $e = 0.189$, K=3.09 km s^{-1}, $a_1 \sin i = 12 \times 10^6$ km, $f(M_2) = 0.0008\,M_\odot$. If we assume a mass of $0.6\,M_\odot$ for the primary, the most probable mass of the secondary is between 0.08 and $0.15\,M_\odot$. Adopting a luminosity for the primary of $3000\,L_\odot$, the radius is about $43\,R_\odot$ for an effective temperature of 6500 K.

2. Spectroscopic observations

High resolution optical spectroscopy was carried out on eight nights in 1996 and three nights in 1997 at the David Dunlap Observatory. We used the 1.88 m telescope equipped with the echelle spectrograph. The studied wavelength region was between 6200–6600 Å in 1996 and 5860–6660 Å in 1997. The resolution ($\lambda/\Delta\lambda$) is about 30000, while the typical S/N ratio is around 150-200.

A sample spectrum is shown in Fig. 1. The studied wavelength range covers the strong sodium D doublet and the Hα line. The latter shows very characteristic P Cygni-profile, usually attributed to a strong stellar wind. Other P Cygni-profiles are present, too, while the spectrum is fairly rich in very narrow emission lines. Several absorption lines make the spectrum partially similar to that of the "normal" stars. The general appearance suggests that even in the optical ranges the star is barely visible through the circumstellar nebula.

A question arises: how can we derive stellar radial velocities from such spectra? There are very few pure absorption lines originating in the stellar photosphere, the majority of spectral lines is disturbed by one or more emission components. It looks almost impossible to separate stellar and circumstellar contributions. Therefore, we conclude that earlier radial velocity data from medium-resolution spectra should be carefully re-analysed.

Some interesting conclusions are based on simple comparisons of different spectral lines. First, we compare the strongest sodium doublet and the Hα line

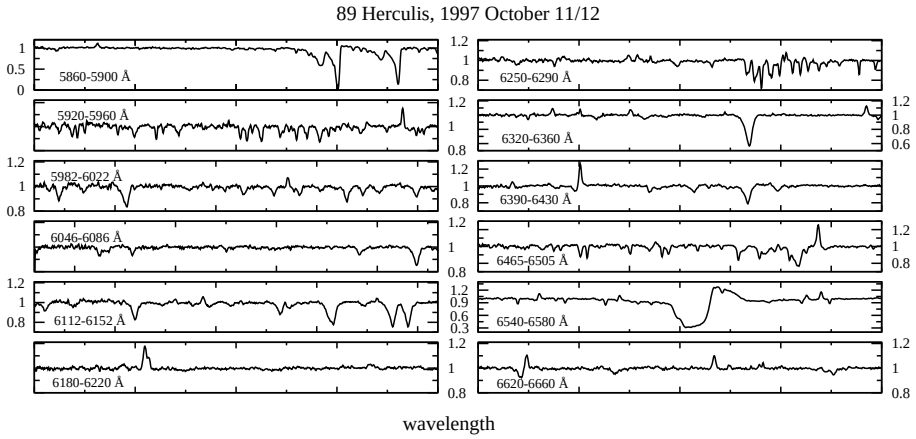

Figure 1: A sample spectrum of 89 Herculis taken in 1997. Note the different scaling of the vertical axes in different subpanels.

(Fig. 2). The two components of the doublet have very similar substructures. They are likely to originate in discrete circumstellar shells with different expansion velocities. The close similarity to the velocity structure of the Hα line strengthens the idea that the weaker components of the doublet originate at 89 Her indeed, not in the intervening interstellar matter. One can identify a shell with $v_{exp} \approx 85\,km\ s^{-1}$, while a weaker feature is unambiguously present with $v_{exp} \approx 140\,km\ s^{-1}$.

Second, two metallic P Cygni-profiles were compared with a pure Si II absorption line and sodium D1 line. It is interesting, that the emission components of the P Cygni-profiles coincide with the minimum of the absorption line, while the sodium D is displaced relative to all lines by more than $+10\,km\,s^{-1}$.

Finally, three narrow emission lines are compared (Fig. 2). The radial velocities of the emission peaks are in very good agreement, however, the seemingly pure emission lines have companion absorption components at $\sim$–$120\,km\,s^{-1}$. Our conclusion is that the optical spectrum of 89 Her is extremely complex due to the presence of circumstellar matter. A future investigation should address the various components of the whole system (a pulsating post-AGB star, a secondary companion of unknown nature, a thick circumstellar nebula with discrete velocity structures) and their contributions to the observed spectrum.

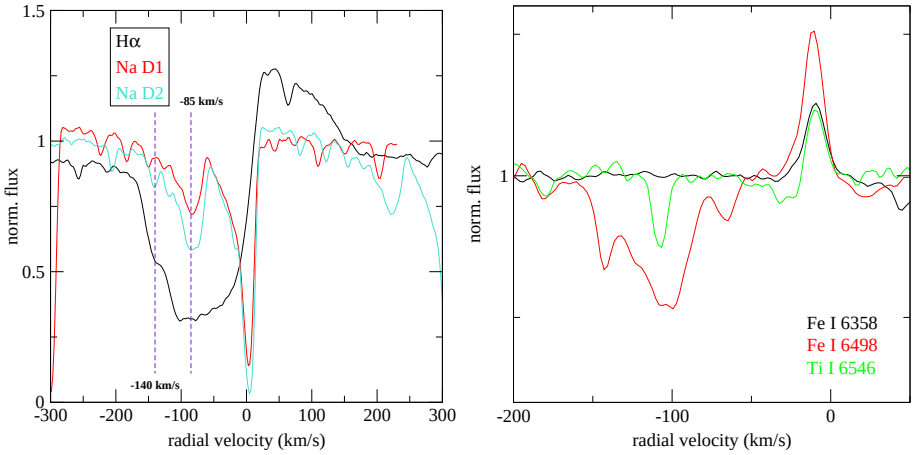

Figure 2: Left: A comparison of the strongest spectral lines. A main expansion velocity of 85 km s^{-1} is suggested by the absorption minimum of the hydrogen P Cygni-profile and the secondary components of the sodium doublet. A weaker feature is also present at –140 km s^{-1}. Right: A comparison of three seemingly pure emission lines. Although the absorption features look similar, the Fe I 6498 and Ti I 6546 lines are in that spectral region which is strongly affected by the atmospheric telluric lines.

Acknowledgements

This work was supported by the Hungarian OTKA grants No. T032258 and T034615, the "Bolyai János" Research Scholarship of LLK from the Hungarian Academy of Sciences and FKFP Grant 0010/2001.

References

Percy, J.R., Bakos, A.G., Henry, G.W., 2000, PASP 112, 840
Szatmáry, K., Kiss, L.L., 1997, IAPPP Comm. No. 67, 66
Waters, L.B., Waelkens, C., Mayor, M., Trams, N.R., 1993, A&A 269, 242

Winds and Bubbles

Stellar Driven Flows in Multi-Phase media

J.E. Dyson

Department of Physics and Astronomy
University of Leeds, Leeds, LS2 9JT, UK

Abstract

After a brief overview of the evolution of flows driven by winds and explosions in single phase media, we briefly describe some of the features of mass injection. We then describe recent work on mass injection into wind-blown bubbles and supernova remnants. We make some final remarks on shocks in multi-phase media.

1. Introduction

Most flows in diffuse astrophysical sources are driven by the injection of mass, momentum and energy. This injection can be impulsive e.g. flows driven by stellar explosions such as novae and supernovae or can be continuous e.g. flows driven by stellar winds and radiation fields. Of course these are not mutually exclusive and in some situations, this distinction is not clear cut. So, for example, a sequence of impulsive events (e.g. supernovae) may often be reasonably approximated as a continuous wind with a mean power of the supernova energy divided by the characteristic time between explosions.

The literature on these flows is vast and just a very few classic papers are mentioned here. Flows driven by the action of stellar UV radiation were classified by Kahn (1954); supernovae induced flows were studied by Shklovskii (1962) and flows driven by fast stellar winds by Pikel'ner (1968). We will here deal only with the latter two types of flow. A useful overview of a variety of problems associated with shock propagation has been given by Bisnovatyi-Kogan & Silich (1995).

2. A brief overview of the evolution of flows in single phase media

2.1. Supernova remnants

In the initial free expansion phase, a forward shock is driven into the supernova site surroundings at velocity $V_s \cong$ constant, so the shock radius $R_s \propto t$, where t is the time. An accelerating reverse shock propagates into the supernova

ejecta. When the mass swept up by the forward shock is O(10) times the ejected mass, the remnant enters the Sedov-Taylor stage of evolution in which only the forward shock remains. Radiation losses are negligible and the remnant evolves with time as $R_s \propto t^{2/5}$, $V_s \propto t^{-3/5}$. Eventually, radiation losses remove thermal energy from all except the very hot interior and the remnant enters the 'pressure-driven snowplough' regime during which $R_s \propto t^{2/7}$ and $V_s \propto t^{-5/7}$. Depending on circumstances, the hot interior may eventually cool and the resulting 'momentum-driven snowplough' evolves as $R_s \propto t^{1/4}$, $V_s \propto t^{-3/4}$. A very comprehensive overview of supernova remnant evolution is given by Truelove & McKee (1999).

2.2. Wind driven interactions

As in the supernova driven interaction, there are two shocks generated, a forward one into the ambient gas and a reverse shock into the ejecta (i.e. the wind). However, the continuous wind means that the reverse shock never collapses onto the stellar surface and the 'two-shock' flow pattern first described by Pikel'ner (1968) moves outwards in the stellar frame. The flow depends largely on the thermal behaviour of the shocked wind. If this wind behaves adiabatically, the outwards shock is driven by the pressure of the shocked wind and the flow is often referred to as 'energy' driven. In that case the outer shock evolves as $R_s \propto t^{3/5}$, $V_s \propto t^{-2/5}$. On the other hand, if the shocked wind cools quickly, the flow is driven by the wind momentum and, unsurprisingly, is then referred to as 'momentum driven'. In that case the outer shock evolves as $R_s \propto t^{1/2}$, $V_s \propto t^{-1/2}$. The type of flow that occurs is determined effectively by the wind velocity. Roughly for wind speeds less than 100 kms^{-1} or so momentum driven flows occur and energy driven flows occur if the wind speed is higher (e.g. Dyson, 1984). So, at least in single phase media, the very fast ($\geq$ few hundred kms^{-1}) winds from stars such as OB stars, Wolf-Rayet Stars and planetary nebula nuclei set up energy driven flows. Winds from YSOs (Young Stellar Objects) which are slower ($\approx$ hundred kms^{-1}) produce either momentum driven flows or energy driven flows since the transition is extremely sharp (Dyson, 1984). Flows can evolve from one type into another dependent on temporal variations in wind power output and/or spatial variations in the ambient density. A thorough treatment is given by Koo & McKee (1992a) and Koo & McKee (1992b).

3. Why study flows in multi-phase media?

Practically every diffuse astronomical source consists of 'cool' clumps embedded in a 'hot' substrate. These include stellar envelopes ejected in the late stages of stellar evolution, molecular clouds and star forming regions and the nuclear regions of active galaxies. Mass from the clumps can be picked up by the global flow initiated by any of the mechanisms above and the resulting dynamics, physics and chemistry of this global flow are thereby altered. The back reaction on the flow may also affect the mass injection mechanism.

There are several ways of injecting material into a flow. The photoevaporation of clumps depends on the presence of an ionizing radiation field. Conduction from cool clumps to the hot substrate may occur; depending on circumstances the inverse may also happen. Clumps can be shredded when overrun by shock waves and the clump material added to the global flow. Finally, simple hydrodynamic ablation via the Bernoulli effect may also happen.

A wide variety of problems involving mass injection have been studied in the literature. A far from exhaustive (though biased) selection includes: the internal dynamics of Wolf-Rayet nebulae (e.g. Hartquist et al., 1986; Arthur et al., 1993, 1994, 1996); ultra-compact HII regions (e.g. Dyson, 1994; Dyson et al., 1995; Lizano et al., 1996); planetary nebula jets (Redman & Dyson, 1999); supernova remnants (McKee & Ostriker, 1997).

4. The scales involved in mass-addition

There is a distinct hierarchy of spatial scales involved in the mass-pick up process. On the smallest scales, mass is accelerated in boundary layers towards full integration with the global flow. Because the global flows are directional, there is the tendency for the accelerated material to be stretched in the flow direction-these are the intermediate scale 'tail' features. The integration of the swept-up material into the global flows takes place on these scales. Finally, the largest scale is the flow itself. Provided there is suitable diagnostic emission or absorption, these various structures can be investigated in astronomical sources giving information on processes that are either difficult or impossible to study under terrestrial laboratory conditions.

5. Remarks on tails

Tail features are interesting for (at least) two reasons. Firstly they provide some of the most intriguing examples of morphology (e.g. the tails in the Helix Nebula NGC 7293, and those of the Orion PROPLYDs). Secondly, it is over these scales in which the integration of the picked up material into the global flow finally takes place and the efficiency of this integration (i.e. the coupling between the global flow and the picked up material) depends on the tail morphology. Very clearly, there is much better coupling if the tails are broad rather than thin, although the number of clumps per unit volume also plays a role. It is worth noting here that all the work discussed later assumes that the mass injection and assimilation into the global flow occurs over length scales much shorter than those associated with the global flows. Thus the likely coarse grain nature of real flows is ignored.

There are in fact several ways of generating visible tail structures. Although we are here concerned with real tails (in the sense that they contain real moving material), what appear observationally to be tails can be formed by the shadowing of radiation fields (e.g. van Berkblom & Arny, 1972; Cantó et al., 1998). The hydrodynamic formation of tails has been discussed on a phenomenological basis by Dyson et al. (1993). These authors considered the way gas liberated from a long-lived source interacted with a uniform stream of gas. There are in principle four possible basic interactions since the source and stream gas can be subsonic or supersonic. Dyson et al. (1993) concluded that wide tails are generated whenever a supersonic stream interacts with either subsonic or supersonic source material or a subsonic stream interacts with supersonic source material. They thus suggested that long thin tails are produced only if a subsonic stream interacts with subsonic source gas. This statement needs the caveat that in addition, any viscous energy dissipation in the tail must be balanced by radiative cooling (Hartquist et al., 1996).

This basic premise has been supported by numerical calculations (Falle et al., 2001) which looked at the interaction of subsonic and supersonic streams with subsonic source material. The wind was assumed to behave adiabatically and the stream gas isothermally. The subsonic-subsonic interaction gave a long thin tail.

An important related problem under study is the interaction of winds with distributed sources and the question of whether a global shock is formed or whether individual shocks occur around individual sources. Some important work has been done on the interaction of global shocks with multiple clumps (Poludnenko et al., 2002), but in these calculations, the clumps are destroyed

by the shocks.

Since the forms of intermediate scale structures depend on the Mach numbers of the global flows, and they in turn determine the coupling between the source and the flow, it is clear that self-consistent flows really need to be studied. In the next sections we will consider a step in this direction by investigating the flows that can be produced with distributed mass loading terms.

6. Mass injection into stellar wind driven flows

Pittard et al. (2001a) and Pittard et al. (2001b) have constructed similarity solutions that describe adiabatic wind-blown bubble evolution with mass loading. Although similarity solutions are rather specialised, they do give some insight into the problems they attempt to describe. The basic equations are the usual conservation of mass, momentum and energy with an appropriate mass injection term added to the continuity equation, specified according to the mode of mass injection.

For conductive (saturated Spitzer) injection, the volume mass injection rate is proportional to $T^{5/2}$, where T is the temperature. For hydrodynamic ablation, the prescription given by Hartquist et al. (1986) is used. In this, the mass injection rate is proportional to M^{γ}, where γ takes the value of 0 if the flow is supersonic relative to the clumps and 4/3 if the flow is subsonic. M is the flow Mach number. We specify the inter-clump density as $\rho = \rho_o r^{\beta}$. A spatial dependency of the mass injection is included through a term r^{λ}.

In the case of hydrodynamic ablation, the similarity variable is $x = rQ^{1/(5+\lambda)}\dot{E}^{-1/(5+\lambda)}t^{-2/(5+\lambda)}$, and for conductive injection $x = rQ^{1/(10+\lambda)}\dot{E}^{-1/(10+\lambda)}t^{-7/(10+\lambda)}$. Here, Q is the constant of proportionality in the mass injection term, $\dot{E}$ is the energy injection rate and t is the time. In the usual way, the coupled partial differential conservation equations reduce to a set of ordinary differential equations. In order to do this, there is the requirement that $\lambda = (2\beta - 5)/3$ in the ablation case and $\lambda = (5 + 7\beta)/3$ in the conductive case.

To summarise the results:

i) Hydrodynamic ablation. Substantial mass loading of wind-blown bubbles occurs over a wide range of λ. If $\lambda \leq -2$, the bubble mass is larger than that of the swept up shell. The profiles of the flow variables are significantly altered under conditions of large mass loading. In contrast to cases with little mass loading, the density and temperature increase and the velocity and Mach numbers drop. As expected, mass loading of the wind strongly reduces

the Mach number of the inner shock (c.f. Williams et al., 1995). Indeed the wind can mass-load sufficiently to go through a sonic point and thus avoid a termination shock altogether. Importantly, depending on circumstances, the flow may have anything from none to several sonic points. (Note that the mass loading is determined so as to be self-consistent with the Mach number of the local flow).
ii) Conductive evaporation. As before, substantial mass loading can occur over a wide range of λ. Here though the bubble mass is larger than that of the swept-up shell if $\lambda \geq 4$. With high mass loading, the average density of the shocked region is larger, the deceleration of the flow is shallower and the temperature of the shocked wind rapidly decreases. The shocked wind region can be entirely subsonic, entirely supersonic or have one or sometimes two sonic points. For a given value of λ and ratio of the radii of the inner and outer shocks, there is a maximum value of the mass loading that can occur.

These solutions give some idea of the complexities produced when mass injection occurs in stellar wind driven bubbles. It is clear that the effects of mass injection are such that the results on bubble dynamics and evolution obtained from calculations in smooth media (e.g. for planetary nebulae) should be viewed with caution.

7. Mass injection into supernova remnants

As in the case of stellar wind driven bubbles, by far the majority of investigations do not include the effects of mass addition. Cowie et al. (1981) numerically modelled the effects of a supernova explosion on medium where discrete clouds are embedded in a lower density substrate. The cloud material is thermally evaporated into the remnant. There have been various similarity solutions derived where, as above for the wind-blown bubbles, clouds are treated as continuously distributed mass injection sources. McKee & Ostriker (1997), Chièze & Lazareff (1981) and White & Long (1991) assumed that conductive evaporation drives mass injection. (Dyson & Hartquist, 1987) assumed that material is hydrodynamically ablated into remnants according the prescription given in Section 6. Arthur (1994) made a preliminary numerical study of the effects of hydrodynamic mass loading due to hydrodynamic ablation on supernovae remnants in the adiabatic case. Arthur & Henney (1996) used numerical simulations of mass loaded supernova remnants to explain the excess soft X-ray emission in bubbles in the Large Magellanic Cloud.

Mass loaded supernova remnants are important in a variety of contexts. A

remnant propagating inside a molecular cloud propagates through a multiphase medium with a complex structure partly determined by the interaction of the progenitor star or neighbouring stars with the cloud. The range of the remnant in the cloud is a significant factor in the importance of the remnant for e.g. sequential star formation. On larger scales, the collective effects of supernova explosions drive galactic superwinds (e.g. Chevalier & Clegg, 1985; Heckman et al., 1990; Suchkov et al., 1996) showed that the superwind in the starburst galaxy M82 must be mass loaded to account for the observed X-ray emission. This necessary mass injection can be supplied by conductive or ablative cloud evaporation in the core of M82 (Hartquist et al., 1997). The ranges of individual remnants are affected by mass loading; clearly these in turn affect the global wind dynamics. Quite accurate approximations, confirmed by appropriate numerical modelling, are available to describe remnant evolution in smooth media (Cioffi et al., 1988; Truelove & McKee, 1999, and references therein). These approximations represent unified solutions for remnant evolution in the early (Truelove & McKee, 1999) and later (Cioffi et al., 1988) stages. Such solutions have the convenient property that only one simulation need be performed for each regime to determine the evolution of all remnants with the same form of initial ejecta and ambient medium density. In principle these solutions could be used to study problems where multiple supernova events occur and where it would be inconvenient to model each individual event. Since, as noted above, mass loaded remnants are important in a variety of contexts, it is useful to have similar approximations available for the mass loaded case.

Dyson et al. (2002) have calculated the evolution of supernova remnants in which mass loading takes place by hydrodynamic ablation. A related calculation where mass loading takes place by conductive evaporation has been made by Pittard et al. (2002). The basic equations are as in Section 6 with the addition that radiative cooling (assumed to be collisional ionization equilibrium cooling) is added to the energy equation.

In all cases studied, once mass loading becomes significant, the internal structures of remnants deviate appreciably from the structures of standard remnants with no mass loading. The distribution of the remnant energy between thermal and kinetic also changes from that of standard remnants.

In the case where mass injection is hydrodynamic, most significantly, the ranges of supernova remnants (defined at the time they have retained 50% of the initial explosion energy), are strongly influenced by the mass added. For example, a remnant that is heavily mass loaded can affect less than 1% of the volume which would be affected by a standard remnant with the same energy and evolving in a medium with the same ambient density. Clearly ranges are

very seriously affected. It is worth noting that there are significant differences between the evolution of remnants where the prescription for mass loading of Hartquist et al. (1986) is used and where a constant (i.e. Mach number independent) injection rate is assumed only once cooling has occurred. Up to this stage, the differences, given the uncertainties in the physics, are negligible.

The situation is very different when mass addition takes place by thermal evaporation. The reason is straightforward; this latter mass injection is very temperature sensitive and the internal temperature structure can change dramatically spatially and temporally during remnant evolution. Moreover, conductively driven mass loading has a built in limitation mechanism. Mass addition tends to result in lower temperatures that reduce the mass loading rates. Once the interior temperatures of remnants drop below about 10^7K, mass addition rates decrease very sharply. Thus the main differences between these mass loaded models and standard models occur in the earlier stages of evolution. The later stages, where swept up gas dominates in either case, are rather similar.

The main differences between the ablation and conductively loaded remnants are that at late times, the former are dominated by added mass and most of the energy is thermal; the latter are dominated by swept up mass and kinetic energy. Ablation loaded remnants evolve more quickly and reach all dynamical stages earlier than conductively loaded remnants. At any given age, they tend to be more massive and smaller than equivalent remnants that are conductively mass loaded.

8. Discussion

Although the effects of mass addition to flows have been studied at some level for over two decades, it is evident that an enormous range of investigations still remains. In part, this is due to increasing observational data (e.g. on superwinds) which demand the inclusion of mass loading for their interpretation. In part there are fundamental processes associated with mass injection and the assimilation of the injected mass into global flows that remain badly understood. For example, there is evidence that clumps in molecular clouds may be magnetically supported but little work has been done on the photoionization of magnetised clouds. There are even more basic problems that need elucidation. Williams & Dyson (2002) have made a study of the structure of shock waves in two-phase media where simple assumptions were made for the dynamical coupling between a tenuous hot phase and a dense cool phase. The results, even for these simple models, show very important changes from standard shocks,

since the 'shocks' now are resolved regions where the two components interact. Another important question is what determines whether global shocks are set up in flows or whether individual shocks around injection sources predominate. Mass loaded flows will continue to provide gainful employment for astronomers and astrophysicists for some time.

Acknowledgements

I am grateful to my many collaborators for doing most of the work presented here. They are Jane Arthur, Rob Coker, Sam Falle, Tom Hartquist, Julian Pittard, Matt Redman, Robin Williams. I would also thank the organisers of this second meeting for their kind invitation to give a talk in such a marvellous country.

References

Arthur, S.J., Dyson, J.E., Hartquist, T. W., 1993, MNRAS 261, 425
Arthur, S.J., Dyson, J.E., Hartquist, T. W., 1994, MNRAS 269, 1117
Arthur, S.J., Henney, W.J., 1996, ApJ 457, 752
Arthur, S.J., Henney, W.J., Dyson J.E., 1996, A&A 313, 897
Bisnovatyi-Kogan, G. S., Silich, S.A., 1995, Rev. Mod. Phys. 67, 661
Cantó, J., Raga, A., Steffen, W., Shapiro, P., 1998, ApJ 502, 695
Chevalier, R., Clegg, A., 1985, Nature 317, 44
Chièze, J.P., Lazareff, B., 1981, A&A 95, 194
Cioffi, D.F., McKee, C.F., Bertschinger, E., 1988, ApJ 334, 252
Cowie, L.L., McKee, C.F., 1977, ApJ 211, 135
Cowie, L.L., McKee, C.F., Ostriker, J.P., 1981, ApJ 247, 908
Dyson, J.E., 1984, A&SS 106,181
Dyson, J.E., 1994, in: Lecture Notes in Physics 431, *Star Formation and Techniques in Infrared and mm-wave Astronomy*, Ray, T.P., Beckwith, S.V. (eds.), Springer Verlag, Berlin, p.93
Dyson, J.E., Arthur, S.J., Hartquist, T.W., 2002, A&A 390, 1063
Dyson, J.E., Hartquist, T.W., 1987, MNRAS 228, 453
Dyson, J.E., Hartquist, T.W., Biro, S., 1993, MNRAS 261,430
Dyson, J.E., Williams, R.J.R., Redman, M.P., 1995, MNRAS 277, 700
Falle, S.A.E.G., Coker, R.F., Pittard, J.M., Dyson, J.E., Hartquist, T.W., 2001, MNRAS 329, 670
Hartquist, T W., Dyson, J.E., Pettini, M., Smith, L.J., 1986, MNRAS 221, 715
Hartquist, T.W., Dyson, J.E., Williams, R.J.R., 1996, A&SS 235, 165
Hartquist, T.W., Dyson, J.E., Williams, R.J.R., 1997, ApJ 482, 182
Heckman, T.M., Armus, L., Miley, G.K., 1990, ApJS 73, 833

Kahn, F.D., 1954, BAIN 12, 187
Koo, B.C., McKee, C.F., 1992a, ApJ 388, 93
Koo, B.C., McKee, C.F., 1992b, ApJ 388, 102
Lizano, S., Cantó, J., Garay, G., Hollenbach, D., 1996, ApJ 468, 739
McKee, C.F., Ostriker, J.P., 1997, ApJ 218,148
Pikel'ner, S.B., 1968, Ap. Lett. 2, 97
Pittard, J.M., Dyson, J.E., Hartquist, T.W., 2001a, A&A 367, 1000
Pittard, J.M., Hartquist, T.W., Dyson, J.E., 2001b, A&A 373, 1043
Pittard, J.M., Arthur, S.J., Dyson, J.E., Falle, S.A.E.G., Hartquist, T.W., Knight, M.I., Pexton, M., 2002, A&A (submitted)
Poludnenko, A.Y., Frank, A., Blackman, E.G., 2002, in: *Mass outflow in Active Galactic nuclei: New Perspectives*, ASP Conference Series Vol. 255, eds. Crenshaw, D.M., et al., p.285
Redman, M.P., Dyson, J.E., 1999, MNRAS 302, L17
Shklovskii, I.S., 1962, Sov. Ast. 6, 162
Suchkov, A.A., Berman, V.G., Heckman, T.M., Balsara, D.S., 1996, ApJ 463, 528
Truelove, J.K., McKee, C.F., 1999, ApJS 120, 299
van Berkblom, D., Arny, T.T., 1972, MNRAS 156, 91
White, R.L., Long, K.S., 1991, ApJ 373, 543
Williams, R.J.R., Hartquist, T.W., & Dyson J.E., 1995, ApJ 446, 759
Williams, R.J.R., Dyson, J.E., 2002, MNRAS 331, 1

The Breakout of Protostellar Winds in the Infalling Environment

F.P. Wilkin

Instituto de Astronomía, UNAM
Apdo. Postal 3-72 (Xangari), 58089 Morelia, Michoacán, Mexico
E-mail: f.wilkin@astrosmo.unam.mx

Abstract

The time of protostellar wind breakout may be determined by the evolution of the infalling flow, rather than any sudden change in the central engine. I examine the transition from pure infall to outflow, in the context of the inside-out collapse of a rotating molecular cloud core. I have followed numerically the motion of the shocked shell created by the impact of a stellar wind and infalling gas. These fully time-dependent calculations include cases both where the shell falls back to the stellar surface, and where it breaks out as a true outflow. Assuming a wind launched from the protostellar surface, the breakout time is determined in terms of the parameters describing the wind ($\dot{M}_w$, V_w) and collapsing cloud core ($a_\circ$, Ω). The trapped wind phase consists of a wind sufficiently strong to push material back from the stellar surface, but too weak to carry the heavy, shocked infall out of the star's gravitational potential. To produce a large-scale outflow, the shocked material must be able to climb out of the star's gravitational potential well, carrying with it the dense, swept-up infall.

KEYWORDS: *circumstellar material–ISM: jets and outflows–stars: mass-loss–stars: pre-main-sequence*

1. Introduction

Because essentially all known protostellar or pre-main sequence objects show evidence of winds, jets, or outflows, the current thinking is concentrated on a picture of simultaneous infall and outflow, in which infall and accretion occur towards the protostellar equatorial regions, and a wind breaks out along the poles (e.g. André et al., 1993). Yet early thinking on the stages of young stellar evolution identified a phase in which infall directly strikes the protostellar surface, with no outflow present (Shu et al., 1987), no clear examples are known of such protostars. In this contribution I consider limits on the timescale for purely-accreting objects in the context of the standard model of inside-out collapse

from a molecular cloud core. The mathematical formulation is a generalization of Wilkin & Stahler (1998), dropping the assumptions of normal force balance and quasi-stationarity to permit full time-dependence and dynamical expansion (or collapse).

2. Description of the Infall, Wind, and Protostar

The inside-out collapse of a singular, isothermal sphere yields a mass accretion rate $\dot{M}_i = 0.975\, a_\circ^3/G$ at the center (Shu, 1977). Here $a_\circ$ is the isothermal sound speed in the cloud core. At the origin is a protostar whose mass grows linearly in time $M_* = \dot{M}_i\, t$, where t is the time since the start of collapse. In the presence of initial, solid-body rotation, the infall is distorted, and accretion occurs preferentially onto the circumstellar disk (Ulrich, 1976; Cassen & Moosman, 1981; Terebey et al., 1984). The natural length scale of the distortion is the centrifugal radius R_{cen}, which grows as t^3. I turn on a wind at the stellar surface, of radius R_*, and numerically determine whether it can halt infall and escape. At early times, $R_{cen} \ll R_*$ and the accretion is nearly isotropic, making breakout of the wind difficult. At late times, when $R_{cen} \gg R_*$, escape becomes easy along the poles.

For simplicity, the wind is assumed isotropic and of constant speed V_w, and mass-loss rate $\dot{M}_w$. The wind and infall collide supersonically, and a shocked shell forms. Low speeds imply rapid cooling and a geometrically thin shell. The dynamics of such time-dependent, thin shells has been discussed in detail by Giuliani (1982). I include the inputs of mass and momentum from infall, the wind, and the gravitational force due to the protostar.

3. The Trapped Wind Stage

For a given evolutionary time and ratio $\alpha \equiv \dot{M}_w/\dot{M}_i$, I determine the minimum wind speed necessary to break out of the infalling flow. Fig. 1 shows an example calculation of a shell that fails to escape and falls back to the star. In this case, a modest increase in wind speed dramatically changes the outcome, permitting breakout of the shell from the infall region. I solved the problem in dimensionless form, which reduces the parameter space from six (R_*, $\dot{M}_w$, V_w, $a_\circ$, Ω, t) to three dimensions (nondimensional time τ, wind speed ν, and α). As a result, the parameter space has been fully explored. Fig. 2 shows the critical wind speed for breakout. When the wind ram pressure exceeds the infall ram pressure at the stellar surface, the wind may initially push the shell upwards. But if the

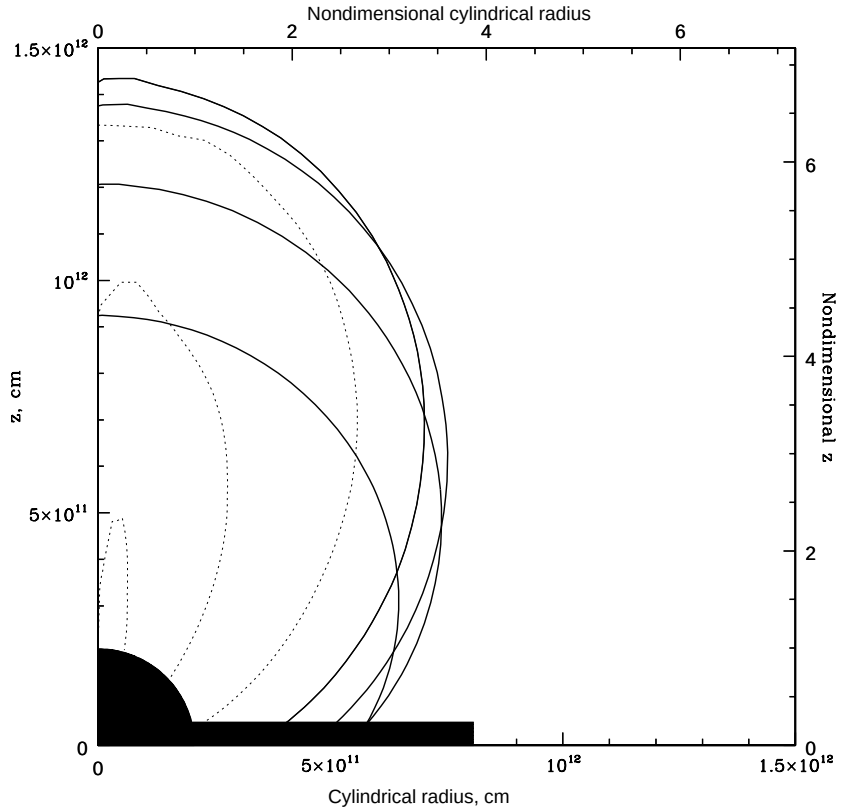

Figure 1: Time-evolution of a failed outflow. The solid curves show the initial rise, while dotted curves show the subsequent recollapse. The protostellar age since core formation is 3.8×10^4 years. The shapes correspond to equal time intervals of 0.016 years. The size of the centrifugal radius is indicated by the disk. Lengths are in cm on the left and bottom axes, and in units of the stellar radius on the remaining axes.

wind speed is less than the critical speed, the shell stalls and falls back. This is the trapped wind stage. In Fig. 3, its duration is the time between the dashed (ram pressure balance) curve and the solid one (critical wind speed) for a given ratio $\alpha \equiv \dot{M}_w/\dot{M}_i$.

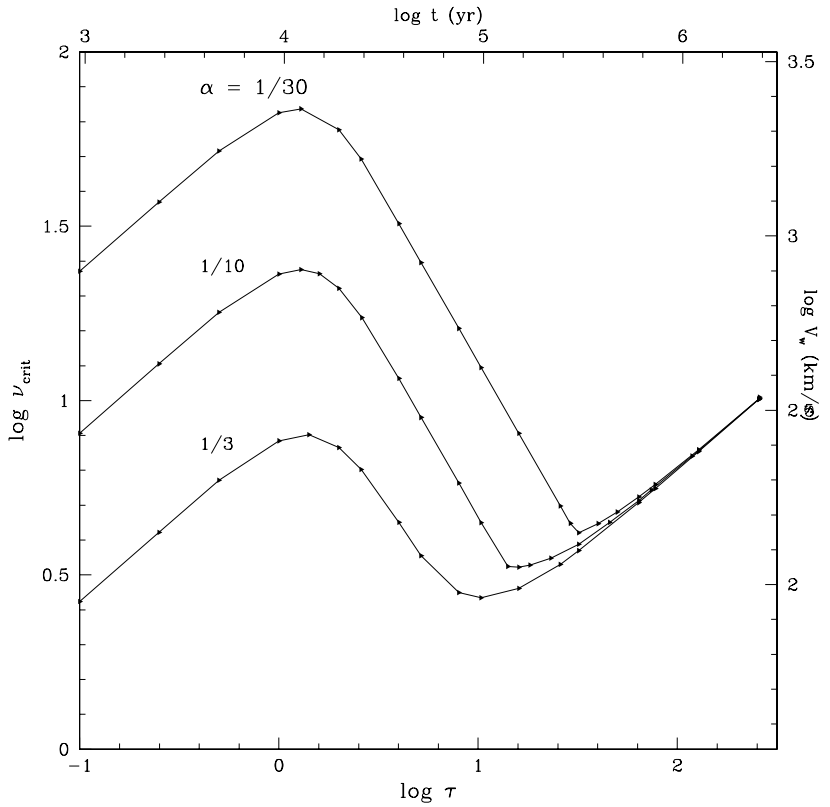

Figure 2: Minimum breakout wind speed versus evolutionary time. The three loci correspond to three ratios, α, of the wind mass loss to infall accretion rate. For a given α, the region above the curve corresponds to breakout, while that below the curve corresponds to recollapse. The power-law increase in v_{crit} at early and late times is associated with the increasing gravitating mass of the protostar.

4. Discussion

The results of Figs. 2 and 3 may be easily scaled to apply to *anisotropic* winds, by comparing to an equivalent, isotropic wind having the same mass and momentum loss rates along the z-axis. Indeed, at early times, the evolution is

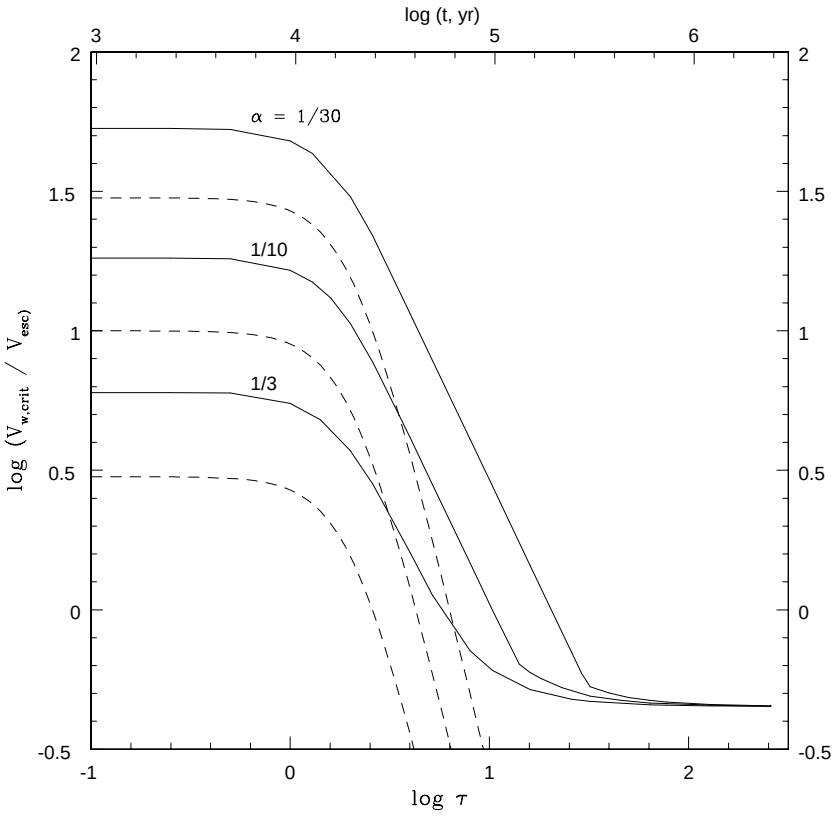

Figure 3: Critical wind speed for breakout (solid curves), in units of the free-fall (escape) speed, as a function of evolutionary time. The corresponding α-values are shown, as well as the wind speed necessary for ram pressure balance at the stellar surface (dashed curves). Assuming wind launch conditions $V_w/V_{esc} = const.$ (i.e. following a horizontal line in this figure), evolution begins at the left edge of the plot with the wind unable to advance beyond the stellar surface until the line intersects the appropriate dashed curve. Then the "trapped wind" phase lasts until the line intersects the corresponding solid curve for breakout. For example, for $V_w/V_{esc} = 1.6$, we follow a horizontal line at $\log(V_w/V_{esc}) = 0.2$. The trapped wind phase begins at $t \approx 19\,000\,yr$, while breakout occurs only at $t \approx 38\,000\,yr$, indicating a substantial duration for the trapped wind stage.

primarily determined by the momentum loss rate of the wind in this direction. At late times, it is the wind speed rather than momentum loss rate that determines breakout. It is hoped that these semi-analytic results will inspire more detailed exploration of this problem with fully radiative hydrodynamic simulations. The existing literature (e.g. Frank & Noriega-Crespo, 1994) on this is not immediately comparable because they have used a different density law which is self-similar, unlike that of Cassen & Moosman. Moreover, I argue that initial conditions with wind velocity much greater than the critical velocity are unphysical, as such a strong wind would have broken out at an earlier time, unless the wind itself evolves strongly with time.

Strong collimation of wind by anisotropic infall is not seen in the current calculations, although further exploration of this issue is forthcoming. I note that numerical simulations demonstrating strong collimation due to the circumstellar density asymmetry (e.g. Delamarter et al., 2000) have assumed a much more asymmetric density field than that used here.

Acknowledgements

I am grateful to the Observatoire de la Côte d'Azur for a Henri Poincaré Fellowship and to the Département Fresnel, UMRS 5528 for hosting my postdoctoral stay in France. I also thank CONACyT/México for financial support and S. Stahler for encouragement in this work.

References

André, P., Ward-Thompson, D., Barsony, M., 1993, ApJ 406, 122
Cassen, P., Moosman, A., 1981, Icarus 48, 353
Delamarter, G., Frank, A., Hartmann, L., 2000, ApJ 530, 923
Frank, A., Noriega-Crespo, A., 1994, A&A 290, 643
Giuliani, J.L., 1982, ApJ 256, 624
Shu, F.H., 1977, ApJ 214, 488
Shu, F.H., Adams, F.C., Lizano, S., 1987, ARAA 25, 23
Terebey, S., Shu, F.H., Cassen, P., 1984, ApJ 286, 529
Ulrich, R.K., 1976, ApJ 210, 377
Wilkin, F.P., Stahler, S.W., 1998, ApJ 502, 661

VLA Observations of WR6: A Search for an Anisotropic Wind

M.E. Contreras[1], L.F. Rodríguez[1], E.M. Arnal[2]

[1]Inst. de Astronomía, UNAM, Apdo.Postal 3-72, Morelia, Mich. 58089, México
[2]Inst. Argentino de Radioastronomía, C.C. 5, 1894 Villa Elisa, Argentina
E-mail: m.contreras@astrosmo.unam.mx

Abstract

The interaction between a stellar wind and its surrounding ISM can create HI cavities or bubbles. In particular, WR 6 shows a very large ovoidal HI bubble around it, whose shape cannot be explained in terms of the standard interstellar bubble theory and may require an anisotropic wind. We have studied this possibility using 3.6-cm VLA observations. We found no firm evidence supporting that WR 6 has a strong anisotropic wind. We conclude that our results are consistent with a classic thermal wind. Under this assumption we have determined the source size, its brightness temperature and its mass loss rate.

Keywords: *Radio Continuum: Stars – Stars: Wolf-Rayet, Individual (WR6) – Stellar Winds*

1. Introduction

Strong winds from massive stars are moving supersonically with respect to the ambient gas, creating a so-called bubble or cavity. Because of their strong stellar winds Wolf-Rayet stars are the best candidates to form an HI cavity around them. Some studies have been carried out to examine the HI distribution around WR stars and to analyze the dynamics and energetic interactions between their stellar wind and the interstellar medium.

Arnal & Cappa (1996) examined the distribution of HI around WR 6. They concluded that the HI bubble is not expanding and that if the standard hydrodynamic stellar wind-blown bubble theory is to be retained in its original form, the most likely explanation is that the central star has a non-isotropic stellar wind.

2. Observations

We present four sets of observations taken with the Very Large Array (VLA) at 3.6-cm. The first observing run was carried out on July 25, 1996. At this epoch

the array was in the D configuration giving the lowest angular resolution. The next three observing runs were made on November 25, December 21, 1996 and on January 12, 1997. During these epochs the array was in the A configuration giving an angular resolution of $\sim 0\farcs2$. The amplitude and phase calibrators were the same for all runs, 1328+307 and 0646-306, respectively. Bootstrapped flux densities for the phase calibrator as well as for WR 6 obtained from each observing run are shown in Table 1.

Table 1: Derived Flux Densities

Observing Run	**0646-306** S_ν [Jy]	**WR 6** S_ν [mJy]
July 25, 1996	0.804 ± 0.006	1.56 ± 0.03
November 26, 1996	0.867 ± 0.005	1.62 ± 0.03
December 21, 1996	0.875 ± 0.005	1.35 ± 0.03
January 12, 1997	0.880 ± 0.004	1.38 ± 0.03

The data analysis and reduction were performed using AIPS and following the standard VLA procedures for editing, calibrating and imaging.

3. Discussion

The presence of an anisotropic wind in WR 6 is important because it could be or could have been in the past related to the elongated HI bubble observed by Arnal & Cappa (1996) at a large scale. It was then important to resolve angularly the source both to detect any possible deviation from the spherical symmetry and to measure the brightness temperature that could help determine if the source has a classical thermal wind. Unfortunately, since the source is not clearly resolved in any of the data sets and it is fairly weak, it was not possible to determine its dimensions directly from our 3.6-cm maps (see Fig. 1).

However, White & Becker (1982) have shown that it is possible to determine the size of a source directly from the u, v data, assuming a spherically symmetric source. Besides, Escalante et al. (1989) have shown that for a marginally resolved wind source the observed flux density depends linearly on the projected

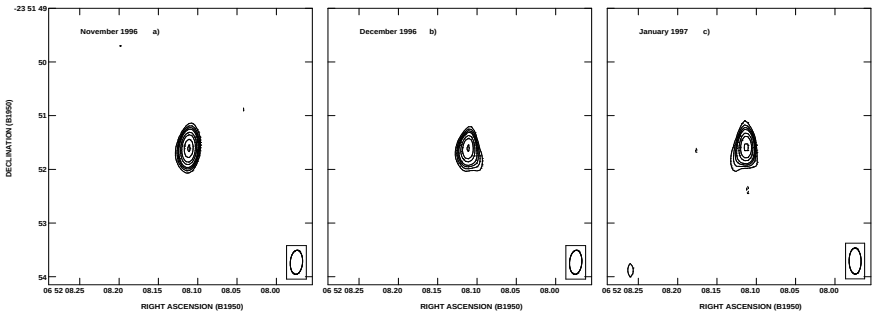

Figure 1: VLA CLEANed 3.6-cm maps for the three high resolution data sets. The maps were obtained with an intermediate *(u,v)* data weight (ROBUST=0). In all three maps the source appears practically unresolved (see beams at right bottom cormer).

baseline separation. Thus, it is possible to determine the source size by making a linear fit to the data in the u, v plane and furthermore to determine its brightness temperature from the same fit. A least squares fit was applied to the real part of all our high angular resolution data using the following equation:

$$V(b) = S_\nu \, (1 - A\, b) \tag{1}$$

where b is the projected baseline separation, given in wavelengths, S_ν is the total flux density, and A is the fitted slope. In our case we have obtained the following values for the slope and the total flux density: $A = 4.6 \pm \times 10^{-7}$ and $S_\nu = 1.52 \pm 0.03$ mJy. Thus, the angular diameter of the source within which half of the flux density is originated can be obtained from the equation:

$$\left[\frac{\theta}{''}\right] = 1.19 \times 10^5 \; A \tag{2}$$

while the brightness temperature is obtained from the relation:

$$\left[\frac{T_B}{10^4 \; K}\right] = \left[\frac{9.48 \times 10^{-15}}{A^2}\right] \; \left[\frac{S_\nu}{mJy}\right] \; \left[\frac{\lambda}{cm}\right]^2 \tag{3}$$

Both relations were derived by Escalante et al. (1989). Then using these expressions we obtained the angular size and the brightness temperature for

WR 6: $\theta = 0\farcs06 \pm 0\farcs01$ and $T_B = 9000 \pm 2500°K$. The angular size corresponds to a dimension of $\sim$ 100 AU at an assumed distance of 1.8 kpc. As we can see, the brightness temperature value is consistent with a classical thermal wind. Additional evidence comes from the spectral index $\alpha = 0.8 \pm 0.2$, obtained from the average of our observations and the 6-cm value of Hogg (1982). Finally, we have obtained the mass loss rate, $\dot{M} = 2.8 \pm 1.0 \times 10^{-5} M_\odot$ yr^{-1}, using the formulation of Panagia & Felli (1975) and a terminal wind velocity of 2700 km s^{-1}.

Then, regarding the main goal of our study, we have not found any firm evidence supporting the possibility of WR 6 having an anisotropic wind, at least one that is evident at scales of $0\farcs2$ or larger. Therefore we cannot provide evidence for a relation between an anisotropy in the stellar wind and the ovoidal shape of the HI cavity. Instead, our data appear consistent with an isotropic thermal wind. Besides, comparing the four flux densities that we have (Table 1), we found no clear evidence for large variability ($\leq$ 15%), in approximately 6 months.

Acknowledgements

We want to thank G. Koenigberger for valuable comments. MEC and LFR acknowledge the support from DGAPA-UNAM and CONACyT-México.

References

Arnal, E.M., Cappa, C.E., 1996, MNRAS 279, 788
Escalante, V., Rodríguez, L.F., Moran, J.M., Cantó, J., 1989, RevMexAA 17, 11
Hogg, D.E., 1982 in IAU Symp. 99, Wolf-Rayet Stars: Observations, Physics and Evolution, eds. C.W.H. de Loore & A.J. Willis, Dordrecht, Reidel, p.221
Panagia, N., Felli, M., 1975, A&A 39, 1
White, R.L., Becker, R.H., 1982, ApJ 262, 657

Multiwavelength Study of the Cas OB5 Supershell

A. Moór, Cs. Kiss

Konkoly Observatory of the Hungarian Academy of Sciences
H-1525 Budapest, P.O. Box 67 , Hungary
E-mail: moor@konkoly.hu

Abstract

We present the results of a multiwavelength study of a large, expanding shell around the Cas OB5 association. Based on the analysis of HI, CO and infrared data the main parameters of the shell were determined. We estimated the total mass in the shell to be $\approx 7.5 \times 10^5 M_\odot$.
Keywords: *ISM:bubbles-ISM:individual(Cas OB5)*

1. Introduction

It is well known that large shell-like structures are relatively common in the disk of spiral galaxies. While the formation of medium size bubbles can be explained by the influence of a single SN event or the stellar wind of massive stars, the size of the largest galactic structures are exceeded by a few orders of magnitude than that created by single event. It is established that these large shells are formed by the energy release of massive stars in OB associations, may be created by impacts of high velocity clouds or its energy input may connect with Gamma-Ray Burst events.

In the last decades several neutral hydrogen shells were investigated apparently related to galactic OB associations (e.g. Cep OB2 (Kun et al., 1987); Orion OB1 (Brown et al., 1995); Perseus OB1 (Cappa & Herbstmeier, 2000)). In our study we investigated the ISM in the vicinity Cas OB5. In this area a large elongated HI shell was found by Fich (1986) with a center position of $l = 117.5°, b = 1.5°$. It was suspected that some SN events occured in the pre-rarified medium of the HI shell and these supernovae actively engaged in enlarging the HI shell. Schwartz (1987) found a far infrared ring ($l = 118°, b = 2°$, diameter $= 5°$) close to the HI shell defined by Fich. Using the diffuse infrared emission originating from this region Kiss et al. (2003, in prep.) identified a far infrared loop GIRL 117+01 at a position similar to Schwartz's. We used HI, CO and infrared data to determine the important parameters of this shell.

2. HI data analysis

In order to study the distribution of HI gas in the environment of Cas OB5, we analyzed the HI emission in the region $108° \leq b \leq 127°$ and $-7° \leq b \leq 9°$ over the velocity interval from $-100\,\mathrm{kms}^{-1}$ to $+30\,\mathrm{kms}^{-1}$. The data were obtained from the Leiden–Dwingeloo HI survey (Hartmann et al., 1997).

Our investigation revealed a large HI shell in the velocity range $[-60\,\mathrm{kms}^{-1} \leq v \leq +3\,\mathrm{kms}^{-1}]$ surrounding the OB association. The projected image of the loop extends to $\sim 8.5°$ in both directions. In Fig. 1 we display the distribution of the neutral hydrogen emission integrated within the velocity range above.

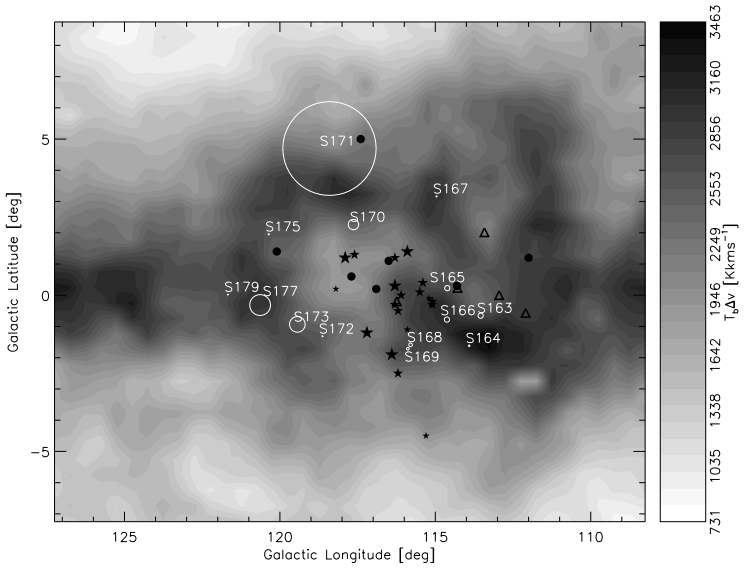

Figure 1: The integrated HI emission map through the velocity range $-60\,\mathrm{kms}^{-1}$ to $+3\,\mathrm{kms}^{-1}$. The displayed Sharpless HII regions are indicated by circles, whose diameter show the mean angular extent of the objects. The star symbols denote the members of the association while the filled circles and triangles mark the SNRs and pulsars respectively

On the basis of the distance to Cas OB5 and HII regions (Sharpless, 1959) encircling the structure we applied a distance of 2.5 kpc for the shell. We assumed that the HI emission is optically thin. After the removal of the background we determined the mass of the HI shell by summing up the column densities of the individual points associated with the shell. This yielded a mass of $M_{sh} \sim 6.3 \times 10^5 M_\odot$. The approaching side of the shell is twice as massive twice as the receding one. This feature sets the true systemic velocity of the center of the expansion to $v_{LSR} \approx -38 kms^{-1}$ and provides a momentum-weighted expansion velocity (Ábrahám et al., 2000) of $v_{eff} \approx 20 kms^{-1}$.

3. Molecular gas in the shell

Heyer et al. (1998) found several large voids of CO emission in the integrated intensity images produced by the FCRAO CO Survey of the Outer Galaxy and demonstrated that there is no extended emission within these voids at a level > 50 mK. One of the most prominent voids is centered at $l = 117.6°, b = 0.0°$ and coincides with the Cas OB5 shell.

In order to estimate the molecular gas mass in the shell we used the Outer Galaxy Survey Cloud Catalog compiled by Heyer et al. (2001). To find the clouds associated with the structure we cut the HI data cube for subsequent 5 kms^{-1} wide slices and searched for clouds in the given velocity range in the shell area. In the velocity interval $v \leq -20 kms^{-1}$ the CO emission originates from the Local Arm therefore we did not consider these clouds in the following.

Using the parameters of the associated clouds (Heyer et al., 2001) and based on the assumption that these clouds have the same distance as the shell we were able to derive the mass of the molecular shell. We estimate the total molecular gas mass to be $\sim 1.2 \times 10^5 M_\odot$. It should be noted that this method has significant uncertainties since the CO 1-0 line is usually optically thick in molecular clouds.

4. Infrared data

The Cas OB5 shell can be identified in the COBE/DIRBE maps of this region. In order to determine the dust mass in the shell we used the 100 and 240μm COBE/DIRBE data. Assuming ν^2 emissivity law we calculated the dust surface density following the method by Hildebrand (1983). The total cold dust mass of the structure was derived by summing up the surface density values of the appropriate COBE/DIRBE pixels. This resulted in $9.5 \times 10^3 M_\odot$.

5. Summary

We investigated the ISM in the vicinity of the Cas OB5 association based on HI, CO and infrared data, and we identified a large shell at each different wavelength. The whole structure is at a distance of 2.5 kpc and is about 190 pc in radius. The expansion velocity of the shell is $\sim 20\,\mathrm{kms}^{-1}$. The total swept up mass is $\sim 7.5 \times 10^5 \mathrm{M}_\odot$

Acknowledgements

This work has been partly supported by the Hungarian Research Fund (OTKA T-034998).

References

Ábrahám, P., Balázs, L.G., Kun, M., 2000, A&A 354, 645
Brown, A.G.A., Hartmann, D., Burton, W.B., 1995, A&A 300, 903
Cappa, C.E., Herbstmeier, U., 2000, AJ 120, 1963
Fich, M., 1986, ApJ 303, 465
Hartmann, D., Burton, W. B., 1997, Atlas of Galactic Neutral Hydrogen, Cambridge: Cambridge Univ. Press
Heyer, M.H., Brunt, C., Snell, R.L., et al., 1998, ApJS 115, 241
Heyer, M.H., Carpenter, J.M., Snell, R.L., 2001, ApJ 551, 852
Hildebrand, R.H., 1983, QJRAS 24, 267
Kun, M., Balázs, L.G., Tóth, I., 1987, Ap&SS 134, 211
Schwartz, P.R., 1987, ApJ 320, 258
Sharpless, S., 1959, ApJS 4, 257

Processes on Galactic Scales

Chemodynamical Modeling of Dwarf Galaxy Evolution

P. Berczik[1], G. Hensler[2], Ch. Theis[2], R. Spurzem[3]

[1]Main Astronomical Observatory, Ukrainian National Academy of Sciences
Zabolotnoho Str., 27, 03680, Kiev, Ukraine.
E-mail: berczik@mao.kiev.ua
[2]Institut für Theoretische Physik und Astrophysik, University of Kiel,
Olshausenstr. 40, 24098 Kiel, Germany.
[3]Astronomisches Rechen-Institut,
Mönchhofstraße 12-14, 69120 Heidelberg, Germany.

Abstract

We present our recently developed 3-dimensional chemodynamical code for galaxy evolution. It follows the evolution of all components of a galaxy such as dark matter, stars, molecular clouds and diffuse interstellar matter (ISM). Dark matter and stars are treated as collisionless N-body systems. The ISM is numerically described by a smoothed particle hydrodynamics (SPH) approach for the diffuse (hot) gas and a sticky particle scheme for the (cool) molecular clouds. Additionally, the galactic components are coupled by several phase transitions like star formation, stellar death or condensation and evaporation processes within the ISM. As an example here we present the dynamical, chemical and photometric evolution of a star forming dwarf galaxy with a total baryonic mass of $2 \times 10^9 M_\odot$.
Keywords: *computational methods: SPH, chemodynamics – evolution of galaxies: dwarf galaxy evolution*

1. Introduction

Since several years smoothed particle hydrodynamics (SPH, Monaghan, 1992) calculations have been applied successfully to study the formation and evolution of galaxies. Its Lagrangian nature as well as its easy implementation together with standard N-body codes allows for a simultaneous description of complex dark matter-gas-stellar systems (Navarro & White, 1993; Mihos & Hernquist, 1996). Nevertheless, until now the present codes lack processes that are based on the coexistence of different phases of the interstellar medium (ISM), mainly dissipative, dynamical and stellar feedback, element distributions, etc. We have therefore developed a 3d chemodynamical code which is based on our single phase galactic evolutionary program (Berczik, 1999, 2000).

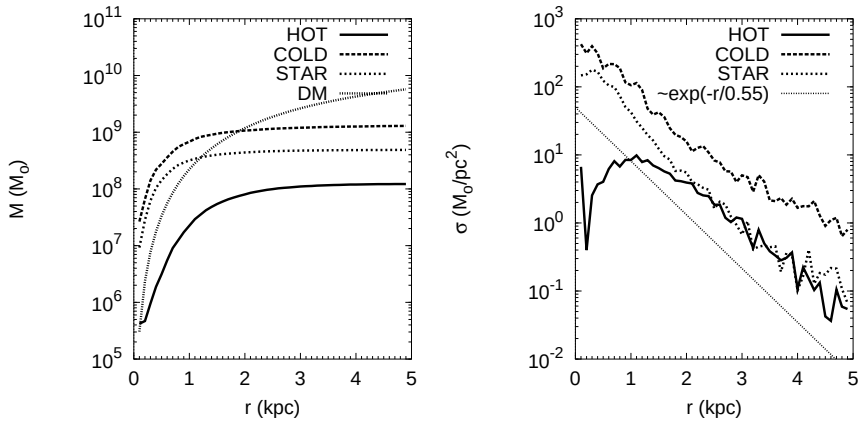

Figure 1: Radial distribution of the cumulative mass (left) and the surface density (right) for the different components in the central region of the model galaxy after 1 Gyr.

This code includes many complex effects such as a multi-phase ISM, cloud-cloud collisions, a drag force between different ISM components, condensation and evaporation of clouds (CE), star formation (SF) and a stellar feedback (FB). This code is a further development of our single phase galactic evolutionary program (Berczik, 1999, 2000) including now different gaseous phases. The more detailed description of the new code and the full list of the interaction processes between all gaseous and stellar phases will be presented in a more comprehensive paper by Berczik et al. (2002). Here we just briefly describe some basic features and effects.

In our new (multi-phase gas) code we use a two component gas description of the ISM (Theis et al., 1992; Samland et al., 1997). The basic idea is to add a cold (10^2 – 10^4 K) cloudy component to the smooth and hot gas (10^4 – 10^7 K) described by SPH. The cold clumps are modelled as N-body particles with some "viscosity" (Theis & Hensler, 1993) (cloud-cloud collisions and drag force between clouds and hot gas component). The cloudy component interacts with the surrounding hot gas also via condensation and evaporation processes (Cowie et al., 1981; Köppen et al., 1998). In the code we introduce also star formation. The "stellar" particles are treated as a dynamically separate (collisionless) N-body component. Only the cloud component forms the stars. During their evolution, these stars return chemically enriched gas material and energy to

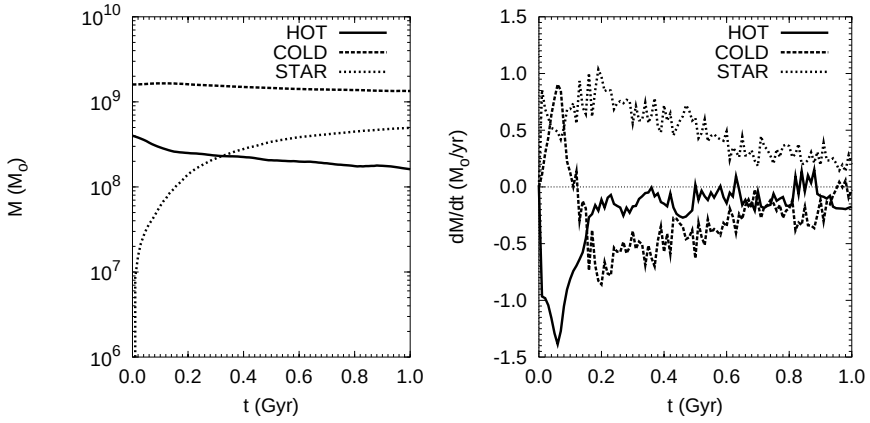

Figure 2: Temporal evolution of the mass (left) and mass exchange rate (right) for the different components of the model galaxy.

both gaseous phases.

2. Basic ingredients of the code

For the parametric description of the cold clumps in the code we use the mass *vs.* radius relation for clouds based mainly on observations and also some theoretical work in this direction (Larson, 1981; Solomon et al., 1987; Maloney, 1990):

$$h_{\rm cl} \simeq 50 \cdot \sqrt{\frac{m_{\rm cl}}{10^6\ {\rm M}_\odot}}\ \ {\rm pc}$$

This parametrization has already successfully been applied for the description of the cloudy medium of the ISM in Theis & Hensler (1993) and Samland et al. (1997).

The basic mechanism for the mass exchange between "cold" and "hot" gaseous phases is a condensation *vs.* evaporation (CE) of the cold cloud clumps. In our code we follow the prescription of these processes using the model proposed in Cowie et al. (1981) and Köppen et al. (1998). In this model the basic parameter controlling the process of CE is σ_0, which gives the ratio between a typical length scale of electron thermal conduction and the cloud size (compare also McKee & Begelman (1990); Begelman & McKee (1990)). If the cloud is small

or has a high temperature the conduction length may exceed the cloud size ($\sigma_0 > 1$) and conductive evaporation is limited by saturation. On the other hand, if the temperature of the cloud becomes very low or its size very large, the cooling length scale becomes shorter than the cloud size and condensation substitutes evaporation. For simplicity and as in Cowie et al. (1981) we just use here $\sigma_0 = 0.03$ as transition value from evaporation to cooling, although a more detailed physical description should invoke the cooling or field length (McKee & Begelman, 1990; Begelman & McKee, 1990). In total the rate at which "cold" clouds evaporate their own material to the surrounding "hot" gas or acquire mass by condensation from the surrounding gas is

$$\frac{dm_{\rm cl}}{dt} = \begin{cases} 0.825 \cdot {\rm T}^{5/2}\, h_{\rm cl}\, \sigma_0^{-1} & \sigma_0 < 0.03 \quad \textbf{Condensation} \\ -27.5 \cdot {\rm T}^{5/2}\, h_{\rm cl}\, \Phi & 0.03 \le \sigma_0 \le 1.0 \quad \textbf{Evaporation} \\ -27.5 \cdot {\rm T}^{5/2}\, h_{\rm cl}\, \Phi\, \sigma_0^{-5/8} & \sigma_0 > 1.0 \quad \textbf{Saturated Evap.} \end{cases}$$

where we have used $\Phi = 1$ (no inhibition of evaporation by magnetic fields) and

$$\sigma_0 = \left(\frac{{\rm T_{hot}(K)}}{1.54 \cdot 10^7} \right)^2 \frac{1}{\Phi\, n_{\rm hot}({\rm cm}^{-3})\, h_{\rm cl}({\rm pc})}$$

In our model the first important dynamical effect in the list of interactions between the two gaseous phases is cloud dragging (DRAG). For this reason we use the prescription proposed in the papers by Shu et al. (1972); Bisnovatyi-Kogan & Sunyaev (1972):

$$\frac{d\mathbf{p}_{\rm cl}}{dt} = C_{\rm DRAG} \cdot \pi h_{\rm cl}^2\, \rho_{\rm hot}\, |\, \mathbf{v}_{\rm cl} - \mathbf{v}_{\rm hot}\, |\, (\mathbf{v}_{\rm cl} - \mathbf{v}_{\rm hot})$$

The drag coefficient $C_{\rm DRAG}$ represents the ratio of the effective cross section of the cloud to its geometrical one $\pi h_{\rm cl}^2$ and is set to 0.5. A value of order unity for $C_{\rm DRAG}$ has the physically correct order of magnitude for the forces exerted by a pressure difference before and after a supersonic shock wave (Courant & Friedrichs, 1998).

The second important dynamical effect during the evolution of the cloudy medium is a cloud *vs.* cloud collisions (COLL). These processes can also significantly reduce the kinetic energy of the cloudy system. As a first approach for these processes we assume that in each collision the colliding clouds lose only 10 % of their kinetic energy.

Stars inject a lot of mass, momentum and energy (both mechanical and thermal) into the galactic system through supernova (SN) explosions, planetary

nebula (PN) events and stellar wind (SW). The gas dynamics then strongly depends on the star formation (SF) and feedback (FB) processes.

Stars are supposed to be formed from collapsing and fragmenting cold gaseous clouds. Some possible SF criteria in numerical simulation have been examined (Katz, 1992; Navarro & White, 1993; Friedli & Benz, 1995). In our code we use the "standard" Jeans instability criterion inside the cloud particle, with randomized efficiency for SF. As a first step we select the cloud particles with:

$$h_{\rm cl} \; > \; \lambda_{\rm J} \; \equiv \; c_{\rm cl} \sqrt{\frac{\pi}{G \; \rho_{\rm cl}}}$$

Next, we calculate the maximum SFR from the whole Jeans mass $M_{\rm J}$ converted from the cloud to star particle during the $\tau_{\rm cl}^{\rm ff}$ time inside the Jeans volume $V_{\rm J}$:

$$\frac{d\rho_*^{\rm max}}{dt} \; \equiv \; \frac{M_{\rm J}}{\tau_{\rm cl}^{\rm ff} \; V_{\rm J}} \; = \; \frac{4}{3} \sqrt{\frac{6 \; G}{\pi}} \; \cdot \; \rho_{cl}^{3/2}$$

where: $\tau_{\rm cl}^{\rm ff} \; \equiv \; \sqrt{\frac{3 \; \pi}{32 \; G \; \rho_{\rm cl}}}$. We set the actual SFR in each current act of SF by randomizing these maximum SFRs:

$$\frac{d\rho_*}{dt} \; = \; \mathbf{RAND} \; (0.1 \; \div \; 1.0) \; \cdot \; \frac{d\rho_*^{\rm max}}{dt}$$

Every new "star" particle in our SF scheme represents a separate, gravitationally bound star formation macro region i.e. Single Stellar Population (SSP). The "star" particle is characterized by its own time of birth $t_{\rm SF}$ which is set equal to the moment of particle formation. We assume that in the moment of creation the "star" particle, the individual stars inside our macro "star" particle are distributed according to the Initial Mass Function (IMF) by Kroupa et al. (1993).

During the evolution, these "star" particles return the chemically enriched gas to surrounding "gas" particles due to SNII, SNIa, PN events. As a first approach, we consider only the production of ^{16}O and ^{56}Fe. The "star" particles return to ISM also the energy due to the SW, SNII, SNIa, PN processes. The total energy released by "star" particles is calculated at each time step and distributed (in the form of thermal energy) between the neighbouring ($N_B = 50$) "gas" particles.

The code also includes the photometric evolution of each "star" particle, based on the idea of the SSP (Bressan et al., 1994; Tantalo et al., 1996). At each time step, absolute magnitudes: M_U, M_B, M_V, M_R, M_I, M_K, M_M and M_{BOL} are defined separately for each "star" particle. The spectro-photometric

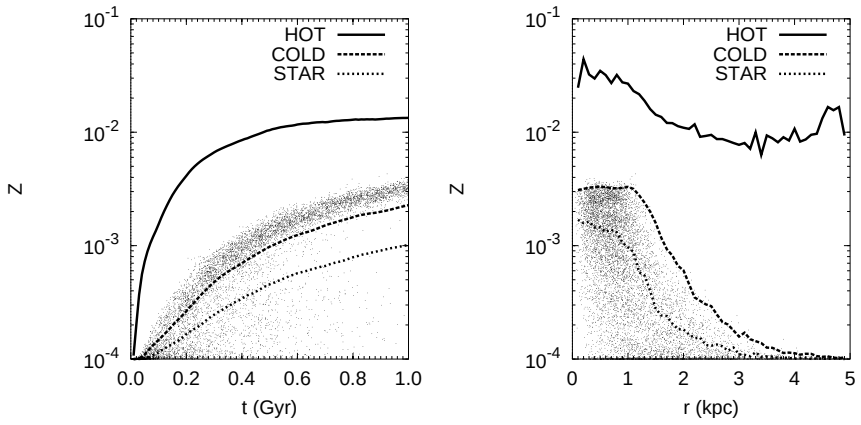

Figure 3: Temporal evolution of the metallicities (left) and their radial distribution after 1 Gyr (right). Individual metallicities of newly born stars are marked by dots.

evolution of the overall ensemble of "star" particles forms the Spectral Energy Distribution (SED) of the galaxy.

As a test of our new code, we calculate the evolution of an isolated star forming dwarf galaxy. The initial total gas content of our dwarf galaxy is 2×10^9 $M_\odot$ (80 % "COLD" + 20 % "HOT" which is placed inside a fixed dark matter halo with parameters $r_0 = 2$ kpc and $\rho_0 = 0.075$ $M_\odot/pc^3$ (Burkert, 1995). With these parameters the dark matter mass inside the initial distribution of gas (20 kpc) is $\simeq 2 \times 10^{10}$ $M_\odot$. We set the initial temperatures on 10^3 K for the cold gas and on 10^5 K for the hot gas. For the initial gas distribution we use a Plummer-Kuzmin disk with parameters a = 0.1 kpc and b = 2 kpc (Miyamoto & Nagai, 1975). The gas initially rotates in centrifugal equilibrium around the z-axis.

We choose the dwarf galaxy as an appropriate object for our code, because in this case even with a relatively "small" number of cold "clouds" ($\sim 10^4$) we achieve the required physical resolution for a realistic description of individual molecular clouds ($\sim 10^5$ $M_\odot$) as a separate "COLD" particle. In the simulation we use $N_{hot} = 10^4$ SPH and $N_{cold} = 10^4$ "COLD" particles. After 1 Gyr more than 10^4 additional stellar particles are created.

3. First results

After a moderate collapse phase the stars and the molecular clouds follow an exponential radial distribution, whereas the diffuse gas shows a central depression as a result of stellar feedback (Fig. 1). The metallicities of the galactic components behave quite differently with respect to their temporal evolution as well as their radial distribution (Fig. 3). Especially, the ISM is not well mixed at any stage.

In Fig. 1 we present the mass and surface density distribution of the different components in the central region of the model after 1 Gyr of evolution. In the region up to $\approx$ 2 kpc the baryonic matter dominates over the DM. The surface density of the stars can well be approximated by an exponential disk with a scale length of 0.55 kpc. In the distribution of hot gas we see a central "hole" ($\approx$ 1 kpc), as a result of gas blow-out from the center mainly due to SN explosions but not for the cold gas. This result disagrees with the model by Mori et al. (1999) where a density hole is caused by their single gas-phase treatment.

In Fig. 2 we present the evolution of the mass and the mass exchange rate of the different components. The SFR (i.e. dM_{STAR}/dt) peaks at a value of 1 $M_\odot yr^{-1}$ after 200 Myrs. Afterwards it drops to 0.2 $M_\odot yr^{-1}$ within several hundred Myrs. After 1 Gyr the stellar mass has already reached 5×10^8 $M_\odot$. Another interesting feature is the behaviour of the hot gas phase mass exchange. After the initial violent phase of condensation an equilibrium is established which gives a hot gas fraction of about 10% of the total gas mass.

The metal content of the diffuse gas and the clouds differ significantly over the whole integration time (Fig. 3). Due to SNII and SNIa events, the metallicity of the hot phase exceeds that of the clouds by almost one order of magnitude. The clouds mainly get their metals by condensation of the hot phase. The central metallicity plateau (up to 1 kpc) of the cold component is explained by the fact, that condensation of metal-enriched material does not work efficiently in that region. This signature agrees well with the observed abundance homogeneity in dIrrs over up to 1 kpc (e.g. in I Zw 18: Izotov, 1999). Moreover, the conditions in the centre lead mainly to evaporation of clouds which also prevents the mixing with the metal enriched hot gas.

Acknowledgements

The work was supported by the German Science Foundation (DFG) with the grants 436 UKR 18/2/99, 436 UKR 17/11/99 and the SFB439 (subproject B5) at the University of Heidelberg. P.B. is grateful for the hospitality of the Astronomisches Rechen-Institut

(Heidelberg) where the main part of this work has been done. The calculation has been computed with the GRAPE5 system at the Astronomical Data Analysis Center of the National Astronomical Observatory, Japan. R.Sp. acknowledges support by the German-Japanese cooperation grant 446 JAP 113/18/0-2.

References

Begelman, M.C., McKee, C.F., 1990, ApJ 358, 375
Berczik, P., 1999, A&A 348, 371
Berczik, P., 2000, Ap&SS 271, 103
Berczik, P., Hensler, G., Theis, Ch., Spurzem, R., 2002, A&A, in prep.
Bisnovatyi-Kogan, G.S.,Sunyaev, R.A., 1972, SvA 16, 201
Bressan, A., Chiosi, C., Fagotto, F., 1994, ApJ 94, 63
Burkert, A., 1995, ApJ 447, L25
Courant R. & Friedrichs K.O., 1998, in "Supersonic Flow and Shock Waves" (Appl. Math. Sciences Vol. 21), Springer-Verlag, Berlin, Heidelberg, p.325
Cowie, L.L., McKee, C.F., Ostriker, J.P., 1981, ApJ, 247, 908
Friedli, D., Benz, W., 1995, A&A 301, 649
Izotov, Y.I., 1999, Proc. XVIII. Rencontre de Moriond, Les Arc, *Dwarf Galaxies and Cosmology*, eds. T.X.Thuan et al., Edition Frontiere, Gif-sur-Yvette
Katz, N., 1992, ApJ 391, 502
Kroupa, P., Tout, C., Gilmore, G., 1993, MNRAS, 262, 545
Köppen, J., Theis, Ch., Hensler, G., 1998, A&A, 331, 524
Larson, R.B., 1981, MNRAS 194, 809
Maloney, P., 1990, ApJ 349, L9
McKee, C.F., Begelman, M.C., 1990, ApJ 358, 392
Mihos, J.C., Hernquist, L., 1996, ApJ 464, 641
Miyamoto, M., Nagai, R., 1975, PASJ 27, 533
Monaghan, J.J., 1992, ARA&A 30, 543
Mori, M., Yoshii, Y., Nomoto, K., 1999, ApJ 511, 585
Navarro, J.F., White, S.D.M., 1993, MNRAS 265, 271
Samland, M., Hensler, G., Theis, Ch., 1997, ApJ 476, 544
Shu, F.H., et al., 1972, ApJ 173, 557
Solomon, P.M., Rivolo, A.R., Barrett, J., Yahil, A., 1987, ApJ 319, 730
Tantalo, R., Chiosi, C., Bressan, A., Fagotto, F., 1996, A&A 311, 361
Theis, Ch., Burkert, A., Hensler, G., 1992, A&A 265, 465
Theis, Ch., Hensler, G., 1993, A&A 280, 85

Milky Way Parameters by the Results of N-body Simulation

A.V. Khoperskov, N.V. Turina
Sternberg Astronomical Institute
119992, Universitetskij pr., 13, Moscow, Russia
E-mail:[1]khopersk@sai.msu.ru,[2]tiurina@sai.msu.ru

Abstract

The results of N-body experiments modelling the disc of our Galaxy are presented. We used the suggestion, that the disc at all radii is on the threshold of gravitational stability. This suggestion sets some limits on dynamic and kinematic parameters of the main subsystems of the Galaxy (disc, bulge and halo). In the solar neighborhood the upper bound of surface density is calculated as $58\,M_\odot/\mathrm{pc}^2$. We came to the conclusion, that the local minimum of the rotation curve in the region $6\,\mathrm{kpc} < r < 10\,\mathrm{kpc}$ is not the result of mass distribution, but may arise from local dynamic processes or another factors, that can cause non-circular motion. Using the observed stellar velocity dispersion and suggesting that the bar in the Milky Way is long-living, we conclude that the central maximum on the rotation curve cannot be explained by the strongly concentrated core of the bulge. The best agreement between model parameters and observed data is reached for an exponential scale length of the disc of 3 kpc. The total disc mass does not exceed $M_d = 4.5 \cdot 10^{10}\,M_\odot$. The relative halo mass in the sphere $r < R_\odot = 8$ kpc should exceed 80 % of disc mass.
Keywords: *galaxies: Milky Way, N-body, bar, rotation curve*

1. Some problems of Milky Way

Rotation curve is one of the most important characteristics of any galaxy. Stars rotate more slowly than gas ($V_* < V_{gas}$, where $V_{gas}(r)$ is the rotation velocity of gas and young stars and $V_*(r)$ relates to the old stars' component). Circular rotation curve $V_c(r)$ is a parameter that enables us to obtain the distributions of gravitation potential and mass. There are many papers presenting rotation curves of stellar and gaseous components of the Milky Way, obtained from observations (Fig.1). Different rotation curves were obtained for various populations of the galactic disc: CO, HI regions, H_α-emission regions, classical cepheids, OB-associations, planetary nebulae and AGB-stars (different symbols and lines in the Fig. 1).

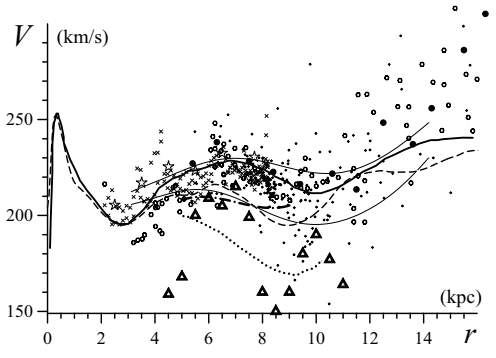

Figure 1: Rotation curves of the Milky Way, taken from different works (for details see Khoperskov & Tiurina, 2002).

Two major features are common for most of them: 1) local depression of the rotation velocity in the region $6\,\mathrm{kpc} < r < 10\,\mathrm{kpc}$ (local minimum of $V(r)$); 2) inner maximum of the rotation velocity near to the centre ($r \simeq 0.3$ kpc). These features may be caused either by mass distribution, or by some dynamic factors.

Spiral galaxies usually consists of two main components: a spherical subsystem (halo, bulge, core) and a disc subsystem (stellar and gaseous discs). Photometric data allow us to model each S-galaxy as disc+bulge system only, but the flatness of the rotation curve at far periphery enforce us to include a halo. If we use rotation curve only for modelling mass distribution of a galaxy, there will be a variety of models, because there is a well known ambiguity in interpretation: we can take low-mass disc and massive halo and bulge or low-mass spherical subsystem and massive disc, the observed rotation curve will be equally well explained in all these cases.

Photometric data give us radial and vertical scales for the distribution of brightness in disc and bulge, but there are some other parameters (like unknown M/L ratio), that give us a freedom for choosing the optimal model for mass distribution. The ambiguity disappears if we assume that the stellar disc of the galaxy is near the threshold of gravitational stability and has a minimum (for this stable state) stellar velocity dispersion c_r. So if we have constructed dynamic model, which would explain observed rotation curves of gas and stellar discs, dispersion of stellar velocities and other observed structural parameters (for example, height scale, scale length), it is possible to calculate the masses of disc and halo separately.

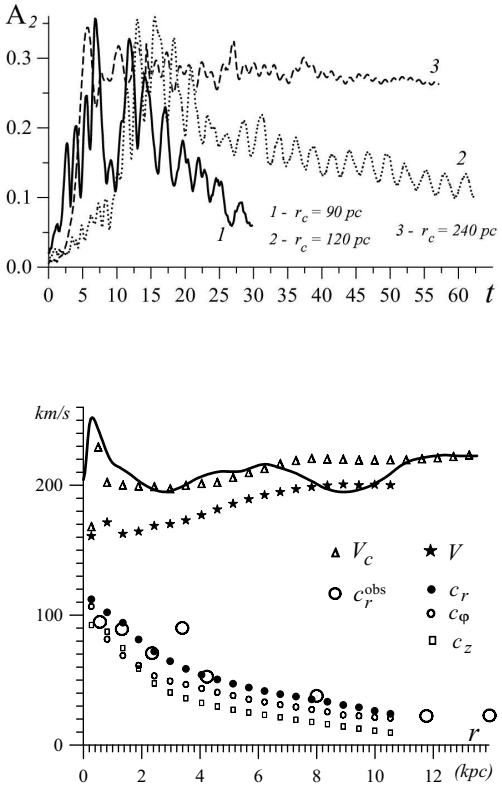

Figure 2: The results of dynamic simulation. (**a**) The evolution of Fourier-harmonics amplitude of the bar-mode in models with different core scales r_c. The decrease of amplitude at small r_c indicate the bar decay. (**b**) The radial distributions of velocity and velocity dispersion in the best model

2. Dynamic simulation of Milky Way

We used dynamic modelling of N-body, using Tree-code ($10^5 \div 5 \cdot 10^5$ particles) and Particle-Particle algorithms ($N = (1 \div 4) \cdot 10^4$). We studied the dynamic evolution of the self-gravitating 3D-disc, weakly unstable initially, which was embedded into the potential of the "rigid" spherical subsystem (halo, bulge, core). During the evolution there is a disc heating (increasing of the velocity dispersion) from the initial unstable state. The disc comes to the stationary state at the end of evolution. For this model disc, which possesses a minimum value of stellar velocity dispersion at a given radius, we compare all its parameters, like surface density, radial, vertical and azimuthal dispersions, disc scales of height and length with the observed ones. In particular, we came to the conclusion,

that if we try to explain the central maximum of Milky Way rotation curve (see Fig.1) by presence of the concentrated core, it would be impossible to create a long-lived bar (Fig.2a) in this dynamic model. The physical mechanism of bar destruction in the presence of a concentrated core is similar to activity of a central massive black hole (Hasan & Norman, 1990).

The presence the of local dip in circular rotation velocity V_c in the region $r \simeq 6 \div 10$ kpc contradicts observed kinematic data of the ratio of velocity dispersions $c_r/c_\varphi = 1.58$ (Dehnen & Binney, 1998) and the results of our dynamic simulation.

The dynamic model that best satisfies the data sets of observations, gives the following parameters of the main components: **bulge** with mass $M_b \leq 1.2{\cdot}10^{10} M_\odot$ and scale of core $r_c \geq 200$ pc; **disc** with full mass $M_d = 4.4{\cdot}10^{10} M_\odot$ and surface density in Solar neighborhood $\sigma_\odot \leq 58 M_\odot/\mathrm{pc}^2$, radial scale 3 kpc and scale height $z_0 = 0.5$ kpc; **halo** with the relative mass $\mu = M_h/M_d \geq 0.87$ at $r < R_\odot$ and $\mu \geq 1.6$ at 4 radial scales ($\sim$ 12 kpc). The ratio between the circular velocity of the disc component V_c^{disc} and the complete circular velocity V_c at the radius $r = 2.2L = 6.6$ kpc is equal to $V_c^{disc}/V_c = 0.73$.

Acknowledgements

This work has been partly supported by the grant 01-02-17597 (RFFI) and Federal programme (40.022.1.1.1101, 01.02.02).

References

Dehnen, W., Binney, J.J., 1998, MN, 298, 387
Hasan, H., Norman, C., 1990, ApJ, 361, 69
Khoperskov, A.V., Tiurina, N.V., 2002, Astr. Rep.

Kinematic Properties of Young Subsystems and the Rotation Curve of Our Galaxy

M.V. Zabolotskikh, A.S. Rastorguev, A.K. Dambis

Sternberg Astronomical Institute
119992, Universitetskij pr., 13, Moscow, Russia
E-mail: zabolot@sai.msu.ru

Abstract

The maximum-likelihood analysis is applied to space velocities of 113 classical Cepheids with periods longer than 9 days, 89 young open clusters with ages less than 40 Myr, 102 blue supergiants, 200 HII-regions and 150 HI radial velocities. We used the distance scales of objects balanced by the statistical-parallax technique. The kinematic properties of young subsystems have been derived (solar motion components, velocity-ellipsoid axes). The rotation curve is constructed from radial velocities of all objects on the galactocentric distances 2-14 kpc for short ($R_0 = 7.5$ kpc) and long ($R_0 = 8.5$ kpc) distance scale.
Keywords: *Galaxy: kinematics, rotation curve, open clusters, Cepheids, blue supergiants, HI, HII*

1. Introduction

The parameters of the Galactic rotation curve were determined by many authors, but it should be pointed out that these parameters depend first on the correctness of the adopted distance scale of objects under study. Objects with known distances – classical Cepheids, open star clusters (OSC), and OB-associations – allow the rotation curve to be determined only out to heliocentric distances of 4-5 kpc, whereas HI and HII kinematic data allow constructing the rotation curve over a wider interval of galactocentric distances. The main problem of using the hydrogen data is that the distances of giant molecular clouds (GMC) and, consequently, those of HII-regions, are determined from their single hot exciting stars whose distance scale is prone to random and systematic errors. Therefore, our goal is to refine the distance scales of young subsystems and to construct the rotational curve of our Galaxy.

2. Observational Data

Our sample included 89 young OSC with $\log T < 7.6$ and heliocentric distances determined by Dambis (1999) by fitting Kholopov's (1980) ZAMS with allowance for evolutionary deviations based on Geneva-group isochrones (Maeder and Meynet 1991). The radial velocities of cluster members were determined by Glushkova based on published data and can be found in the paper by Rastorguev et al. (1999). The proper motions of clusters were computed from those of their member stars found in the HIPPARCOS catalog (Baumgardt et al. 2000).

We also used 113 classical Cepheids with periods $P > 9^d$ and heliocentric distances computed using the fundamental-mode period-luminosity relation of Berdnikov et al. (1996): $\langle M_K \rangle_I = -5.46^m - 3.52^m \log P$ in accordance with the procedure described therein. An earlier statistical-parallax analysis (Rastorguev et al. 1999) showed that the sample of Cepheids with shorter periods is not homogeneous in terms of pulsation mode and may be contaminated by first-overtone pulsators. We used published Cepheid radial velocities and HIPPARCOS proper motions. Young OSC and long-period Cepheids make up a kinematically homogeneous reference sample consisting of 176 and 142 objects with radial velocities and proper motions, respectively, including 124 objects with space velocities.

We performed a separate analysis of a blue supergiant sample consisting of 102 stars with heliocentric distances tied to the OSC distance scale (Dambis 1990). The proper motions of supergiants adopted from the HIPPARCOS catalog, and radial velocities from the catalogs of Barbier-Brossat and Figon (2000) and WEB (Duflot et al. 1995).

Brand and Blitz (1993) published the distances and radial velocities for a total of 206 HII-regions. We selected 203 of these objects with spectroscopic or photometric distances inferred from their exciting stars. The radial velocities of HII-regions were determined from the CO (2.6-mm) radio lines of their associated molecular clouds. We did not include three HII-regions in the final list because of their large residual velocities relative to the provisional rotation-curve solution. The catalog mentioned above also gives standard errors of individual distances and line-of-sight velocities.

We adopted 150 tangent-point radial velocities of HI clouds from Fich et al. (1989). Note that published HI and HII radial velocities are traditionally corrected for the solar motion relative to the standard apex assumed to coincide with the local standard of rest (LSR), and therefore we first converted them into heliocentric radial velocities.

3. Method of Analysis

We used the techniques of maximum-likelihood and statistical parallax (including its simplified version) to compute the kinematic parameters and refine the distance scales involved. See Murray (1983) for a description of the principal ideas of the statistical-parallax method used in this paper. The tangential velocity of a star is computed from its proper motion and distance and therefore depends on the adopted distance scale, whereas radial velocities are distance independent. The distance scale factor is defined as $p = r_o/r_t$, where r_o is the adopted distance and r_t is the true distance. The gist of the method consists of reconciling the fields of radial and tangential velocities in terms of some model of the field of systematic motions and ellipsoidal distribution of residual velocities.

The residual velocity of a star can be written in the following form: $\Delta\mathbf{V} = \mathbf{V}_{obs} - \mathbf{V}_{sun} - \mathbf{V}_{rot}$, where $\mathbf{V}_{obs}$ is the observed space velocity; $\mathbf{V}_{sun}$ is the mean heliocentric velocity of the sample studied; $\mathbf{V}_{rot}$ is the contribution of Galactic differential rotation. Residual space velocities are usually assumed to have a three-dimensional normal distribution: $f(\Delta\mathbf{V}) = (2\pi)^{-3/2} |L_{obs}|^{-1/2} \{-0.5\Delta\mathbf{V}^T \times L_{obs}^{-1} \times \Delta\mathbf{V}\}$, where the matrix of covariance L_{obs} contains the ellipsoidal velocity distribution, errors of distances, radial velocities and proper motion and influence of errors of distances on the systematic velocities. We inferred the unknown parameters by using the maximum-likelihood method or in other words by minimizing the function $\mathrm{LF} = -\sum_{i=1}^{N} \ln f(\Delta\mathbf{V})$. To compute the parameter errors we used the method proposed by Hawley et al. (1986).

The simplified version of the statistical-parallax technique (as used, e.g., by Feast et al. 1998) based on reconciling the kinematic parameters inferred separately from radial velocities and proper motions. Thus it is well known that Oort's constant A inferred from proper motions is much less sensitive to the adopted distance scale than is the value of the same constant inferred from radial velocities. This allows not only the kinematic parameters to be determined but also the distance scale of objects under study to be refined. When refining the distance scale by reconciling the values of Oort's constant A we set $p = 1$.

4. Results and Discussion

First, we applied the maximum-likelihood method to our sample of Cepheids and OSC. Because the galactocentric distance of Sun R_0 and the distance scale

are correlated with each other, we performed our computations with two most commonly adopted values – $R_0 = 7.5$ and 8.5 kpc. We determined the angular velocity of galactic rotation from space velocities of Cepheids and OSC and then used it to construct the Galactic rotation curve based on the radial velocities of all objects considered. The dispersion of the inferred absolute magnitude is equal to $\sigma_M = 0.15^m$ for sample of Cepheids and OSC and $\sigma_M = 0.38^m$ for sample of blue supergiants. It should be noted that the study of the kinematics and space distribution in the disk of other galaxies showed the exponential decrease of surface brightness and velocity dispersion with galactocentric distance (Bottema 1993). But the real accuracy of the computed rotational curve allows us to get rid of this effect.

Table 1 lists the distance scale factors for our samples estimated by the statistical-parallax technique and its simplified version. We analyzed the problem of systematic differences between the distance scale factors given by this two methods. One hundred numerical simulations have shown that the distance scale factor is on the average equal to 1 from both methods and p_1 and p_2 are correlated with each other. We cannot unambiguously choose between the two approaches to the distance scale refinement. It is logical to associate the short and long distance scales with $R_0 = 7.5$ and $R_0 = 8.5$ kpc. In other words $p = 0.96 \rightarrow R_0 = 7.5$ kpc and $p = 0.84 \rightarrow R_0 = 8.5$ kpc for Cepheids+OSC sample and $p = 1.09 \rightarrow R_0 = 7.5$ kpc and $p = 0.97 \rightarrow R_0 = 8.5$ kpc for the blue supergiants sample.

Table 1. Distance scale factors estimated by the statistical-parallax technique (p_1) and by simplified version (p_2).

R_0, kpc	p_1, Cepheids+OSC	p_2, Cepheids+OSC	p_1, Supergiants	p_2, Supergiants
7.5	0.86	0.96	1.09	0.97
8.5	0.84	0.97	1.09	0.97
errors	±0.05	±0.09	±0.08	±0.16

The only way to match the distance scales of HII and stars is to compare the first derivatives of angular velocities inferred from radial and space velocities for gas and stars, respectively. In the result $p = 0.95$ for $R_0 = 7.5$ kpc and $p = 0.90$ for $R_0 = 8.5$ kpc. The good agreement between mean heliocentric velocity components of different young-object samples allows us to construct the rotation curve over a sufficiently wide interval of galactocentric distances, 2 – 14 kpc, using radial velocities of both stars and gas (see Fig. 1, 2). The resulting local centroid velocity and Oort's constant A

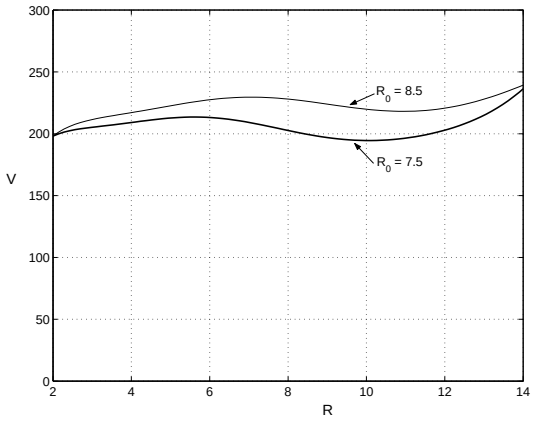

Figure 1: Galactic rotation curve $V(R)$ for the short (R_0 = 7.5 kpc) and long (R_0 = 8.5 kpc) distance scales

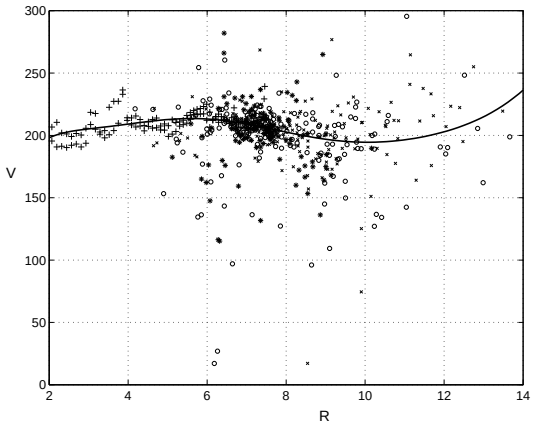

Figure 2: Galactic rotation curve $V(R)$ for the short distance scale (R_0 = 7.5 kpc) with young-object data points ("+" - HI, "×" - HII, "o" - Cepheids+OC, "*" - blue supergiants)

are equal to $V(R_0) = (206 \pm 10)$ kms^{-1}, $A = (17.1 \pm 0.5)$ kms^{-1}kpc^{-1} and $V(R_0) = (226 \pm 12)$ kms^{-1}, $A = (15.4 \pm 0.6)$ kms^{-1}kpc^{-1} for the short and long distance scale, respectively. We computed the velocity ellipsoid axes separately for Cepheids and OSC, supergiants and gas (see Table 2). We see that the axial ratio of the Cepheids and OSC velocity ellipsoid obeys closely to the Lindblad formula, whereas for the gas $\sigma_u \approx \sigma_v$.

Table 2. Heliocentric velocity components and velocity ellipsoid axes for the young object sample (* - fixing parameters).

	σ_u, kms^{-1}	σ_v, kms^{-1}	σ_w*, kms^{-1}	u_0, kms^{-1}	v_0, kms^{-1}	w_0*, kms^{-1}
Cepheids+OSC	13.30	7.59	7.55			
errors	±1.79	±0.41	–			
Supergiants	14.17	10.00	5.13			
errors	±0.51	±2.12	–	−9.17	−12.98	−7.25
HII	6.71	7.19	5.0			
errors	±0.60	0.93	–			
HI	6.60	6.05	5.0			
errors	–	±0.34	–	±0.48	±0.78	–

Acknowledgements

The work was supported by the Russian Foundation for Basic Research (grants nos. 01-02-06012, 00-02-17804, 99-02-17842, 01-02-16086, 02-02-16677, and 02-02-06593) and the Council for the Support of Leading Scientific Schools (grant no. 00-15-96627).

References

Barbier-Brossat, M., Figon, P., 2000, A&AS 142, 217

Baumgardt, H., Dettbarn, C., Wielen, R., 2000, A&AS 146, 251

Berdnikov, L.N., Vozyakova, O.V., Dambis, A.K., 1996, Astron. Lett. 22, 838

Bottema, R., 1993, A&A 275, 16

Brand J., Blitz, L., 1993, A&A 275, 67

Dambis, A.K., 1990, Sov. Astron. Lett. 16, 224

Dambis, A.K., 1999, Astron. Lett. 25, 7

Duflot, M., Figon, P., Meyssonnier, N., 1995, A&AS 114, 269

Feast, M., Pont, F., Whitelock, P., 1998, MNRAS 298, L43

Fich, M., Blitz, L., Stark, A.A., 1989, ApJ 342, 272

Hawley, S.L., Jeffreys, W.H., Barnes, III, T.J., L. Wan, 1986, ApJ 302, 626

Kholopov, P.N., 1980, Sov. Astron. 24, 7

Maeder F., Meynet, G., 1991, A&AS 89, 451

Murray, C.A., 1983, Vectorial Astrometry (A. Hilger, Bristol)

Rastorguev, A.S., Glushkova, E.V., Dambis, A.K., Zabolotskikh, M.V., 1999, Astron. Lett. 25, 595

The HIPPARCOS and TYCHO Catalogues, European Space Agency, 1997, ESA SP-1200

Published by the Konkoly Observatory of the Hungarian Academy of Sciences
Budapest, 2003